Università degli Studi di Napoli Federico II

DOTTORATO DI RICERCA IN FISICA FONDAMENTALE ED APPLICATA

Ciclo XXVI

Coordinatore: Prof. Raffaele Velotta

COHERENCE EFFECTS IN SUPERCONDUCTING HYBRID DEVICES

Settore Scientifico Disciplinare: FIS03

Dottorando:
Luca Galletti

Tutore:
Prof. Francesco Tafuri
Prof. Floriana Lombardi

Anni 2011/2014

factus de materia, cinis elementi
similis sum folio, de quo ludunt venti

CONTENTS

INTRODUCTION AND MOTIVATION

The combination different functionalities in a single device can be achieved in a hybrid, as for instance a device made of a semiconducting barrier connecting two superconducting electrodes. The scope of superconducting hybrid devices is to take advantage of the functionality of the different barriers. The proximity effect, induced by the superconducting electrodes, in addition, gives the unique capability to carry macroscopic coherence.

The new capabilities of assembling coplanar hybrid devices with unconventional barriers is becoming the new frontier both for the understanding of how superconductivity propagates in exotic conditions and for new possible perspectives of smart functionalities for innovative applications. Here, well established and universally accepted concepts need to be revised.

The diffusion of devices with nano/hybrid barriers has favored the use of junctions with lower critical current and capacitance, thus falling a regime of moderate damping, where the dissipation plays a significant role. The study of the dynamics of the escape from the metastable zero voltage state of the junction, is a standard tool to investigate the phase dynamics of the system, including its quantum codes. Here devices with higher dissipation are characterized by the onset of multiple re-trapping processes, described in this work.

The introduction of topological insulators, recently discovered in systems with strong spin-orbit, represents one of the milestones towards this re-definition of fundamental concepts, which passes through the study of the superconductivity in un-trivial topologies. These are the favorable conditions for the study of new phenomena, as for instance the presence of Majorana fermions at the edge states of a 1D topological superconductor, or embedded in two-dimensional vortex states.

This work is motivated by the study of the Josephson effect in unconventional conditions. A special attention is devoted to the study of

A. the moderate damping regime, characteristic of most hybrid devices, and

B. of topological insulator barrier. The aim is to identify those effect which are unconventional, in the sense of imprinting of topologically non trivial states.

Evidence of a ballistic coherent transport have been observed in a superconductor-topological insulator-superconductor junction, and it

has been attributed to the dominant role of the topological edge state to carry super-current. This work included a systematic and complete set of transport measurements of $Al/Bi_2Se_3/Al$ junctions in an external magnetic field, and in a microwave field. The most revealing measurement was the critical current as a function of the temperature, which gave the notion of the coherent ballistic transport. A comparative study of Shubnikov - de Haas oscillations and scanning tunneling spectroscopy gave an experimental signature compatible with a two dimensional electron transport channel with a Dirac dispersion relation.

The same ballistic transport regime was also confirmed on $Al/Bi_2Te_3/Al$ junctions, where, in addition, special attention was devoted to the escape dynamics. The merit of these measurements is to be the very first ones on junctions with topological barriers, further supported by a comparison with numerical codes based on Monte Carlo simulations. Our data gave evidence of moderate damping, through a comparative analysis performed also on other junctions, such as bi-epitaxial YBCO junctions. The possibility to reproducibly achieve low critical currents in sub-micron junctions can be controllably induced in larger junctions in case of low critical current densities, or in junctions with larger intrinsic dissipation levels, as occurring in high temperature supeconductors, thanks to their design scalability, and flexibility in controlling the level of damping.

These studies are based on a long-standing experience earned on a variety of devices, including NbN junctions with various barriers. It includes advanced knowledge on low noise measurements, performed at cryogenic temperatures, which I assimilated during my PhD project, in the laboratory of prof. Francesco Tafuri. I also had the opportunity of spending one year at the Chalmers University of Technology, in the laboratory of prof. Floriana Lombardi, where I completed my formation with competences in nano-fabrication techniques and in high magnetic field measurement systems.

Herewith follows a short description of the main content of this PhD thesis.

The first chapter is dedicated to a review of the main concepts of Josephson effect, including a study of the electrodynamics of the system. The study of the various regime of the superconducting transport are also discussed, as well as the dynamics of the escapes.

The second chapter is a quick review of the main concepts of the quantum Hall effect, in view a topological approach to the problem. The chapter also includes a short introduction of topological insulators and Majorana fermions.

In the third chapter I describe the experimental setup used for the low noise transport measurements and for measurements in high magnetic field. I also review the main fabrication techniques used in this work, and the main features of the coplanar hybrid devices fabricated.

In the fourth chapter I present the high magnetic field characterization of the Bi_2Se_3 barriers, including the transport measurements performed on the Hall bars and the STM analysis performed on the cleaved surface of the crystal.

In the fifth chapter the transport measurements of $Al/Bi_2Se_3/Al$ Josephson junctions is discussed in detail, including the measurement of the $I_C(T)$ curve, which gave the notion of ballistic coherent transport.

The sixth chapter is devoted to a comparative analysis of escape dynamics, performed on various devices. Here the measurements performed on $Al/Bi_2Te_3/Al$ junctions are compared with those performed on other junctions, as NbN junctions, bi-epitaxial YBCO junctions and with numerical codes based on Monte Carlo simulations

1 REMARKS ON PROXIMITY EFFECT

The Josephson effect is one of the most fascinating topics of the modern physics. This effect gives a direct experimental access to the quantum nature of a macroscopic system, paving the way to the notion of "quantum device".

Historically tunnel Josephson junctions have been the first play ground to characterize macroscopic quantum phenomena [54, 123, 43], physically related to the quantum behavior of the Josephson phase difference between the two electrodes. This is a macroscopic degree of freedom (i.e. the Gauge invariant phase difference between the BCS states of two condensates) manifesting a collective quantum behavior.

A Josephson junction (JJ) is a device formed by two superconducting electrodes see Fig. 1a, separated by a thin barrier [91]. When the gap between the electrode is small enough to create a coupling ("weak link") between the two condensates "the vacuum space becomes superconducting" (cit. A. Barone). In other words a dissipation-less current flows across the device up to a certain threshold value, referred as "critical current" (I_C).

A Josephson junction can be considered as a non-linear resonator [55], characterized by a quality factor (Q), which describes its dynamics. This is not surprising if we consider the junction as a capacitor to which the superconductivity of the electrodes has basically added an effective (i.e. "kinetic") inductance, thus creating a resonant LC circuit. The study of the dissipation mechanism is therefore one of the main issues for any quantum superconducting device. The typical resonant frequency (the plasma frequency ω_p) of Josephson junctions falls in the 100 GHz - 1 THz regime, making a Josephson junction an interesting element for a wide range of devices and applications (THz detectors [72, 154] and

emitters [181, 182, 15], SQUIDs magnetometers [42, 133], micro-coolers [112], molecular detectors [170], hot electrons bolometers [138] etc).

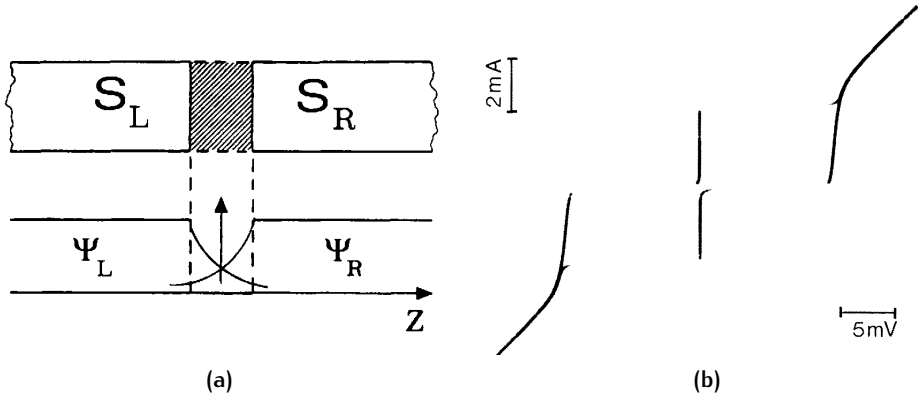

Figure 1: (a) Sketch of a Josephson junction. The magnitude of the wave-function of the condensates $\Psi_{L,R}$ is vanishing in the barrier, with a finite overlap. (b) Typical current-voltage characteristic of a device (adapted from Ref. [14]).

The nonlinear resonant nature of Josephson junctions, combined with their macroscopic quantum nature, makes them ideal candidates for the creation of "artificial atoms" in quantum bits (QuBIT)
[187, 189, 39, 40, 148]. Superconducting QuBITs have been a strong motivation for the study of macroscopic quantum phenomena [29], also in unconventional hybrid systems, which could benefit of the functionalities of complementary quantum components [135].

The propagation of superconductivity across the barrier is becoming more dense of a variety of physical flavors thanks to the recent introduction of capabilities
[64, 90, 139, 185, 191, 146, 158, 153, 53, 49, 41, 62]:

- of assembling nanowires and bi-dimensional flakes (of topological insulators and graphene for instance) with superconducting electrodes
- of building advanced coplanar structures
- of solving a broad range of problems of material science, which leads to a large variety of interfaces

Here, well established and universally accepted concepts need to be revised. The aim of this paragraph is to review the fundamental notions of the Josephson effect, which are functional for the understanding of the results presented in this work, and to give a tentative description of some unconventional features that will be discussed in the presentation of the experimental results.

1.1 JOSEPHSON EFFECT AND THE WEAK SUPERCONDUCTIVITY

The Josephson effect can be observed when the wave-functions of the coherent condensates of the two superconducting electrodes create an overlap, thus supporting the coherent flow of Cooper pairs.

The dynamics of the system is described by the well-known Josephson equations [14, 113].

$$I = I_C \sin\varphi \tag{1}$$

$$\frac{d\varphi}{dt} = \frac{2e}{\hbar}V \tag{2}$$

The first equation describes a relation between the dissipation-less current flowing through the junction and the Josephson phase. This relation is also referred as current-phase relation (CPR). As we will discuss in the next paragraphs, unconventional devices are characterized by modifications of the CPR [73]. For instance normal metal barriers includes a second harmonic [188, 22, 23], this feature was also observed in HTS superconductors [89]. Different barriers, like nanowires [141] or graphene 2D barriers [45] may lead to a more complex CPRs. Topologically non trivial barrier are expected to modify the periodicity of the CPR to a 4π periodic function [65, 149, 161]. More detail on the phenomenology in this type of devices is given in Sec. 2.4.

As a current bias is ramped up to the device, the Josephson phase is is adjusted to match the two members of Eq. 1. When the bias current exceeds the critical current I_C (see Fig. 1b), the current voltage (IV) curve of the device switches to a linear branch with a slope R_N. This is called the "normal resistance" of the junction. As discussed in the next paragraphs (Sec. 1.5), the transition to the resistive state can be either determined by a sudden switch or by a progressive crossover, corresponding to a rounded non-linear behavior of the IV curve. However, the appearance of a difference of potential V across the device corresponds to a time variation of the Josephson phase, following (Eq. 2).

Normally the measurement of current-voltage curves (IV) cannot measure the CPR, and only the value of I_C is measurable. Nevertheless the CPR strongly affects the behavior of the device under the effect of an external magnetic field, or a microwave field [14].

1.2 JUNCTIONS ELECTRODYNAMICS

In this paragraph the typical features of the Josephson junctions under the effect of an external magnetic field and of a microwave field are described.

1.2.1 Effects of Magnetic Field

The effect of a magnetic field is to create a spatial modulation of the phase φ along the barrier

$$\frac{\partial \varphi}{\partial x} = \frac{2e}{\hbar c} B_y d_{eff} \tag{3}$$

where B_y is the component of the magnetic field perpendicular to the junction plane, d is the separation between electrodes, and $d_{eff} = (2\lambda + d)$ is the effective width of the barrier (see Fig. 2a), including the London penetration depth λ of the electrodes [155].

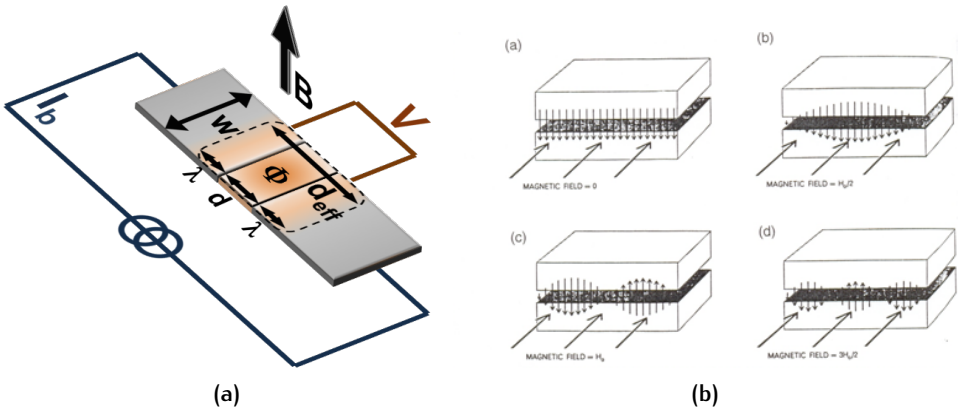

Figure 2: (a) Sketch of a Josephson junction, the shaded area corresponds to the effective area of the junction. (b) Sketch of the spatial modulations of the critical current density along the junction (see Eq. 4).

The modulation of the phase induces a spatial modulation of the critical current density (see Fig. 2b).

$$J = J_C \sin\left(\varphi + \frac{\Phi}{\Phi_0}\right) \tag{4}$$

In the simple case of a rectangular cross section with a homogeneous J_C, the simple Fraunhofer pattern can be found [14, 113].

$$I_C(B) = I_{C0} \left| \frac{\sin\left((\mathbf{B}\cdot\mathbf{S})/\phi_0\right)}{(\mathbf{B}\cdot\mathbf{S})/\phi_0} \right| \tag{5}$$

Here w is the width of the junction $\mathbf{S} = w d_{eff}$ is the surface, as shown in Fig. 2a, and $\phi_0 = \hbar/2e$ is the elementary flux quantum. The Eq. 5, shown in Fig. 3, comes from a spatial integration of Eq. 4 on the rectangular cross section barrier [14]. Deviations are expected for a different geometry of the barrier [130], for a not-uniform distribution of the critical current density across the cross section of the junction [197, 198, 57], or in a thin-film approximation [155]. Thus, the measurements of the Fraunhofer pattern is the standard test to verify the homogeneity of the critical current (and of the barrier) in a Josephson junction.

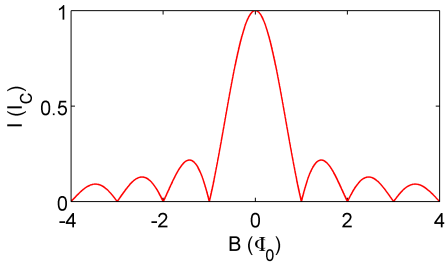

Figure 3: Modulation of the critical current as a function of the magnetic flux enclosed in the effective area of the junction. The modulation follows a Fraunhofer pattern (see Eq. 5) in a rectangular geometry.

There is a characteristic length-scale for the determination of the dynamics of the junction, called "Josephson penetration depth" [14, 113]

$$\lambda_J = \frac{\phi_0}{2\pi\mu_0 d_{eff} J_C} \tag{6}$$

If the physical dimensions of the junction exceed λ_J, the screening effects become significant [196, 147] and the magnetic field response of the junction can be more complex than the model presented above, including for instance the appearance of screening current on the edge of the junction. The junction in this case is said "magnetically long" [14].

A remarkable effect can be detected when the critical current density is completely concentrated on the edges. This is what conceptually is realized in a d.c. SQUID, with the only practical difference that the area in a SQUID can be macroscopically different.

1.2.2 Magnetic Field in Annular Geometries: d.c. SQUIDs

A d.c. SQUID is a devices made of two Josephson junctions in parallel [14, 176], enclosing a superconducting loop. When a magnetic field is treaded in the loop, the fluxoid

$$\int\int_S \mathbf{B}\cdot\mathbf{d\sigma} + \frac{m}{2\rho e^2}\oint_\Gamma \mathbf{J_s}\cdot\mathbf{dl} = n\Phi_0 \tag{7}$$

is quantized to an integer value of the elementary flux Φ_0.

The total current flowing through the circuit is given by

$$I = I_a \sin \varphi_a^* + I_b \sin \varphi_b^* \tag{8}$$

The dependence of $I_C(H)$ is characteristic of the nature and performance of the SQUIDs.

If the SQUID is made of two identical junctions, this modulation of I_C is [14]

$$I_C(B) = 2I_{C0} \left| \frac{\sin \pi\Phi_j/\Phi_0}{\pi\Phi_j/\Phi_0} \right| |\cos \pi\Phi_{ext}/\Phi_0| \tag{9}$$

At low field the modulation is a co-sinusoidal curve.

SQUIDs are ideal systems to study the unconventional features related to un-trivial current phase relations [183, 141]. The recent introduction of barrier of topological insulator reinforced the interest in this kind of measurements, as the presence of a topological barrier is expected to modify the periodicity of the CPR [183, 184] (Eq. 1).

1.2.3 Effects of Microwaves and the Shapiro Steps

This paragraph is dedicated to a description of how a microwave field modifies the IV curve of a junction. These measurements are also of fundamental interest, since they give an experimental access to the periodicity of the CPR of the device. Combining together Eq. 1, and 2 it is possible to obtain the equation

$$J = J_C \sin\left(\varphi + \frac{2V}{eh}t\right) \tag{10}$$

describing an oscillatory current across the junction. The frequency of the oscillation of the critical current is connected to a fundamental constant

$$\frac{2e}{h} \simeq 483.6 \text{MHz}/\mu\text{V} \tag{11}$$

The case discussed here is the ideal case of a Josephson junction driven by an a.c. voltage [177]

$$V = V_0 + V_1 \cos \omega_1 t \tag{12}$$

where ω_1 is the frequency of the a.c. voltage bias. In this case the phase is tuned by the microwave field, via the a.c. Josephson effect

$$\phi = \phi_0 + \omega_p t + \left(\frac{2eV_1}{\hbar\omega_1}\right) \sin \omega_1 t \tag{13}$$

where

$$\omega_p = \sqrt{\frac{2eI_C}{\hbar C}} \tag{14}$$

is the plasma frequency, a parameter already qualitatively introduced in the introduction of this Chapter, which describes the typical resonant frequency of the junction. In order to have a detectable effect ω_1 should be in the range of the plasma frequency. In fact the contribute to the d.c. component is relevant only when $\omega_p = n\omega_1$, that is only when the potential V is an integer multiple of $\hbar/2e$. The effect is the appearance of steps (see Fig. 4a) in the IV curve at voltages

$$V_n = n\frac{h}{2e}\nu \tag{15}$$

where ν is the frequency of the microwaves.

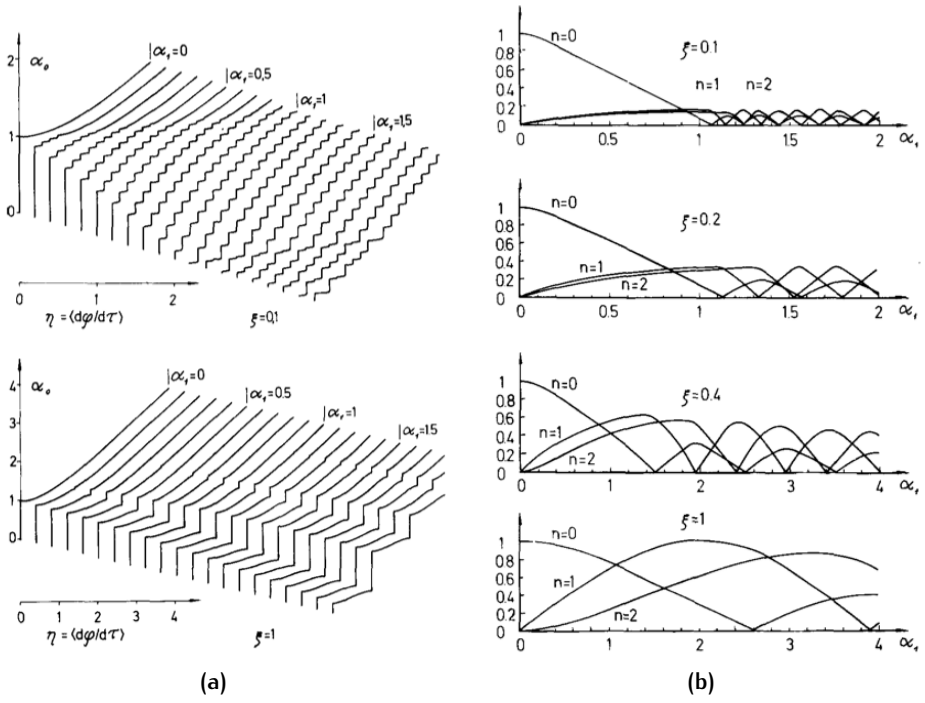

Figure 4: (a) Current - voltage characteristic of a Josephson junction under the effect of a microwave field of increasing power. The figure clearly shows the appearance of the Shapiro steps at the positions given by Eq. 15. In the figure the steps are shown for two different values of the parameter η (see Eq. 17). Curves are shifted for clarity (adapted from Ref. [157]). (b) Modulation of the critical current and of the first two Shapiro step amplitudes for various values of η (see Eq. 17). The curves follows the Bessel behavior for $\eta = 1$, while the width and the amplitude of the modulations is progressively reduced when $\eta \to 0$ (adapted from Ref. [157].

The amplitude of the step is tuned by the amplitude V_1 of the voltage induced by the microwaves across the junction

$$I_n = I_C \, J_n \left(\frac{2eV_1}{h\nu} \right) \tag{16}$$

where $J_n(x)$ is the n^{th} Bessel functions.

The modulations of the step amplitude in a real case is a bit more complicated, since junctions are usually current biased. Moreover, when the $I_C R_N$ product is much bigger than the microwave frequency $\hbar\omega_{RF}/2e$ a numerical approach is required [157].

$$\alpha_0 + \alpha_1 \sin(\eta\tau) = \frac{d\varphi}{d\tau} + \sin\varphi \tag{17}$$

where $\alpha_0 = I/I_C$, $\alpha_1 = I_{RF}/I_C$ are the d.c. and a.c. component of the current bias, normalized to I_C, and $\tau = \Omega t$ is the normalized time, with $\Omega = 2eI_c R_N/\hbar$. As it is shown in Fig. 4b, the parameter $\eta = \hbar\omega_{RF}/2eI_C R_N$ is fundamental for the dynamics of the junction. When $\eta \lessapprox 1$ the modulations follows the ideal Bessel modulation, when instead $\eta \ll 1$, both width and amplitude of the modulations are progressively reduced.

1.2.4 The Sine-Gordon Equation

In the most general case the behavior of the junction in an electromagnetic field can be described by the Sine-Gordon equation [13, 46]

$$\frac{\partial^2\varphi}{\partial x^2} + \frac{\partial^2\varphi}{\partial y^2} - \frac{1}{c_J}\frac{\partial^2\varphi}{\partial t^2} = \frac{1}{\lambda_J}\sin\varphi \tag{18}$$

where $c_J = c\sqrt{d_{eff}/\epsilon_r w}$ is the effective speed of light in the barrier and ϵ_r is the relative dielectric constant of the material.

In the case of zero magnetic field the equation yields

$$\frac{\partial^2\varphi}{\partial t^2} + \omega_p^2 \sin\varphi = 0 \tag{19}$$

$\omega_p = c_J/\lambda_J$ is the plasma frequency, already introduced in Eq. 14. This result points to oscillations of the phase at a frequency given by ω_p. This effect, as discussed in Sec. 1.5.3 has many consequences on the dynamics of the junctions, particularly those influencing the escape dynamics of the phase in moderately damped regime.

1.3 GENERAL THEORY OF SIS AND SNS JUNCTIONS

1.3.1 SIS Junctions

A microscopic derivation of the theory of the Josephson effect, can be achieved in the framework of the Gor'kov equations within the Ambegaokar and Baratoff model [5]. In this model the dissipation-less current flowing through the device can be derived from the Green's function of the Cooper pairs:

$$J_C(T) = \frac{\pi\sigma\Delta}{2e} \tanh\left(\frac{\beta\Delta}{2}\right) \tag{20}$$

where J_C is the critical current density, σ the conductivity of the barrier, $\beta = 1/k_B T$ and Δ is the superconducting gap of the electrodes. This result is the heart of the Ambegaokar and Baratoff model, yielding the temperature dependence of the critical current in the case of a tunneling barrier. This is one of the fingerprint of the junction behavior, giving information on the nature of the barrier. The model also gives the fundamental relation

$$eI_C R_N = \frac{\pi}{2}\Delta \tag{21}$$

which provides an upper limit (defined by superconducting gap of the electrodes) for the $I_C R_N$ quality factor of the junction.

Unconventional hybrid devices are often characterized by the use of exotic materials as barrier. The coherent transport across these barrier can be described by the Josephson equations (Eq. 1, 2), with the inclusion of an unconventional CPR.

1.3.2 SNS Junctions

In the case the barrier is made of normal metal (SNS junctions) the device shows different features from the tunnel case [30, 73, 48, 47]. There are many differences between the features of SNS and SIS junctions, here we focus on two aspects:

1. the behavior of the $I_C(T)$ curve
2. the feature of the IV curve at high bias, nominally the presence of an "excess current"

Further elements determines the features of SNS devices, with remarkable differences with respect to tunnel devices. For instance the

lower capacitance that typically characterizes SNS junctions determines a rounded non-linear behavior of the IV curve, as described in Sec. 1.5.1.

Temperature Dependence of the Critical Current

The $I_C(T)$ curve can be described by the Likharev model [52]:

$$I_C = I_{C0} e^{-L/\xi_n} \tag{22}$$

where ξ_n is the coherence length, qualitatively describing the decay length of the superconductivity in the normal metal [52].

In normal barrier, coherence effect, known as "proximity effect" [51, 134], can be supported by electron-holes states. The basic mechanism of the proximity effect is the "Andreev reflection" [9].

Andreev Reflections

An electron with energy E lower than gap Δ_0 finds no available levels in the superconductor at energy E [92]. However, a coherent transport can be sustained at the Fermi energy by the Cooper pairs. The Andreev reflection, schematically shown in Fig. 5a is based on the transmission of an electron at energy E, through the creation of a Cooper pair. In order to maintain the charge and momentum conservation, a hole state must be formed (and 'reflected') in the normal metal. This process involves no energy transfer and it is reversible, in the sense that an incoming hole annihilates with a Cooper pair, producing a backscattered electron [92].

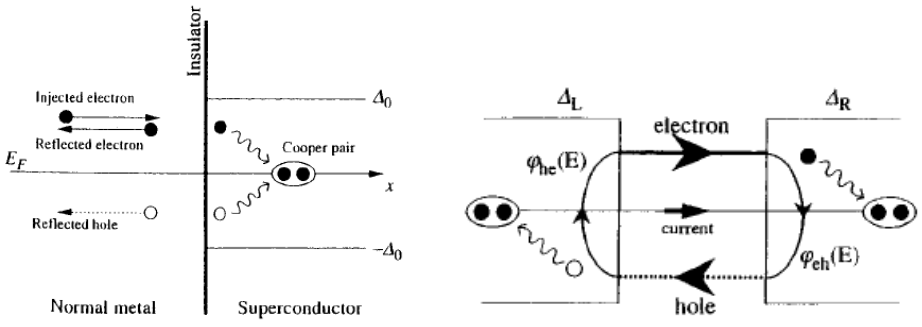

Figure 5: (a) Schematic illustration of the Andreev reflection at a S-N interface. An electron with energy E lower than gap finds no available levels at the energy E. However a transport mechanism involving an electron-hole couple is energetically permitted. (b) Schematic illustration of Andreev bound states in a S-N-S structure. The Antreev reflection at the two SN interfaces creates resonant bound states, which can contribute to the superconducting transport (adapted from [92]).

The presence of Andreev reflections in an SNS structure determines a transport mechanism through resonant bound states, called "Andreev Bound States", as shown in Fig. 5b [92].

The quantity ξ_n introduced in Eq. 22 is the characteristic length of the coherent transport through Andreev bound states.

Excess Current

Although at high voltage ($eV > \Delta$) the IV characteristic of an SNS junctions is linear, with slope R_N, it does not in general fall on the normal-state curve $V = IR_N$, as it does in a tunnel junction (see Fig. 6a). Rather, it is displaced by a constant amount referred to as the "excess current", I_{ex}, determined in the case of a perfectly transparent junction ($z = 0$) by the equation [30]

$$I_{ex}(V) = \frac{4\Delta}{3eR_N} \tanh \frac{eV}{2k_B T} \tag{23}$$

were k_B is the Boltzmann's constant. The excess current can be found by extrapolating the linear part of the IV characteristic at $V = 0$.

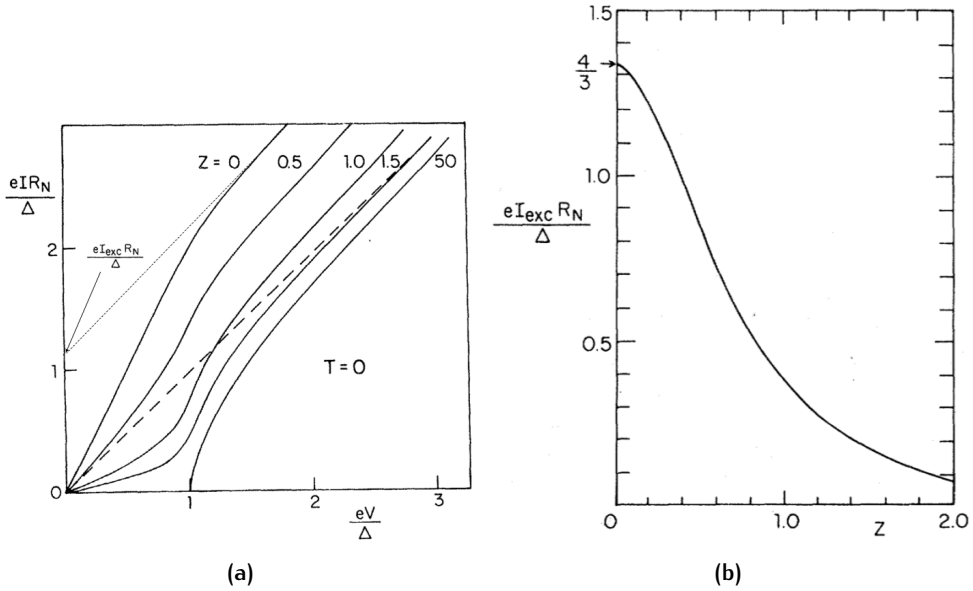

Figure 6: (a) IV characteristics for different values of the strength of the barrier. The tunnel junction ($z = 50$) falls on the normal-state curve $V = IR_N$ (dashed line). As the transparency is reduced, the IV characteristic approaches an ideal S-N-S behavior (corresponding to $z = 0$). Correspondingly an excess current appears from the extrapolation linear part of the IV characteristic at $V = 0$ (dotted line). The amount of the excess is modified by the barrier strength, as shown in panel (b), where the parameter $eI_{ex}R_N/\Delta$ is shown as a function of the barrier strength z (adapted from [30]).

1.3.3 SINIS Junctions

The case of a SNS junction implies a perfect transmission ($z = 0$) of the electrons on the SN interfaces. However, in many experimental conditions this approximation does not hold, and a finite transmission coefficient D should be considered. The transparency of the interface is connected to strength of the barrier z through the relation

$$D = (1/(1 + z^2)) \tag{24}$$

A SINIS junction [201, 69, 31, 32] includes an insulating layer between the superconductor and the normal barrier, that reduces the transmission coefficient D. Changing D it is possible to tune the behavior, from an SNS ($D = 1$) to an SIS ($D = 0$) junction, specifically the excess current follows the non analytical relation [30] shown in Fig. 6a, 6b.

In what follows in the experimental section, we will verify how the transparency D influences:

1. The behavior of the $I_C(T)$ curve
2. The amount of the excess current

The shape of $I_c(T)$ curve is determined by many factors, including if the junction is in a diffusive or a ballistic transport regime [52, 4, 69, 180]. More details are given in the next paragraph.

1.4 BALLISTIC AND DIFFUSIVE TRANSPORT REGIMES

In this paragraph we will discuss the diverse regimes of the coherent transport across a proximity device and their related phenomenology. These notes, far from being exhaustive, are inspired by the uncommon features coming from hybrid structures.

Transport regimes can be first classified on the basis of the ballistic and diffusive regimes of transport. By ballistic we mean that the charge carriers passes through the barrier without experiencing any scattering event. Diffusive, on the other hand, is referred to regimes where the transport is dominated by scattering events (i.e. Mott scattering, electron-phonon, impurities etc). It is worth noting here that diffusive does not necessarily imply the loss of phase coherence, which in many case can be conserved [19].

In addition junctions can be divided in short and long junction, according to the mutual relation between the coherence length ξ_n and the distance d between the electrodes.

1.4.1 Long Junctions

The long junction regime ($d \gg \xi_n$) can be approached in the framework of the Likharev model (Eq. 22) described Sec. 1.3. The coherence length ξ_n describes the coherent transport within the barrier, determined by the uncertainty principle. Therefore it is approximately [52]

$$\xi_n = \tau_T v_F \tag{25}$$

where v_F is the Fermi velocity and $\tau_T = \hbar/(2\pi k_B T)$ is the electron relaxation time.

If the coherence length is larger than the mean free path of the metal, we are in the ballistic regime, where the coherence length is determined by the equation

$$\xi_n = \frac{\hbar v_F}{k_B T} \tag{26}$$

In the diffusive regime, instead, ξ_n is determined by the diffusion coefficient D_n

$$\xi_n = \sqrt{\tau_T D_n} \tag{27}$$

1.4.2 Short Junctions

In the short junction regime ($d \ll \xi_n$), the transport is strongly influenced by the superconducting gap of the material [19, 4]. In this case the distinction between diffusive and ballistic regime is given by the mutual relation between d and the mean free path l_e. This can be summed up in the table below.

Ballistic		Diffusive	
$\xi_n \gg l_e$		$\xi_n \ll l_e$	
$E_{th} = \hbar v_F/d$		$E_{th} = \hbar D/d^2$	
Long	Short	Long	Short
$d \gg l_e \gg \xi_n$	$\xi_n \gg l_e \gg d$	$d \gg \xi_n \gg l_e$	$\xi_n \gg d \gg l_e$
$I_C = e v_F l/L^2$	$I_C = N e\Delta/\hbar$	$I_C \simeq e D_n/L^2$	$I_C \simeq e\Delta/\hbar$

In the table, where N is the number of the transverse modes at the Fermi level which can propagate through the junction. E_{th} is the Thouless energy, which is a fundamental constant for the Josephson Effect in the mesoscopic scales. In fact the notion of long and short

junction can be equivalently given in terms of relative magnitudes of E_{th} and Δ. Particularly the short junction regimes holds when $\Delta \ll E_{th}$ whereas the long junction regime is $\Delta \gg E_{th}$.

1.4.3 Eilenberger Model

An hybrid structure containing superconductors can be described on the basis of the Gor'kov equations. In the case of short SINIS junctions [32], the model can be generalized for junctions of arbitrary length [69]. The critical current can therefore be extracted from the formula

$$I = a\frac{2}{\pi}ek_F^2\frac{k_B T}{h}\sin(\chi)\sum_{\omega_n}\int_0^1 \zeta\, d\zeta \frac{t^2}{Q^{1/2}(t,\chi,\zeta)} \tag{28}$$

where $\zeta = k_x/k_F$ and $t = D/(2-D)$ with D the transparency of the S-N interface, a is the cross section of the junction and

$$Q = \left[t^2\cos(\chi) + (1+(t^2+1)\omega_n^2/\Delta^2)\cosh(2\omega_n L/\mu\hbar v_F) + \right.$$

$$\left. +2t\omega_n\Omega_n/\Delta^2\sinh(2\omega_n L/\mu\hbar v_F)\right]^2 - (1-t^2)^2\Omega_n^2/\Delta^2$$

where $\omega_n = 2\pi k_B T(2n+1)$ are the Matsubara frequencies and $\Omega_n = \sqrt{\omega_n^2+\Delta^2}$ respectively. χ is the phase difference between the two superconducting islands.

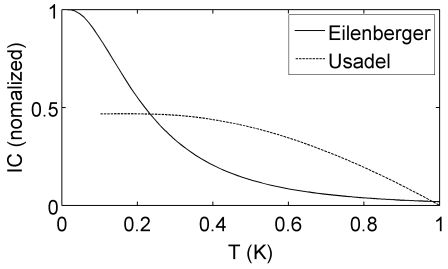

Figure 7: $I_C(T)$ sample curves simulated from Eq. 28 and 29 for a short ballistic (Eilenberger) and diffusive (Usadel) junction more detail on the simulations and on the parameter are discussed in Sec. 5.3.

1.4.4 Usadel Model

A short SNS junction in the diffusive transport regime can be modeled with the Usadel equation [185, 180]

$$\Phi_{S,N} = \Delta_{S,N} + \xi_{S,N}^2\frac{\pi k_B T_C}{\omega_n G_{S,N}}\frac{d}{dx}\left(G_{S,N}^2\frac{d}{dx}\Phi_{S,N}\right) \tag{29}$$

where Φ is a quantity determined by the Green's function G, and ω_n are the Matsubara frequencies. This model can be simplified in the case of a dirty superconductor, yielding the temperature dependence of the critical current density [107]:

$$J = \frac{2\pi\sigma k_B T}{e} \Im m \sum_{\omega_n > 0} \frac{G_N^2}{\omega_n^2} \Phi_N \frac{d}{dx} \Phi_N \tag{30}$$

For junctions with arbitrary length and arbitrary barrier transparency, no analytical expression exists for the Green's functions, though a numerical recipe can be used.

The $I_C(T)$ curve is again the fingerprint of the junction dynamics. Fig. 7 shows a numerical estimation made from Eq. 28 and 29 for a consistent set of junction parameters, showing a remarkable difference. A detailed account on the simulation parameters in the various regime is given in Sec. 5.3.

1.5 RCSJ MODEL

Up to here we have described a Josephson junction as an ideal element, isolated from its environment. A real device is characterized by the presence of parasitic capacitance and by resistive losses through the barrier. The Resistively and Capacitatively Shunted Junction (RCSJ) model [165, 131, 93], described below, accounts for the effects of stray capacitance and resistance of the junction. The case of negligible capacitance is also described in Sec. 1.5.1. This model (RSJ) can be solved exactly [14], including the effects of thermal fluctuations.

The equivalent circuit of the junction should also incorporate the lines used for the measurements, the filtering stages eventually present in the circuit, and the high frequency losses of the device through the substrate. All these elements can be included in the theoretical framework of the RCSJ Model.

The model circuit is an ideal Josephson junction, connected in parallel with a capacitor ad a resistor (see Fig. 8a). The circuit is usually closed on a current generator, therefore giving a current bias to the device. The equation of the circuit is

$$\frac{d^2\varphi}{d\tau^2} + \frac{1}{Q}\frac{d\varphi}{d\tau} + \sin\varphi = \frac{I}{I_C} \tag{31}$$

where

$$Q = \omega_p RC$$

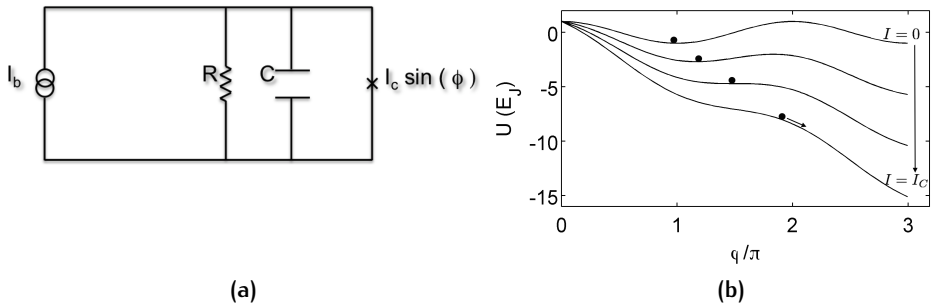

Figure 8: (a) RCSJ equivalent circuit. In this model the dynamics of the device is equivalent to the motion of a particle on the potential in Eq. 32, shown in panel (b) for an increasing value of the bias current.

is the damping factor of the circuit. It has already been introduced in the introduction of this Chapter, and it represents the dissipative term of Eq. 31. ω_p is the plasma frequency of the junction (Eq. 14).

This equation cannot be solved analytically. However a broad phenomenology can be understood considering a mechanical analog of this equation. Indeed it can be readily verified that Eq. 31 is the Hamilton-Lagrange equation of the dynamics of a point particle along the potential (see Fig. 8b)

$$U(\varphi) = -E_J \left(\cos\varphi - \frac{I}{I_C}\varphi \right) \tag{32}$$

where $E_J = \hbar I_C / 2e$ is the Josephson energy.

First introduced by Steward and Mc Cumber in 1968 [165, 131]. After the discovery of macroscopic quantum behavior in JJs [54, 123, 43] the model has progressively turned out to be a powerful tool to describe the dynamics of the junction, including its quantum nature. The dimension along which the particle 'moves' is indeed the Josephson phase, a macroscopic degree of freedom of the device. This "phase particle" is a mechanical analog of the junction dynamics, capturing the nature of the device dynamics and its quantum codes.

1.5.1 Under-damped and Over-damped IV Characteristics

The current voltage characteristic of a junction can be qualitatively explained very easily in terms of the RCSJ model. In fact when the bias current is zero the phase particle is trapped in one of the minima on the potential. In this case we know (from Sec. 1.2.4) that the phase oscillates at the plasma frequency, and this is reflected into an oscillation of the particle around the minimum of the potential. When the current bias is

increased the particle is still trapped into a local minimum, but the plasma frequency changes with the current

$$\omega_p = \omega_{p0}\left(1-\left(\frac{I}{I_C}\right)^2\right)^{(1/4)} \tag{33}$$

Ramping up the bias current, the tilt of the potential Eq. 32 is increased (see Fig. 8b). When the bias current exceeds I_C the minima disappears and the particle switches to a 'running' state. In this state the particle is running down the potential, therefore the phase is changing in time, meaning a finite difference of potential across the junction (cfr. Fig. 8b).

The dynamics is significantly influenced by the damping factor: when the damping is high ($Q \lesssim 1$) the IV curve is completely determined by the bias current. In this case the Eq. 31 is analytically solvable [14]. When instead the damping effect can be neglected ($Q \gg 1$), the IV curve shows up an hysteresis effect. In this regime a stochastic switching from the metastable, zero voltage state to a resistive state is detected. This is the case of high capacitance junctions.

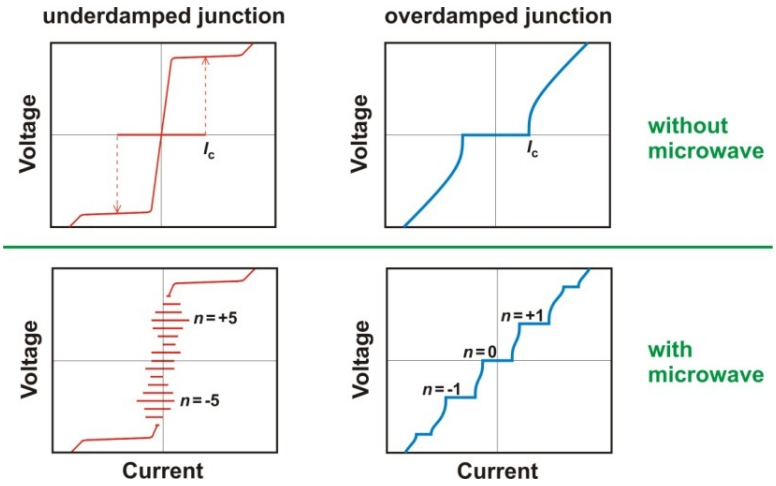

Figure 9: (above) Sketch of IV curves in under-damped (left) and in over-damped (right) regimes. The figure below shows how Shapiro steps appear in IV curves with different features (adapted from [99])

RSJ Model

As mentioned before, the case of over-damped junctions can be treated analytically. In this case, the capacitance effects of the junction are negligible, therefore the model is also called RSJ [14].

The effects of thermal fluctuations can also be included in the model through a thermal coefficient $\gamma = \hbar I_C(T)/ek_BT$ yielding the thermal average of the potential as a function of I, and γ:

$$\langle V \rangle = \frac{2}{\gamma} R_N I_C \frac{e^{\pi\gamma i} - 1}{e^{\pi\gamma i}} \mathcal{I}^{-1} \tag{34}$$

where $i = I/I_C$ is the normalized current, γ is the thermal coefficient and

$$\mathcal{I}^{-1} = \int_0^{2\pi} e^{-\frac{\gamma}{2} i\varphi} \, \mathcal{I}_0 \left(\gamma \sin \frac{\varphi}{2} \right) d\varphi$$

is a normalization factor, $\mathcal{I}_0$ is the 0 order modified Bessel function of the first kind and k_B is the Boltzmann's constant.

Figure 10 shows the result of a numerical calculation of Eq. 34. Increasing the γ the IV curves become more and more rounded, and for $\gamma \to \infty$ the IV goes towards an ohmic behavior.

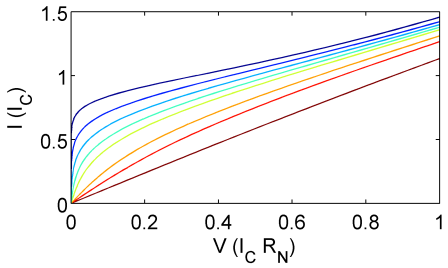

Figure 10: IV curves of an over-damped junction for different values of the thermal coefficient γ. The curves are obtained from a numerical estimation of Eq. 34 with $1 < \gamma < 47$.

Underdamped Regime

When $Q \gg 1$ (Under-damped junctions) the IV is characterized by an hysteretic behavior (see Fig. 9). This effect can be qualitatively described as an inertial effect of the particle in the running state. When the current is ramped back to zero the value of the bias necessary to stop the motion of the particle (called re-trapping current I_r) is lower than I_C, and ideally $I_r = 0$ in the case of no dissipation. The value of the re-trapping current is given by a balance between the dissipation of the resistance and the kinetic energy of the phase particle, and it can be estimated from the equation [132, 202, 179]

$$Q^2 = \frac{2 - (\pi - 2) I_r/I_C}{(I_r/I_C)^2} \tag{35}$$

As discussed above, the under-damped dynamics is characterized by stochastic switching events from the local minimum of the potential.

The study of the escape dynamics is a powerful tool to characterize the dynamics of the junction.

1.5.2 Escape dynamics

When the bias current approaches I_C, the junction can escape from the local minimum of the potential. This effect is responsible for the hysteresis in the IV curve (Fig. 9). There are two main mechanisms inducing the switching: thermal effects and quantum effects (see Fig. 11a).

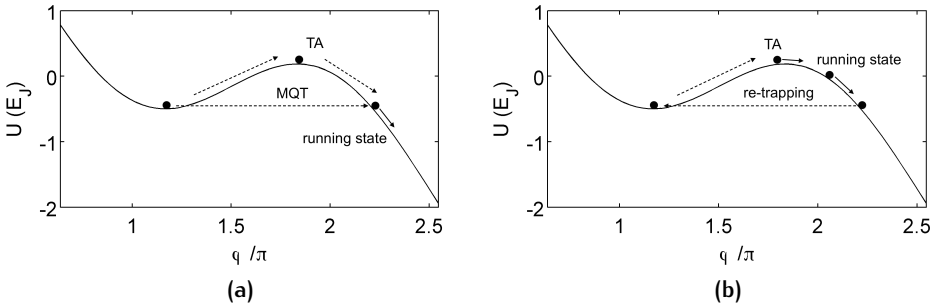

Figure 11: (a) Sketch of the escape dynamics from a local minimum of the potential Eq. 32. The escape can be triggered by a thermal mechanism (Eq. 36) or by a quantum mechanism (Eq. 38). (b) Re-trapping of the particle from a running state. The re-trapping rate is given by Eq. 41

The thermal effects can be theoretically treated within the framework of the Kramers problem of a thermal escape from a potential [74]. The probability per unit time to escape the potential is given by the so called "escape rate" [68]

$$\Gamma_T = \Gamma_{0T} \frac{\omega_p}{2\pi} \exp\left(\frac{\Delta U}{k_B T}\right) \tag{36}$$

Γ_{0T} is a pre-factor containing a thermal dependence

$$\Gamma_{0T} \simeq 4\left[(1 + Qk_B T/1.8\Delta U)^{\frac{1}{2}} + 1\right]^{-2}$$

and

$$\Delta U(I) = E_J\left(\sqrt{1 - \frac{I}{I_C}} - \cos^{-1}\left(\frac{I}{I_C}\right)\right) \tag{37}$$

is the potential barrier created by the potential (Eq. 32) at the value I of the bias current. Quantum effects are related to tunneling events of the phase particle across the potential barrier ΔU (see Fig. 11a). The

expression of the quantum escape rata can be obtained in the WKB approximation [34, 190]

$$\Gamma_q = \Gamma_{0q} \frac{\omega_p}{2\pi} \exp\left[-7.2 \frac{\Delta U}{\hbar\omega_p}\left(1 + \frac{0.87}{Q}\right)\right] \tag{38}$$

where

$$\Gamma_{0q} \simeq (864\pi\Delta U/\hbar\omega_p)^{\frac{1}{2}}$$

The main difference between the two contribution is that in the thermal regime the dynamics is determined by the exponent ($\Delta U/k_B T$), which explicitly depends on the temperature, while in the quantum regime the exponent is temperature independent ($\Delta U/\hbar\omega_p$). To express the experimental measurements of the escape rate in a way that is as independent as possible of the parameters of the junction, a parameter, called "escape temperature" (T_{esc}), is traditionally introduced [54]. In the thermal regime the escape temperature coincides with the temperature of the bath, while in the quantum regime ($T_{esc} = \hbar\omega_p/k_B$). The model can therefore be re-parametrized in therms of T_{esc}

$$\Gamma(I) = \frac{\omega_p}{2\pi} e^{-\frac{\Delta U}{k_B T_{esc}}} \left(\Gamma_{0q} + \Gamma_{0T}\right) \tag{39}$$

In the experiment a current ramp is given to the junction. When the current bias approaches I_C the junction undergoes a stochastic switching. The value of the current at which the switching happened is therefore registered (switching current), and the junction is reset (i.e. the current is put to zero). Multiple ($\simeq 1000 - 10000$) events are therefore collected, to create a switching current distribution (SCD) (see Fig. 12).

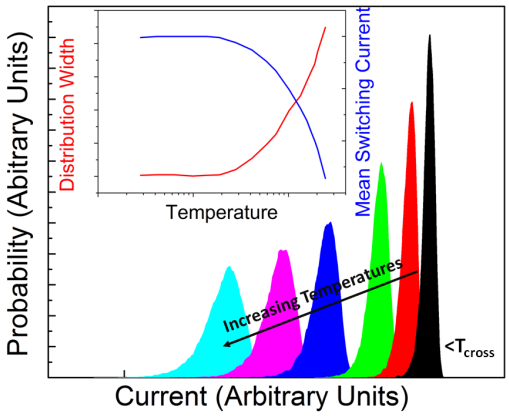

Figure 12: Sketch of switching current distribution for various temperatures. As the temperature is increased, the histograms become broader, and their mean value progressively decreases. The inset shows the mean value and the width of the SCD as a function of the temperature.

This is related to the escape rate through the equation [68]

$$\Gamma(I) = \frac{\gamma P(I)}{1 - \int_0^I P(i)di} \tag{40}$$

The experimental signature is the behavior of the SCDs as function of the temperature. In MQT regime the histograms overlap [172, 123, 54] as the the mechanism of the escape is temperature independent. This is reflected in a constant value of T_{esc}, which is determined by the quantum noise of the junction. In thermal activation regime the SCDs progressively becomes larger and their amplitude decreases as shown in Fig. 12. The width of the histogram increases following a universal scaling law $T^{2/3}$ [108]. This power law is determined within the Kramers model [74, 68].

Peculiar features can be detected in hybrid barriers [108, 45], or in the case of superconducting nanowires [109, 10, 159], generally related to the particular nature of the junctions. For instance a theoretical description of the phenomenology of the MQT in a ballistic regime has never been completely developed up to now.

1.5.3 Moderate Damping: Re-trapping and Phase Diffusion

Once the phase particle has escaped from the local minima of the potential, the junction is in a running state (corresponding to the resistive branch of the IV curve). In this state the energy gained by passing from one well to the next one barely exceeds the dissipative losses and the particle eventually gets re-trapped (see Fig. 11b) [93, 124, 59], diffusing to the next wells. This effect manifests in the behavior of the SCD. Specifically, the width of the distribution decreases when the temperature is increased. The SCD histograms move to lower currents till they touch the limit $I_R = (4I_C/\pi)1/Q$. This phenomenon can be well described by the re-trapping rate [21]

$$\Gamma_R = \frac{I - I_r}{I_C}\omega_p\sqrt{\frac{E_J}{2\pi k_B T}}e^{-\left(\frac{E_J Q^2 (I-I_r)^2}{2k_B T I_C^2}\right)} \tag{41}$$

where $i_r \simeq 4I_C/\pi Q$. Here is worth noting that the re-trapping is a thermal phenomenon in the sense that it is enhanced by thermal fluctuations [122].

Eq. 41 strictly holds in the limit $Q \gg 1$. In the moderate damping regime this model still applies in a good approximation [104], but the dynamics involves multiple escape and re-trapping events [122]. This behavior is determined by the enhanced re-trapping rate at lower Q ($\Gamma_R \simeq e^{-\frac{E_J Q}{k_B T}}$).

First introduced by Kautz and Martinis [93], the main experimental signature was detected in the appearance of a finite voltage on the IV curve of moderately damped devices near I_C. Only in 2008 Fenton and Warburton [59] introduced a quantitative description of the phenomenon, thanks to the introduction of Monte Carlo methods to describe the dynamics of multiple escapes and re-trappings. This dynamics significantly influences the behavior of the SCDs, and determines a progressive shrinking of the histograms for an increasing temperature [59, 122].

Frequency Dependent Damping

A complete description of the dynamics of moderate Q junctions requires a slight generalization of RCSJ model, taking into account the frequency effect on the effective shunting circuit of the junction [93].

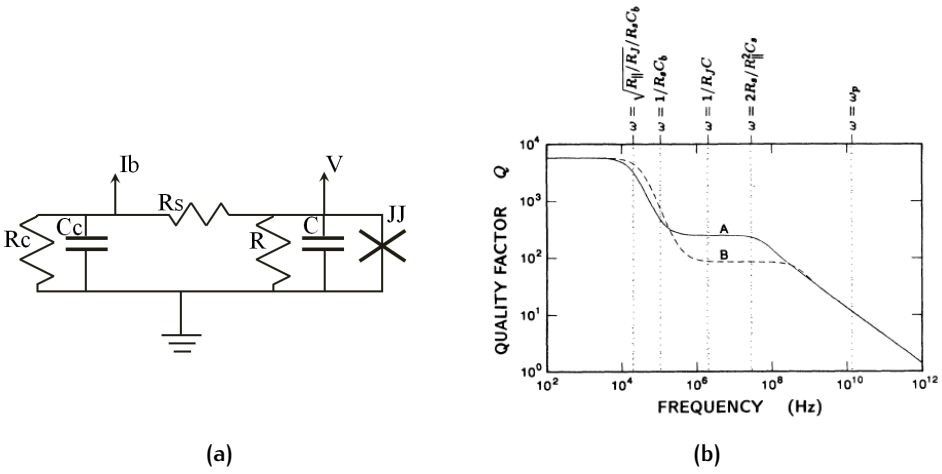

Figure 13: (a) Equivalent circuit to describe a frequency dependent damping. (b) Effective quality factor as a function as a function of the frequency of the current bias. The rwo plateaus corresponds to Q_H and Q_L.

The frequency dependent damping factor is $Q(\omega) = \omega_p C/G(\omega)$, where ω_p is the plasma frequency of the junction, C is the shunt capacitance and $G(\omega)$ is the frequency dependent leads loaded on the junction. The equivalent circuit is represented in Fig. 13a: R_b and C_b models the external impedance felt by the junction, R_s is the resistance of the transmission line, R and C are the intrinsic shunt capacitance and resistance of the junction. At low frequencies the load on the junction is basically given by the shunt resistance of the junction (R), in parallel with R_s and R_c, while at high frequencies the external circuit capacitance behaves like a short, therefore the load is determined by the impedance of the transmission line R_s. The resulting frequency

dependent damping factor (Fig. 13b) shows two flat plateaus: the low frequency one gives the low frequency damping factor Q_L whereas the high frequency one gives Q_H.

Classically the low frequency damping (Q_L) should play no role in the dynamics of the PDR, since the phase particle should only feel the effect of the high frequency damping factor (Q_H determined by the damping of the external circuit), but there are some evidence of a nontrivial dependence of the thermal behavior of the width of the SCD $w(T)$ from the low frequency damping factor Q_L, as described in Sec. 6.3.2.

To sum up the escape dynamics is a very powerful tool to characterize the junction dynamics. The study of the SCDs reveals the nature of coherence and dissipation of the device, including the features traditionally related to the dynamics of multiple escapes and re-trappings. This is the characteristic regime of unconventional hybrid devices and nano-structures. Macroscopic quantum phenomena are typically manifested at the lowest temperatures, and determines the main switching mechanism of the devices.

2 HALL EFFECT: A SHORT SUMMMARY

In the last Chapter we have extensively described the physics of the Josephson effect, that is one of the most fascinating field where quantum phenomena appear on a macroscopic scale. The next paragraphs are dedicated to the Hall (Sec. 2.1.1) and quantum hall effect (QHE) [98] (Sec. 2.1.3). A short review of the main concepts of topological insulators [136, 81, 8] (Sec. 2.2) is also included, with a special focus to those features connected to the manifestation of their topological nature in the study of the Shubnikov - de Haas oscillations [152, 185, 6] (Sec. 2.3). Specifically we discuss how the presence of a zero energy Landau level, which is typical of Dirac electrons, manifests through a Berry phase φ_B [25, 8], which is expected to be π in topological insulators and 0 in topologically trivial materials. A final paragraph (Sec. 2.4) is devoted to the introduction of topological superconductors and Majorana bound states.

2.1 INTRODUCTORY REMARKS

A two-dimensional electron gas (2DEG), embedded in a perpendicular magnetic field shows up quantized energy levels:

$$E_n = \hbar\omega_c(n + \frac{1}{2}) \tag{42}$$

known as Landau levels. Here the quantity ω_c is the cyclotron frequency, given by

$$\omega_c = \frac{eH}{cm} \tag{43}$$

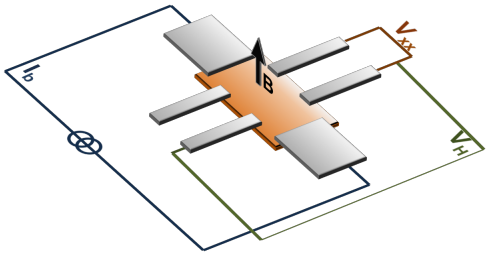

Figure 14: Sketch of a Hall bar in a perpendicular magnetic field. The device is biased with a current I_b. The Hall voltage V_H and the longitudinal voltage V_{xx} are measured between the voltage probe as shown in figure.

The device to study Hall effect is the Hall bar, which is a six terminal device. Two contacts are used to give a bias current I, the remaining four contacts can be used to measure the voltage difference between different points of the device. Specifically we are interested in V_{xx} and V_H (see Fig. 14), which are used to define the longitudinal and transversal resistance

$$\begin{aligned} R_{xx} &= V_{xx}/I \\ R_{xy} &= V_H/I \end{aligned} \tag{44}$$

As a consequence of the formation Landau levels [110] the transversal conductance is quantized in units of

$$G_0 = \frac{2e^2}{\hbar} \tag{45}$$

The value of $G_0 = 7.74809 \cdot 10^{-5}$ S is a constant of fundamental interest both for the physics of semiconductor [7, 98] an for mesoscopic physics [33].

Due to the strong magnetic field, the current flows only on the edges of the Hall bar, while the bulk is a sort of insulating material. This makes the QHE a topologically non trivial state of matter [178, 11, 151].

2.1.1 Classical Hall Effect

The Hall effect was introduced by the studies of E. H. Hall [78], involving the appearance of a transverse "Hall" voltage V_H, when a magnetic field was applied to a metallic or semiconducting bar. When the magnetic field is not strong enough to induce coherence effect related to the quantum confinement, the Hall voltage is proportional to the magnetic field and to the bias current I. Therefore it is possible to define a coefficient

$$R_H = -\frac{V_H t}{ne} \tag{46}$$

called "Hall coefficient" (here t is the thickness of the Hall bar). This was the regime studied by Hall et al. [78] in the end of the XIX century.

In the linear regime, the Hall coefficient is related to the carrier density of the system, via the relation

$$n = -\frac{1}{R_H q} \tag{47}$$

where q is the charge (including sign) of the carriers. It is possible to directly determine the sign of this charge q, which in metallic Hall bars is typically negative (i.e. the charge is transported by the electrons), while for instance in semiconductors it can either be positive or negative, depending on the doping of the material.

From the value of the charge carrier density and the conductivity one can also infer the value of the electrical mobility

$$\mu = \frac{\sigma}{ne} \tag{48}$$

If the system is an ideal 2D electron gas (2DEG), the thickness t is an ill defined quantity, therefore one can define

$$R_H^{2D} = -\frac{V_H}{n_{2D} e} \tag{49}$$

yielding

$$n_{2D} = -\frac{1}{R_H^{2D} e} = -\frac{1}{R_H e t} \tag{50}$$

In the case of a purely 2D system the Hall coefficient is defined by Eq. 49, while in 3D systems this quantity should be normalized to the thickness t of the Hall bar [164] (as in Eq. 46). Clearly, R_H^{2D} and R_H^{3D} cannot be simultaneously independent of the sample thickness t. Therefore one can infer if the transport takes place in the bulk of the flake or in the 2D edge states by studying the thickness dependence of the 2D and 3D Hall coefficients.

There is a great deal of phenomena determining a quasi 2D transport mechanism. Classically these phenomena are observed in field effect transistors and heterostructures, due to the effect of a quantum confinement [50]. Hall measurements in graphene samples [206, 144, 145] show unconventional properties [143], due to the presence of a zero energy Landau level, which is peculiar of Dirac electrons. These features are discussed in more detail in Sec. 2.1.3, 2.3.

More recently new insights on transport in low dimensions have been taken by the introduction of the topological insulators (see Sec. 2.2). In this case the transport on a 2D channel is made possible by a

mechanism of topological protection of the edge states [66, 8, 81]. In these materials an unwanted contribution can also arise from impurity states in the bulk of the material. Therefore a hybrid 2D - 3D transport state can be observed [164, 70].

In the case of a mixed transport, modeled as a parallel of a 2D and a 3D channel [164], the result is given by the equation:

$$\begin{aligned} R_H^{2D} &= \frac{n_{3D}\alpha^2 t + n_{2D}}{e(n_{3D}\alpha^2 t + n_{2D})^2} \\ R_H^{3D} &= R_H^{2D} t \end{aligned} \tag{51}$$

where α is the ratio between the bulk and the surface mobility. It is expected to be in the order of the unity in this model.

2.1.2 Drude Model

Classical electrodynamics relates the electric field to the current density by means of the Ohm's law

$$\vec{E} = \boldsymbol{\rho}\vec{J} \tag{52}$$

where $\boldsymbol{\rho}$ is the resistivity tensor. This is a fundamental quantity to describe the phenomenology of magnetoresistance (MR) phenomena. This quantity is experimentally accessible. In fact, provided that the material is homogeneous and isotropic, there are only two independent elements of the resistivity tensor:

$$\boldsymbol{\rho} = \begin{pmatrix} \rho_{xx} & \rho_{xy} \\ \rho_{xy} & \rho_{xx} \end{pmatrix} \tag{53}$$

ρ_{xx} and ρ_{xy} are simply related to the quantities R_{xx} and R_{xy} (see Eq. 44):

$$\begin{aligned} \rho_{xx} &= \frac{R_{xx} w}{l} \\ \rho_{xy} &= R_{xy} \end{aligned} \tag{54}$$

Here l and w are the length and the width of the Hall bar, respectively.

By simple inversion of Eq. 55, we have $\vec{J} = \boldsymbol{\sigma}\vec{E}$, where the conductivity tensor $\boldsymbol{\sigma} = \boldsymbol{\rho}^{-1}$ is

$$\boldsymbol{\sigma} = \begin{pmatrix} \sigma_{xx} & \sigma_{xy} \\ \sigma_{xy} & \sigma_{xx} \end{pmatrix} \tag{55}$$

where

$$\begin{aligned} \sigma_{xx} &= \rho_{xx}/(\rho_{xy}^2 + \rho_{xx}^2) \\ \sigma_{xy} &= -\rho_{xy}/(\rho_{xy}^2 + \rho_{xx}^2). \end{aligned} \tag{56}$$

In the simple case of Drude theory, for instance, this can be obtained from the Lorentz's law acting on a gas of free carriers, yielding the result

$$\begin{aligned} \boldsymbol{\sigma}(H) &= \sigma_0 \frac{1}{1+\omega_c^2\tau^2} \begin{pmatrix} 1 & -\omega_c\tau \\ \omega_c\tau & 1 \end{pmatrix} \\ \sigma_0 &= \frac{ne^2\tau}{m} \end{aligned} \tag{57}$$

where τ is the relaxation time, that is the average time between two scattering events.

We can account for more than one kind of carrier [94] using the equation set

$$\begin{aligned} \sigma_{xx}(B) &= \frac{l}{w}\left(e\left(\frac{n_1\mu_1}{1+\mu_1^2B^2}+\frac{n_2\mu_2}{1+\mu_2^2B^2}\right)\right) \\ \sigma_{xy}(B) &= eB\left(\frac{n_1\mu_1^2}{1+\mu_1^2B^2}+\frac{n_2\mu_2^2}{1+\mu_2^2B^2}\right) \end{aligned} \tag{58}$$

Upon considering the Onsager's reciprocal relations [76], we can see that σ_{xx} is symmetric with respect to magnetic field $\sigma_{xx}(B) = \sigma_{xx}(-B)$), while σ_{xy} is antisymmetric ($\sigma_{xy}(B) = -\sigma_{xy}(-B)$). The same symmetry relations applies to the resistance tensor.

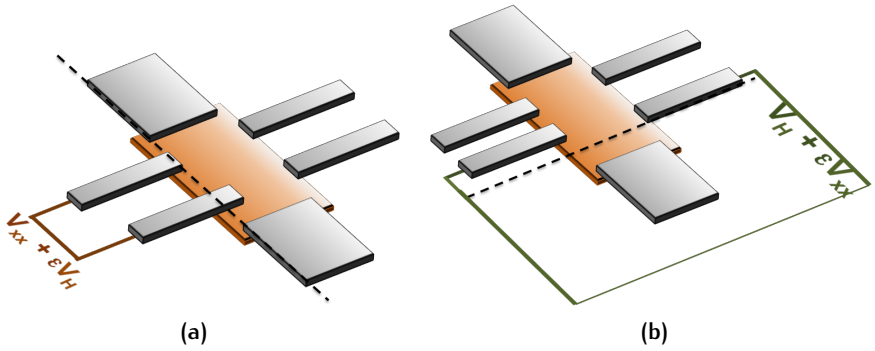

Figure 15: Anomalies in the geometry of a Hall device can induce deviation of the longitudinal and transversal voltages. In fact a misalignment con induce an intermixing between the two components.

Experimentally, the presence of anomalies in the geometry of the device can induce deviations from the ideal case (see Fig. 15), therefore the experimental quantities cannot be in general fully symmetric or antisymmetric.

2.1.3 Quantum Hall Effect

At high magnetic fields

$$\mu B \gg 1 \tag{59}$$

the charge carriers are able to close at least one loop around the cyclotron orbit with negligible decoherence, which is in fact induced by the scattering phenomena. The conductance tensor in the collision-less regime is given by

$$\sigma(H) = \sigma_0 \begin{pmatrix} 0 & -1 \\ 1 & 0 \end{pmatrix} \tag{60}$$

When the Fermi energy

$$E_F = \frac{\pi \hbar n_{2D}}{m} \tag{61}$$

lies between two Landau levels (Eq. 42), the system is collision-less, this means that a current flows along the x direction with no electric field (i.e. $R_{xx} = 0$). Correspondingly the transversal conductance G_{xy} assumes an integer multiple of G_0 [178].

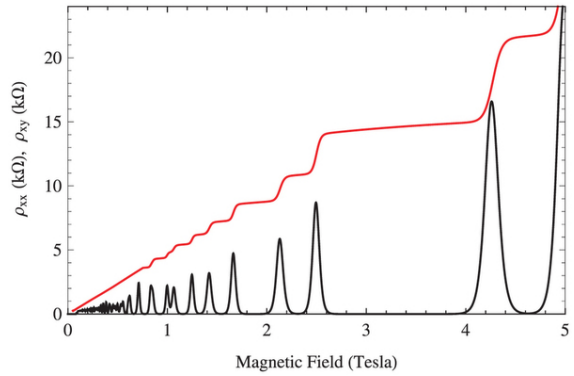

Figure 16: Longitudinal and transversal resistance in quantum Hall effect. ρ_{xy} (in red) presents the appearance of plateaus, which become more and more pronounced as the magnetic field is increased. Correspondingly ρ_{xx} (in black) shows pronounced peacks.

The position of the Fermi energy with respect to the Landau levels can be tuned either by changing the magnetic field (i.e. moving the position of E_n, see Eq. 42) or depleting the channel with a gate (i.e. moving the position of E_F see Eq. 61). When E_F passes through a Landau level, the system is no longer in the collision-less approximation, this corresponds to a peak of G_{xx} and to the passage of G_{xy} form a plateau to one another (see Fig. 16).

Landau Levels in 3D Systems

Landau levels are an exclusive features of 2DEG systems. In a 3D electron gas in magnetic field, Landau levels are broadened into bands. In this case each Landau level corresponds to a free particle parabolic band (see Fig. 17a)

$$E_{N,k_z} = \left(N + \frac{1}{2}\right)\hbar\omega_c + \frac{\hbar^2 k_z^2}{2m} \tag{62}$$

with the density of states (shown in Fig. 17b) given by the expression [77]

$$D(E,H) = \frac{1}{2}\hbar\omega_c A \sum_{N=0}^{\infty} \frac{1}{\sqrt{E - \left(N + \frac{1}{2}\right)\hbar\omega_c}} \Theta\left(E - \left(N - \frac{1}{2}\right)\hbar\omega_c\right) \tag{63}$$

where $A = 4\pi V(2m)^{3/2}h^{-3}$.

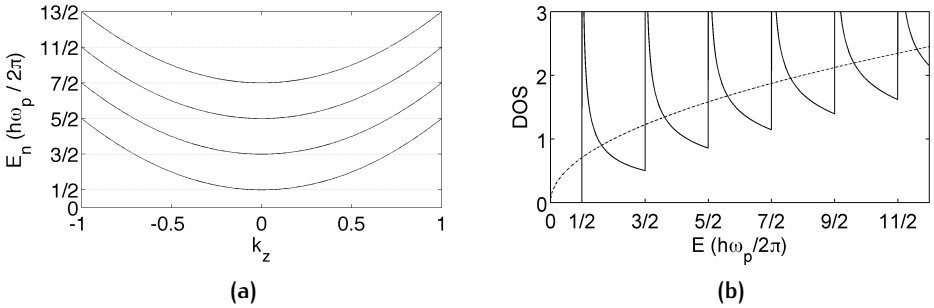

Figure 17: (a) Parabolic bands of an electron gas in a high magnetic field. Each parabolic band corresponds to a Landau level in 2D. (b) Density of state of the 3D electron gas, presenting poles in correspondence of the energies of the Landau levels.

The density of states presents poles in correspondence to the position of Landau levels. Therefore it is possible to detect features related to LLs in 3D systems as for instance Shubnikov de Haas oscillations [166], described in more detail in Sec. 2.3.

Quantum Hall Effect and Topological Invariants

The quantum Hall effect, as discussed before, can be intended in the framework of topological field theory [178]. The two main features characterizing the quantum Hall states are: 1) the presence of edge currents 2) the quantization of Hall resistance.

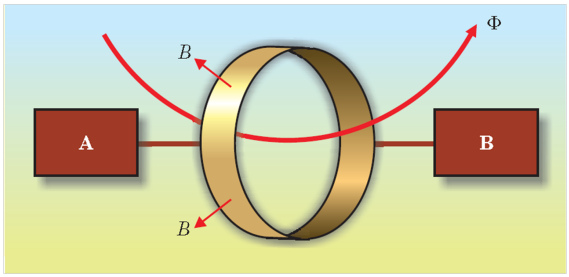

Figure 18: Sketch of the gedanken experiment proposed by Laughlin (adapted from [11]).

1. The current flows without a voltage along the x axis of the bar (i.e. $V_{xx} = 0$). This current is carried by the edge states of the system. In the quantum Hall state there is an edge state, represented by a 1D system. The edge state is chiral and the electrons are localized on different sides of the Hall bar (see Fig. 19a), thus preventing any intermixing between the left movers and the right movers. This protects the charge carriers from random collisions, giving the notion of a dissipation-less current.

2. The quantization of the Hall resistance is connected with the concept of adiabatic curvature [178, 85]. It is worth mentioning here the gedanken experiment proposed by Laughlin [110]. He interpreted the QHE as a quantum pump.

   Let us suppose to close an Hall bar on itself, along the direction of the current, thus creating a closed ribbon. The magnetic field is everywhere orthogonal to the ribbon, while the Hall voltage can be detected between the edges. Laughlin introduced a fictitious magnetic flux treading the loop (see Fig. 18). Using simple gauge invariance arguments it is possible to show that, by changing the flux by a unit flux quantum ($\Phi_0 = hc/e$), the system remains unchanged, this phenomenon was first observed in silicon metal-oxide-semiconductor field-effect transistor, thus giving the feature of the flat plateaus of the conductance.

There is no guarantee that the charge transported in each cycle is the same. The answer to the Hall quantization have to be sought in the topology [11], which connects the Hall conductance to the adiabatic curvature of the parameter space. However, the details of the topological approach to the QHE, and to the topological phase transitions are theoretically extremely complex, and falls beyond the purposes of this work.

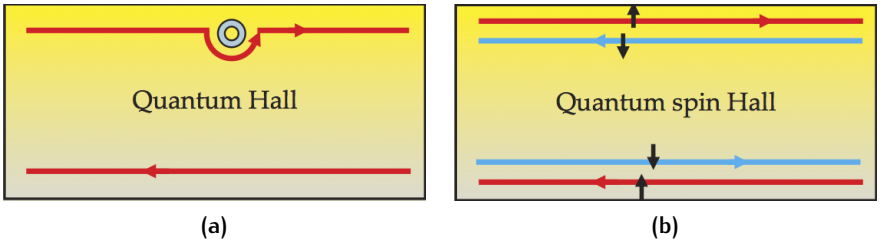

Figure 19: (a) Edge states of a Hall bar in a in a the quantum Hall state. The edge states, represented by 1D states, are spatially separated. (b) Spin current separation of the quantum spin Hall state. Each edge of the system is characterized by two counter-propagating currents with opposite spin (adapted from [151]).

2.2 TOPOLOGICAL INSULATORS

Topological insulators (TI) are a new class of material generating a surge of research activity. Historically the first topological state of matter was the QHE [178], but the word topological insulator was introduced much later [136], after the discovery of the quantum spin Hall effect [101, 24]. The materials which presents this effect are normally referred as 2D topological insulators.

The unconventional features of TI are related to their uncommon band structure [24, 63, 64], generated by their strong spin-orbit coupling. Specifically in heavy elements (Bi, Te, Sb and Hg) compounds with large spin-orbit coupling, the p band can be pushed down so much in energy to generate an inversion between the p and s band of the material. When the topological insulator is terminated and faces an ordinary insulator (including the vacuum), a matching condition must apply to the p and s bands (see Fig. 20). The consequence is the creation of a crossing point between the bands at the edge of the material. Near the crossing point the dispersion of the states is linear, thus recreating the energy dispersion of massless Dirac fermions in 1D.

2.2.1 2D Topological Insulators

Recently it has been shown that systems with strong spin-orbit coupling can show a state similar to the QHE, but in absence of the magnetic field. In this case there are two helical edge states due to the spin-orbit scattering. Counter-propagating electrons have also opposite projections of the spin along the direction of motion (see Fig.19b). First observed in CdTe/HgTe/CdTe quantum wells [101, 24], this effect is usually considered as the birth of a the topological insulators [136, 81, 8].

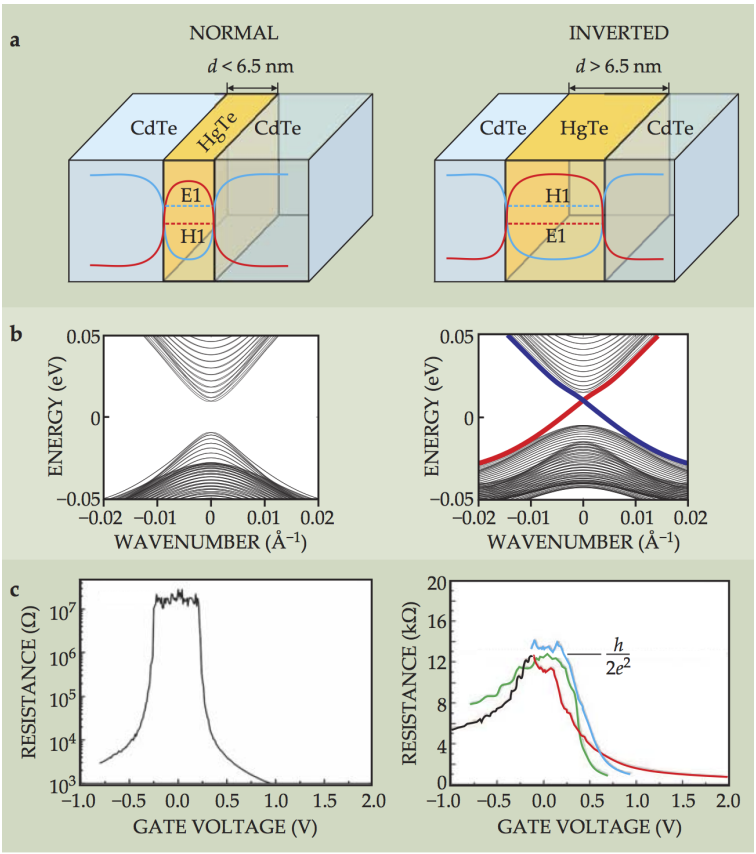

Figure 20: Schematic explanation of the König experiment [101]. (a) Sketch of the s and p bands of the system in the inverted and non inverted (i.e. trivial) state. The corresponding band structure is shown in (b), where the Dirac cone is depicted in red and blue. The cone is a manifestation of the bend inversion, in correspondence of the edge of the system. (c) Experimental signature of the topological state, consisting of the appearance of a transport channel with conductance G_0 when the thickness of the bar exceeded the critical thickness d of 6.5 nm. Below the critical thickness the conductance shows a divergence of at least 10^7 Ω. The figure is adapted from [151]

The effect, in fact, involves a crossing between s and p bands, detected when the thickness of the HgTe was above a critical thickness of 6.5 nm. The effect reported in Ref. [101] is the creation of a conduction state with conductance G_0. Below the critical thickness, the structure showed zero conductance, as expected in the case of a quantum well with a normal electronic structure.

2.2.2 3D Topological Insulators

3D topological insulators where theoretically predicted in 2006 [66, 137, 156], and experimentally found in the rare earths materials [63, 192, 205, 37, 86, 82]. In 3D the edge state is a surface (i.e. a 2D electron gas) with a Dirac dispersion

The simplest 3D topological insulator can be thought as a stack of 2D TIs [100]. In this case the surface edge state exists but it is not protected against a weak disorder. Therefore it is experimentally rather difficult to observe such states [81], thus referred as 'weak'. However, in 3D it is possible to have different topological states, called 'strong' TIs, which are topologically protected. By topological protection we mean that [8]

1. the existence of a gapless edge state is guaranteed as long as the time reversal symmetry is conserved
2. the backscattering of electrons with momentum $+\mathbf{k}$ into electrons with momentum $-\mathbf{k}$ is prohibited
3. the presence of a π Berry phase, which protects the electrons to weak localization ((see also Sec. 2.3.1 and 2.3.3)).

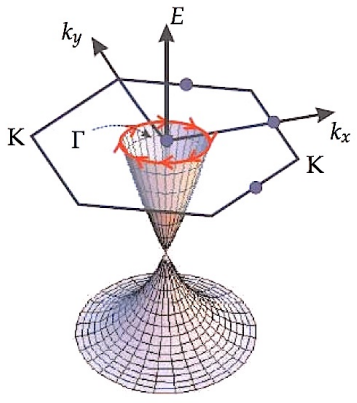

Figure 21: Energy dispersion of the topological edge state of a 3D TI. The spin and the orbital momentum are locked together, to create a chiral edge state. The energy has a linear dispersion, thus creating the feature of a Dirac cone (adapted from [151]).

Strong TIs are characterized by a metallic 2D surface state with an odd number of Dirac cones [63, 66]. The spin and the orbital momentum **k** are locked together, thus generating chiral states in the Dirac cone, where the direction of the spin is everywhere tangential to the cone (see Fig.21). This circumstance is more complex than the spin separation, which instead characterizes 2D and weak TIs.

The presence of fractional topological classes in 3D, which are prohibited in 2D, can be intuitively understood with a simple argument [136]. In three dimensions it is possible to create a knot (for example with a rope), this feature is impossible to be recreated on a 2D surface (for instance marking a line with a pencil) without overlapping the line (thus in fact invoking a third dimension). The rope represents a topological class which describes strong 3D topological insulators, as the examples shown in Fig. 22.

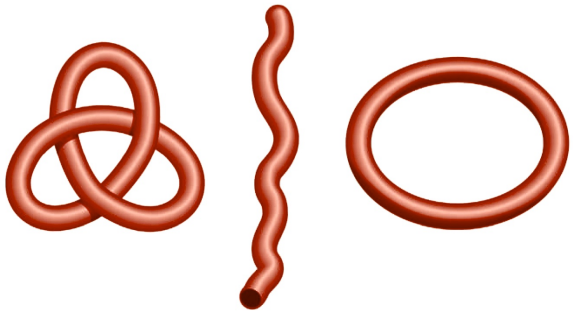

Figure 22: An illustration of topological change and the resultant surface state. The knot is a topological insulator, and the loop is an ordinary insulator. Because there is no continuous deformation by which one can be converted into the other, there must be a surface where the string is cut, shown as a string with open ends (centre), to pass between the two knots (adapted from [136]).

Topological insulators materials have been recently classified among Bi compounds, particularly tetradymite chalcogenides. Bi_2Te_3, Bi_2Se_3 and Sb_2Te_3 have been extensively studied by means of Angle Resolved Photo Emission Spectroscopy (ARPES), revealing the presence of the edge state Dirac cones [37, 205, 192, 86]. More recently evidence of 2D transport channels in Bi compounds devices and in HgTe nano-ribbons have been confirmed by the study of the Shubnikov - de Haas oscillations [152, 185, 195, 174, 6, 83, 175, 164, 58, 166].

2.3 SHUBNIKOV – DE HAAS OSCILLATIONS

If in a quantum Hall state (see Sec. 2.1.3) $E_F \gg \hbar\omega_c$, many ($N > 10$) Landau levels are populated and it is not possible to resolve their

discreteness. Therefore σ_{xx} shows typical oscillations, known as "Shubnikov - de Haas" (SdH) oscillations (see Fig. 23). This is the case for instance of low magnetic field and high doping levels.

The recent introduction of topological insulators required a systematic method to study topological features of Hall devices, including the determination of the Berry phase [152, 185, 6, 195, 83, 166, 58] (see Sect. 2.3.3). Specifically, as discussed in Sec. 2.2, 3D topological insulators are characterized by a linear energy dispersion, thus obeying Dirac's equation.

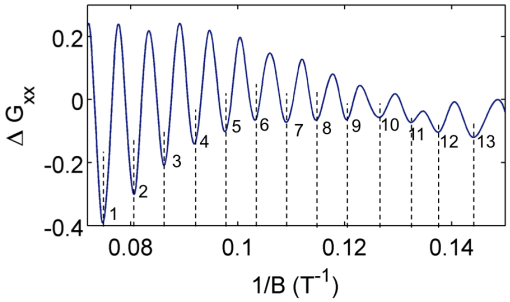

Figure 23: Oscillations of the residual conductance as a function of the reverse of the magnetic field. ΔG_{xx} shows typical, equally spaced oscillations (see Eq. 66). The position of the Landau level are given by the position of the minima and the values of N and $1/B_N$ are extracted (see text for details).

The oscillations are related to the passage of the Fermi energy across the Landau levels, therefore their periodicity is related to the ratio ω_c/E_F. Nominally the frequency is given by the Onsager's quantization condition [160, 8]

$$A_N = \frac{2\pi e}{\hbar c} B \left(N + \frac{1}{2} - \beta \right) \tag{64}$$

which is satisfied when the N^{th} Landau level is crossing the Fermi energy. Here, A_N is the area enclosed by electrons in the k-space with their cyclotron orbits on the Fermi surface. The parameter $\beta = \varphi_B/2\pi$ is determined by the Berry phase [25] (see Sec. 2.3.1, 2.3.3), which is expected to be π in topological insulators (i.e. $\beta = 1/2$) and 0 in topologically trivial materials.

In order to evidence the effect, the background conductance is typically subtracted, and the oscillations of the residual conductance ΔG_{xx} are studied. The position of the Landau levels can therefore be addressed from the position of the minima of the ΔG_{xx}, as shown on in Fig. 23.

2.3.1 SdH in a Dirac Electron Gas

Dirac electrons are characterized by a value of the Berry phase of π [8, 144, 203, 119]. It can be shown that a 2D electron gas with a Dirac energy dispersion in a Magnetic field have Landau levels. However their energies are different with respect to Landau levels in 'normal' (i.e. Schrödinger) 2DEGs (see Fig. 24). Nominally the energies

$$E_N = \sqrt{\hbar\omega_c N} \tag{65}$$

are characterized by

- An aperiodic spacing of Landau levels
- The presence of a Landau level at $E = 0$, which is not present for Schrödinger electrons (see Eq. 42). The position of this level cannot be tuned with the magnetic field.

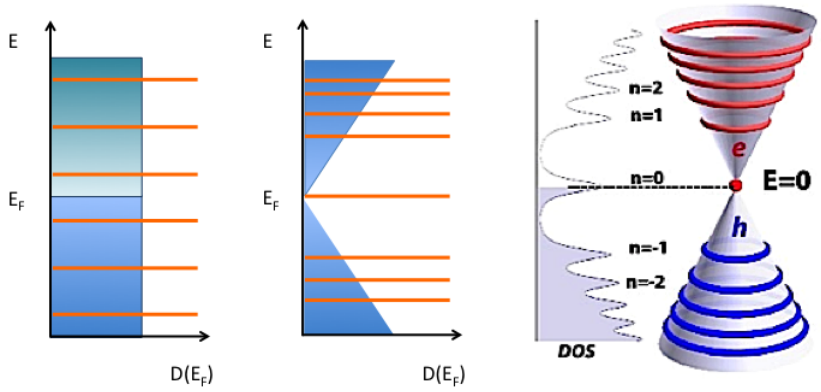

Figure 24: Landau levels in Schrödinger (a) and in Dirac (b) electrons.

From the analysis of the SdH it not possible to see the trace of the aperiodic level spacing, which instead can be verified with STM analysis [208, 38]. However from the value of the Berry phase it is possible to infer whether one has Dirac electrons or Schrödinger electrons. This can be done with the fan diagram.

2.3.2 Fan Diagram

In Fig. 25, the sequence of the values $1/B_N$ of the N^{th} minima of the magneto-conductance oscillations

$$\Delta\sigma_{xx} \simeq \cos\left[2\pi\left(\frac{F}{B} - \frac{1}{2} + \beta\right)\right] \tag{66}$$

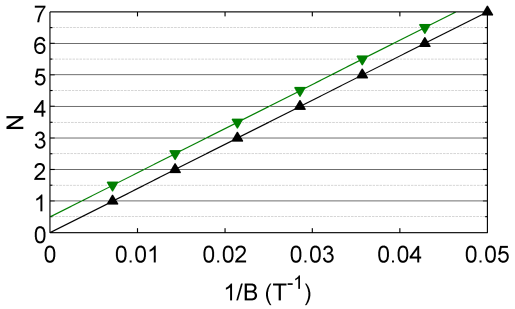

Figure 25: Fan diagram of the $1/B_N$ values of the σ_{xx} minima. The slope of the line is given by the frequency F of the σ_{xx} oscillations (see Eq. 67). The intercept of the line, instead, is connected to the value of the Berry phase. In the case of $\varphi_B = \pi$, the line shows a value of the intercept of $\beta = 1/2$ (downward triangles, in green), while the topologically trivial case ($\varphi_B = 0$) is depicted by upward triangles, in black.

are plotted as a function of the label N.

The minima of $\Delta\sigma_{xx}$ occurs each time that value of the argument

$$2\pi\left(\frac{F}{B} - \frac{1}{2} + \beta\right)$$

equals $\pi(2N-1)$. Therefore the slope of the straight line which connects the value of $1/B_N$ vs N is the frequency F, which is connected to the carrier density

$$F = \frac{\hbar c}{e} n_{2D} \tag{67}$$

The intercept of the line, instead, is connected to the value of the Berry phase [25], and it is a fundamental information on the topology of the system.

2.3.3 Berry Phase

When the linear fit is interpolated to $1/B_N \to 0$, the intercept of the N-axis assumes a value β, which is connected to the the Berry phase. Specifically a value of $\beta = 1/2$, corresponding to a Berry phase of π is expected in the case of Dirac electrons, while a $\beta = 0$ is the typical value of the Berry phase $\varphi_B = 0$ of the Schrödinger electrons [8].

The index N of the Landau levels, as extracted from the oscillations, is defined up to an arbitrary constant. The absolute value of N can be extracted imposing the value $N = 0$ when $1/B_N \to 0$. The presence of Berry phase modifies the boundary condition to be $N = 0 + \beta$ (when $1/B_N \to 0$). Therefore the Berry phase gives a rigid shift to the fan diagram, as shown in Fig. 25. However, this shift cannot be accounted

on the arbitrary attribution of the label N as the displacement is a semi-integer value of N.

A spurious 1/2 shift, instead [193, 8], can appear if the fan diagram is constructed using the oscillations of ρ_{xx}. In this case an uncertainty in the assignment of the indexes is given, namely whether to assign an integer index to a minimum or to a maximum of ρ_{xx}. In fact, if a wrong choice is made, a spurious $\beta = 1/2$ intercept can be observed for Schrödinger electrons.

When the condition $\sigma_{xx} \ll \sigma_{xy}$ is satisfied (which is usually the case with low-carrier-density semiconductors), $\rho_{xx} \simeq \sigma_{xx}/\sigma_{xx}^2$ and the minima in ρ_{xx} coincide with those in σ_{xx}. This is the reason why the fan diagram constructed from the minima of ρ_{xx} data can give the correct phase factor in graphene [142, 120, 207]. However, in the case of TIs, due to the presence of the bulk transport channel, often the condition $\sigma_{xx} \ll \sigma_{xy}$ does not strictly hold [8, 70]. In the extreme case, when $\sigma_{xy} \ll \sigma_{xx}$ (which is usually the case in metals), $\rho_{xx} = \sigma_{xx}^{-1}$, and the minima of ρ_{xx} now coincide with the maxima in σ_{xx}. In this limit, as mentioned a recent paper [193], one should refer to resistance maxima. However, this ambiguity is avoided by directly referring to the minima of the ΔG_{xx} [194].

2.3.4 SdH in 3D Systems

Shubnikov - de Haas oscillations are not an exclusive feature of 2D system, but they can also be detected in 3D systems, under some conditions, due to the formation of Landau bands [166]. In 3D it is possible to observe oscillations for any direction of the magnetic field. Therefore a support to the 2D nature of SdH oscillations can be provided by a study of the oscillations as a function of the angle θ between the magnetic field and the surface of the sample [152, 58].

The projection of the 3D Fermi surface on the plane orthogonal to the magnetic field, cuts a 2D projection in the k-space. The area of this 2D projection determines the frequency of the SdH oscillations, following the Onsager's relation (Eq. 64). If the system has an isotropic Fermi surface, the frequency of the oscillations F should be independent from the angle θ, while in anisotropic systems F depends on the value of the angle θ, following the different sections of Fermi surface along different orientations [167, 84, 80].

This effect is traditionally [8] studied by plotting the SdH oscillations as a function of the normal component $1/B_N$

$$2\pi\left(\frac{F}{B_N} - \frac{1}{2} + \beta\right)$$

If the system is a 2DEG, the position of the minima should not vary with the angle θ.

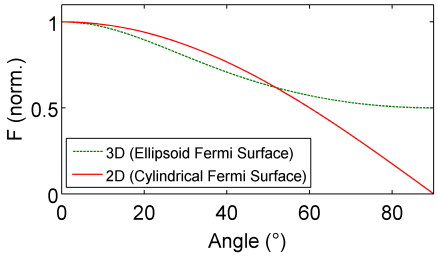

Figure 26: Frequency of the oscillation as a function of the angle θ for different shapes of the Fermi surface. The green dashed line is the case of an ellipsoid Fermi surface (2 axis of the ellipsoid are equal, and one is a factor of two bigger), while the red line describes the case of a 2D transport, given by a cylindrical Fermi surface.

Equivalently [175], it is possible to extract if the transport is a 2D or an anisotropic 3D by studying the behavior of F vs θ. Specifically in the case of a 2D transport, F changes as $1/\cos\theta$. If instead the transport is an anisotropic 3D, the frequency of the oscillations still changes as a function of the angle, but the dependence does not follow the cosine dependence behavior (see Fig. 26).

2.4 TOPOLOGICAL SUPERCONDUCTORS

When superconductivity is induced in a topological insulator, a new state of matter is created. This is called a "Topological Superconductor". In this case a spinless superconducting state with a p wave order parameter can be created [18, 1]. The presence of Majorana bound states at the interface between a trivial superconductor and a topological superconductor is predicted [18, 1, 96, 149].

2.4.1 Majorana Bound States

Majorana fermions were predicted in 1937 by Ettore Majorana [121], as neutral solution of the Dirac equation of relativistic quantum field theory. Majorana fermions are spin 1/2 massless fermion, which are their own antiparticles, therefore they were proposed as candidates to describe neutrinos ("there is now no need to assume the existence of antineutrons or antineutrinos", cit. E. Majorana).

The simplest model accounting for Majorana fermions as boundary excitations is the Kitaev model [96, 95]. This model describes a one

dimensional p-wave spinless superconductor. The solution of the model predicts the formation of Majorana bound states at the end of the chain (see Fig., 27a), under certain constraints on the hamiltonian parameters. In fact, let's consider a chain on N Dirac fermion. The hamiltonian of the system:

$$H - \mu N = \sum_i t\left(c_i^\dagger c_{i+1} + c_{i+1}^\dagger c_i\right) - \mu c_i^\dagger c_i + \Delta\left(c_i c_{i+1} + c_{i+1}^\dagger c_i^\dagger\right) \quad (68)$$

where μ and t represents on-site interactions and the interactions with the nearest neighbors fermions of the chain respectively. c_i and $c_i^\dagger$ are the electron annihilation and creation operators, respectively. The system can be recast in terms of Majorana fermions. In the limiting case of $\mu = 0$ and $2t > 0$, the ground state of the system presents unpaired Majorana fermions the the edges of the chain.

It can be shown that the an s wave quasi-1D superconductor (i.e. a wire) in presence of spin-orbit coupling and a magnetic field along the wire can be mapped onto a spinless quasi 1D p wave superconductor (Kitaev model) in the low energy limit [96, 149, 61]. This is why recently, InAs and InSb nanowires in proximity with s wave superconductors are expected to present the physics of unpaired Majorana fermions. However, to the date, the most relevant experiment by Mourik et al. [139] is still strongly debated.

In two dimensions the presence of Majorana fermions embedded in the core of a vortex is predicted [18]. In the p wave, the superconductor opens an excitation gap, which can be closed locally by a magnetic field (see Fig. 27b). As the Majorana fermions have to stick at zero energy, a possible experimental route is to look for zero energy bias anomalies in tunneling spectroscopy [139, 102]. However, no clear signature have been measured up to now [140, 60].

The presence of Majorana bound states in Josephson junctions with topological barrier, is expected to modify the CPR, thus giving a 4π periodic relation [65, 18, 1, 149, 161, 191, 103, 184, 183]. However, the condition to experimentally observe Majorana bound states are rather stringent, as pointed out in recent papers [161, 150, 183, 118]. The reason of this difficulty has to be sought in the competing mechanisms of different transport channels. Specifically if a trivial superconducting transport is created within the junction, there is a competing mechanism between a 2π and a 4π periodic relation. In this case the experiments also give evidence of the lower periodicity [153, 183].

Moreover even if 4π periodicity was measured, this would not be an unambiguous proof of the existence of Majorana fermions, as possible Landau-Zener transitions could result in similar evidences.

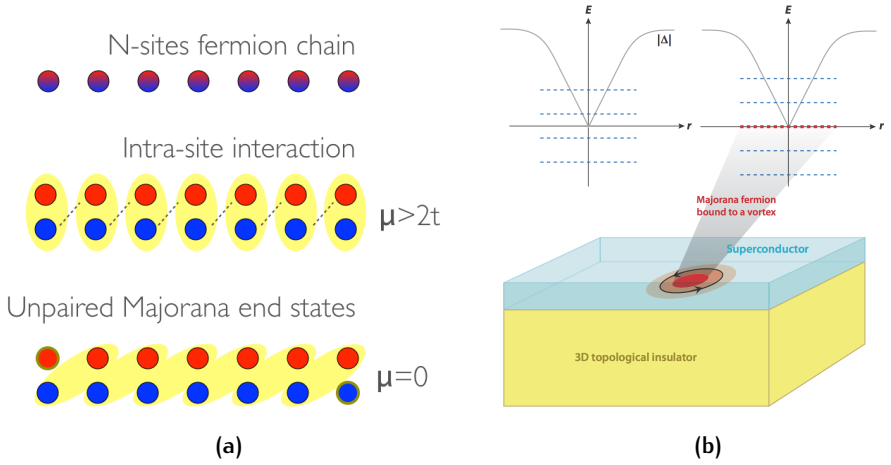

Figure 27: (a) Sketch of a 1D spinless p-wave superconductor. As the intra-site interaction t is increased the coupling between the nearest neighbors is increased, yielding, in the limiting case of $\mu = 0$ and $t > 0$ to the creation of a couple of unpaired Majorana fermions at the end of the chain (courtesy of P. Lucignano). (b) Schematic representation of a Majorana fermion embedded to an Abrikosov vortex core. The magnetic field creates sub-gap states $E_n = n\delta$, which does not include $E_n = 0$. The presence of a Majorana fermion shifts the energy of the levels of an amount $\alpha = 1/2$, thus creating an $E_n = 0$ energy state (adapted from [18]).

3 MEASUREMENT SETUP AND DEVICE FABRICATION

In this Chapter I will present the equipment used to fabricate the devices (Sec. 3.1) and the experimental setup used for low noise measurements in cryogenic environments and high magnetic fields (Sec. 3.2). A description of the device realized in this work is also included (Sec. 3.3).

3.1 NANO-LITHOGRAPHY TECHNIQUES

The fabrication process is based on the e-beam lithography technique, which allows to define the geometry of the devices with an extremely high resolution ($10 - 100$ nm).

3.1.1 e-beam lithography

The e-beam lithography has become the universal standard for nano-fabrication techniques, thanks to its versatility and high performances. In fact it is relatively easy to achieve sub-micron patterning without the use of a hard mask, as for instance in photolithography technique. In the e-beam lithography, the design is be created on a CAD file, and then converted to a format which is interpreted by the software of the machine and impressed on the device through a focussed electron beam. This gives the high versatility of this technique, as the design can be changed and adjusted as required.

The e-beam machine used to fabricate the Bi_2Se_3 and Bi_2Te_3 devices presented on this work is the Jeol-JBX 9300 FS. This system has a gaussian beam of 4 nm of diameter, emitted by a ZrO/W thermal field source.

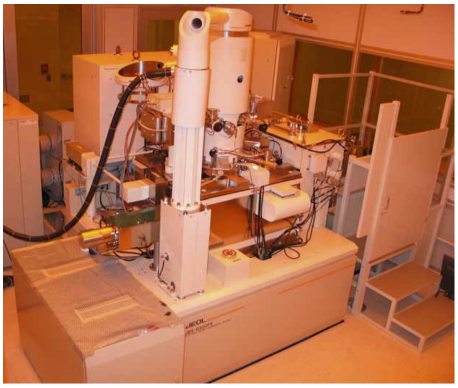

Figure 28: The Jeol JBX 9300 FS system.

The system allows for exposition at 50 kV or at 100 kV at beam currents ranging between 50 pA and 100 nA. The system is also equipped with an interferometric stage allowing for a positioning with a precision of 0.62 nm.

3.1.2 e-beam resist, development and Lift-Off

In order to impress the design on the sample a thin film ($10 - 100$ nm) of a sensitive polymer (e-beam resist) is spun on the sample (in this work ZEP-520A 1:2 Anisole) and baked at 130 °C. The exposition of the resist to e-beam changes the chemical composition of the exposed part. Therefore it can be removed upon immersion of the device in a suitable solution, called "developer" (in this work Hexyl Acetate). The ZEP is a positive e-beam resist, this means that the exposed parts are removed in the development procedure. A copolymer (MMA EL8) is spun on the sample prior to the ZEP. Its use is required for the lift-off procedure, described below. This procedure is used to transfer the design from the e-beam resist to the final device.

In the lift-off, a thin metallic film is evaporated on the sample (in this work through an e-beam evaporation technique, performed in a Lesker PVD 225 system). The unwanted parts of the metal thin films can be therefore removed in a warm acetone bath (this last step is the so called called lift-off).

The resolution of the lithography is typically limited by electron diffraction phenomena which take place in the e-beam resist, therefore a higher resolution is achieved with thinner resist layer, on the other hand the thickness should be sufficient to permit the lift-off. In order to have a good lift-off, the thickness of the resist has to be significantly (i.e. 30%) higher than the thickness of the metal film. In our samples a total thickness of 190 nm was achieved (ZEP: 60 nm, EL8: $\simeq$ 130 nm). The use

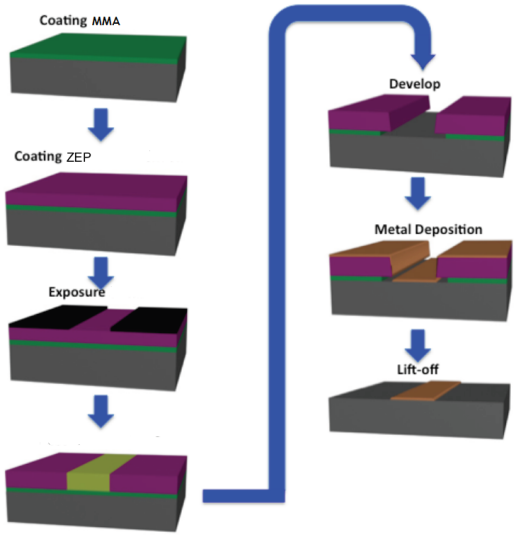

Figure 29: Lift off procedure: (on the left) lift off layer deposition, resist layer deposition, exposure; (on the right) develop (undercuts produces a gap in the deposited metal), metal deposition, and lift off.

of a copolymer is used to create undercuts after the development (MMA EL8 is developed in MIBK:IPA 1:1). As shown in Fig. 29, the undercuts are required to create a gap between the part of the metallic film deposited on the top of the resist layer and the part directly deposited on the sample.

3.1.3 Description of the e-beam Machine

Column

The very heart of the e-beam machine is the electro-optical equipment used to create the focussed electron beam. This is called the "column". The column is composed of several lenses, made of magnetic multipoles, used to focus the beam (see Fig. 30). The beam line also includes an astigmatism correction electrode, and two pairs of deflectors (main deflectors and subsidiary deflectors), which are used to move the beam on a writing field in the x and y direction. The writing field size of the system is 500 µm x 500 µm.

Stage

To achieve design are bigger than 500 µm x 500 µm, the chip is divided in fields, and a movement of the stage is used to move the sample below the column. When the exposure of a writing field is completed, the stage

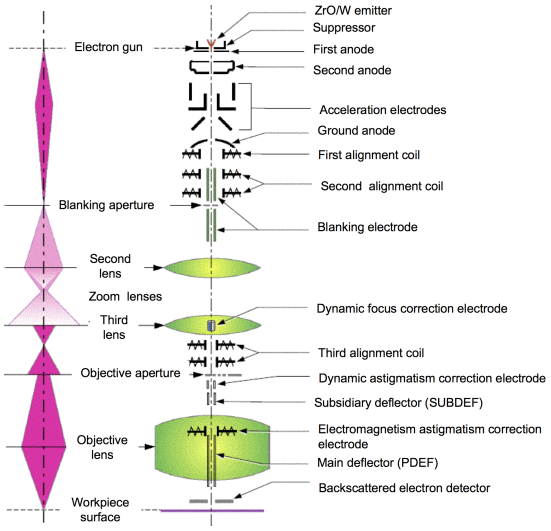

Figure 30: A sketch of the electro-optical system of the Jeol JBX. The main components are labeled.

moves to the next writing field as shown in Fig. 31a. At the edges of the writing field the exposition is interrupted, and continued after the stage movement, therefore the alignment is a crucial step. It the system used in this work, this is achieved through a couple of two arms interferometer (see Fig. 31b), allowing to a precision of 0.62 nm in the positioning of the stage. The edges of the writing field usually have a lower resolution than the center. This is due to effects of distortions of the deflectors which are more severe at higher deflection angles. For this reason, the most demanding part of the design (in terms of resolution) should always be positioned as close as possible to the center of the writing field.

System Calibration

The fundamental issue to increase the performances of the system is an accurate calibration of the optics, including:

- the adjustment of the focus
- a correction of the beam astigmatism
- a calibration of the main and subsidiary deflectors
- a correction of the field distortion
- the alignment of the sample

This procedure is performed by using two detectors, allowing the detection of both absorbed electrons (AE) and (BE) backscattered electrons (see Fig. 32a, 32b). These detectors can be also used to perform an imaging of parts on the sample (SEM), if required. The calibration is initialized by eye (optimizing the SEM image), and then implemented using an automatic procedure, which is repeated right before each exposure.

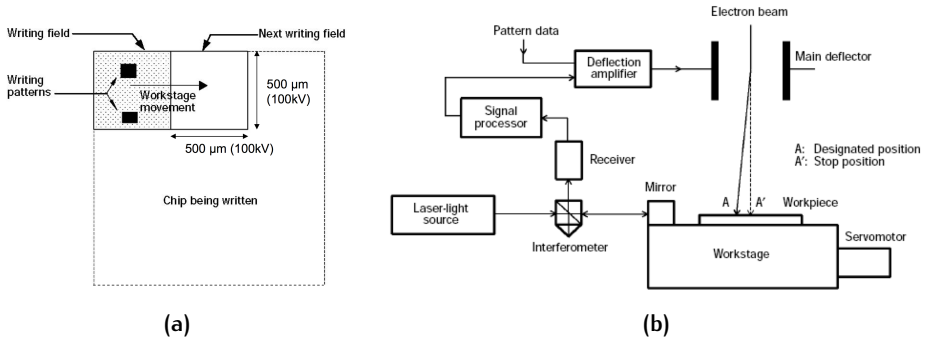

Figure 31: (a) Sketch of the movement of the stage from a writing field to the new writing field. (b) Scheme of the stage of the machine, including the interferometer system for the stage positioning.

The system is conceived to automatically recognize the position of a cross marker, using the BE sensor. Upon a scan on the arms of the cross it is possible to extrapolate the centroid of the marker, through a procedure of numerical differentiation and autocorrelation of the BE signal.

The focus and astigmatism of the beam is optimized through multiple scans on the edge of a mark (see Fig. 32a). The parameters are optimized to get the sharpest profile. The focus is optimized on a reference surface, whose height is measured to high precision using a couple of laser-beams and two four quadrant photodiodes (see Fig. 32c). Then the height of the sample is measured, and the focus is continuously optimized during the exposure, through the dynamic focus correction electrode shown in Fig. 30.

To calibrate the deflector of the beam a cross markers is used. The marker is moved to different position of the writing field and detected with the beam. The absolute value of the distance is separately measured with the interferometer, as shown in Fig. 33. Therefore the deflector positioning is calibrated with high precision.

The field distortion is corrected using an array of equally spaced cross markers. The deflector and sub-deflector voltage deviates from the linear behavior at higher angles, generating the distortions at the edges of the field described above. The distortion corresponds to an apparent dislocation of the markers at the edge of the writing field. However the

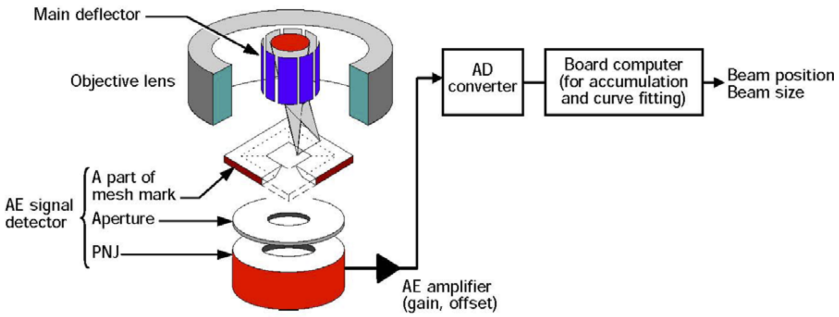

(a)

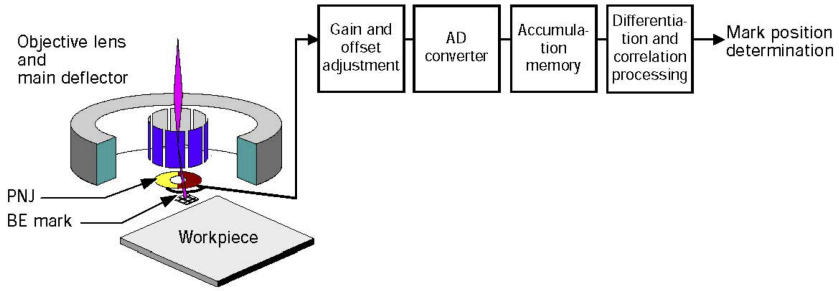

(b)

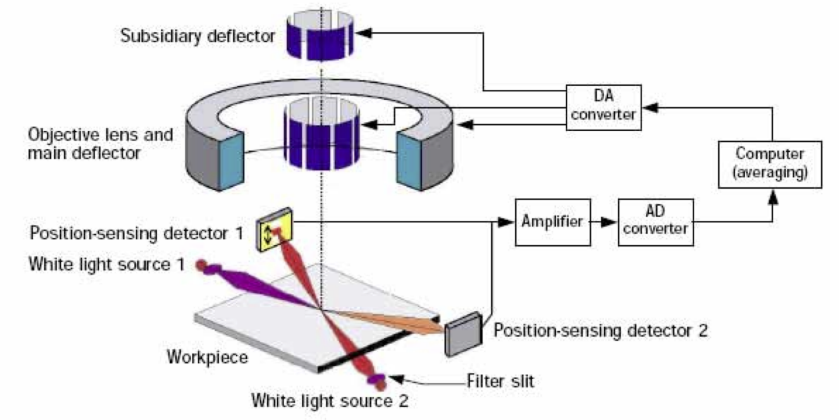

(c)

Figure 32: Scheme of the detectors for adsorbed electrons (AE) - panel (a) and backscattered electrons (BE) - panel (b). (c) Scheme of the system for height measurements, the system is based on two crossed laser. The position of the reflected light is measured with a four quadrant photodiode. The optical lever enhances the precision of the measurement.

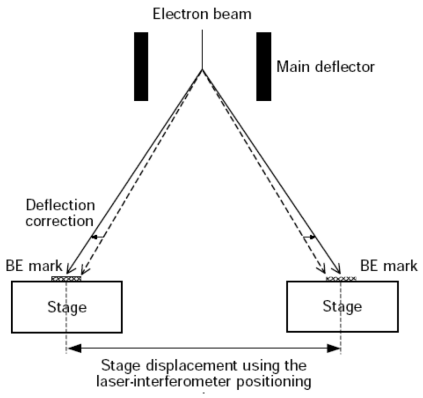

Figure 33: Sketch of the calibration procedure of the deflectors.

distortions can be partially compensated by correcting the deflection voltage to minimize the apparent dislocations of the markers.

The last crucial step of the calibration is the alignment of the sample. In this step the system searches two cross marks on the sample, using the correlation function of the BE sensor, as described above. These marks are usually defined in a preliminary lithography step. The relative position of the two marks with respect to the design is specified on the CAD file. In this way, the position of the sample is aligned with the design. In our samples, for instance, this is required to align the Al electrodes to the flake of TI, as described in Sec. 3.3.1 below.

3.2 LOW NOISE MEASUREMENTS AT CRYOGENIC TEMPERATURES

In this paragraph we will describe the equipment used to perform transport measurements. The measurements have been performed in a cryogenic environment, and includes the use of high magnetic field, generated by superconducting coils included in the system. State of art electronic equipment was used to perform low noise measurement, including high gain amplifiers, with high signal to noise ratio, and advanced filtering stages, both at room temperature and at cryogenic temperatures.

3.2.1 High Magnetic Field Measurements

The preliminary characterization of Bi_2Se_3 samples at high magnetic field, described in Sec. 4.1 was performed in a Quantum Design PPMS

system. This system is equipped with a NbTi magnet to perform measurements in magnetic field up to 14 T, at temperatures down to 2 K. The system is optimized for measurements of R(T) and R(B) in a four point configuration. The device is biased with a d.c. current of 1 μA, and the corresponding voltage is measured. We performed measurements in a Hall configuration, thus measuring V_{xx} and V_H (see Fig. 34) as a function of the magnetic field. It is possible to rotate the sample with respect to the magnetic field, using a motor. The position of the sample can be changed while keeping the system cold.

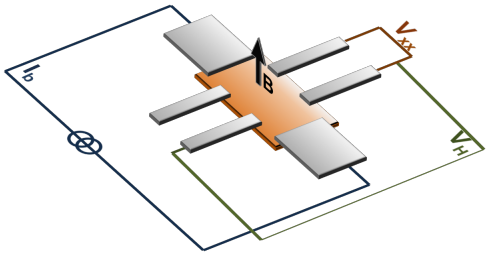

Figure 34: Sketch of a Hall bar in a perpendicular magnetic field. The device is biased with a current I_b. The Hall voltage V_H and the longitudinal voltage V_{xx} are measured between the voltage probe as shown in figure.

3.2.2 Evaporation Refrigerator

Most of the low noise transport characterization included in this work are performed using an evaporative refrigerator (Oxford Instruments Heliox VS system). This system allows to reach a base temperature of roughly 250 mK, basing on the principle of the evaporative cooling of ^{3}He. This is a very robust system, that allows a fast cool down with limited ^{4}He consumption.

The system is immersed in a thermal bath of ^{4}He (at the temperature of 4.2 K), from which the cryostat is thermally decoupled through a vacuum cell (IVC).

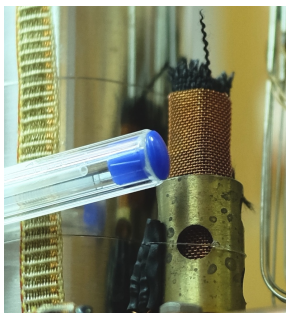

Figure 35: A sorb cryo-pump. The scale is signaled by the pen.

The system uses a 1 K pot to cool down to the temperature below 2.2 K, the liquefaction temperature of ^{3}He, down to a approximately 1.5 K. The ^{3}He, which is contained in a closed tank, is therefore condensed in, and later pumped in a 'single shot' operation with a sorption pump, allowing a stability at base temperature of approximately 7 h. The sorption pump is a molecular pump that is based on the adsorption mechanism (see Fig. 35). It consists of a large amount of zeolite, enclosed in a small cylinder inside the cryostat. When zeolites are at a temperatures lower than 30 K, the vapor of ^{3}He are adsorbed. The pump can be activated and switched off by a heating system, as needed.

This system allowed measurements with high thermal stability at temperatures between 250 mK and 80 K. The system is also equipped with a NbTi superconducting coil to apply an external magnetic field to the system, up to 300 mK, and with a microwave line, allowing to shine a RF radiation on the sample via a linear antenna.

3.2.3 Dilution Refrigerator

A characterization of the samples down to 20 mK was performed using dilution refrigerators. Specifically measurements are mainly performed a Oxford Kelvinox MX dilution refrigerator. Measurements presented in Sec. 6.5, instead have been measured in a cryogen free Oxford Triton 200 refrigerator.

The Oxford Kelvinox MX was equipped with a NbTi coil to apply an external magnetic field up to 50 mT. The Oxford Triton 200 instead was equipped with a 12 T NbTi magnet for high field measurements. Lower field could be achieved with a 10 mT Cu Humboldt coil, with the axis orthogonal to the main magnet. Moreover the system was also equipped with a microwave line, similarly to the Heliox system described above.

Generally speaking the working principle of the two systems is rather similar: it is based on the principle of cooling by diluting a ^{3}He - ^{4}He mixture. As shown in Fig. 36 the mixture, below 867 mK, undergoes a phase separation. Therefore the dilution induces a cooling process, following the phase separation curve. This process is achieved in the dilution unit.

Dilution Unit

The hearth of the dilution unit is the mixing chamber: a pot, connected with two pipes, allowing to selectively address the the two phases of the mixture. In fact when the two phases separates, the ^{4}He rich phase, which is heavier, goes below the ^{3}He rich phase. The pipe connected to

the bottom (called "Still line") is connected to the ^{4}He rich phase. It is used to extract the ^{3}He, through a mechanical pump. The ^{3}He is then brought back through the the pipe (called "condenser line") connected to top of the pot (see Fig. 36), thus creating a closed loop.

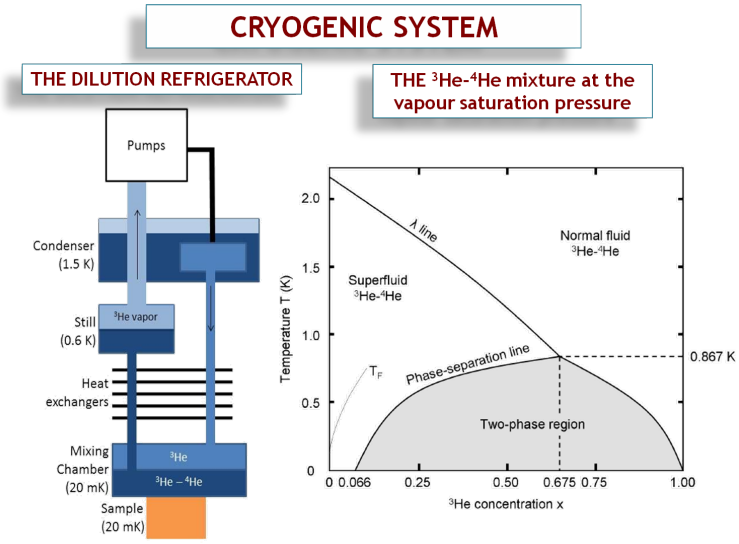

Figure 36: Scheme of a dilution unit, showing the main components, and phase diagram of the ^{3}He - ^{4}He mixture.

Diluting the ^{4}He phase is possible by applying some heat, which prevailingly causes the evaporation of the ^{3}He. This 'distillation' procedure is normally performed in a separate pot, called "Still". The ^{3}He evaporated in the Still is evacuated by a mechanical pump. The dilution of the mixture in the mixing chamber, instead, is driven by the osmotic pressure created between the mixing chamber and the Still.

Finally the ^{3}He recollected by the mechanical pump is re-condensed and added to the ^{3}He rich phase through the condenser line. The system thus allows for continuous operations.

The crucial part of the continuous circulation system is the pre-cooling of the warm ^{3}He added to the mixing chamber. The ^{3}He is first pre-cooled in several steps, using the various stages of the cryostat to progressively cool down the gas, however the most demanding part in the thermalization at the lowest temperatures. This is achieved trough a combination of a continuous heat exchanger and a cold plate exchanger (see Fig. 37), optimized to enhances the heat transfer between the still and the condenser line.

The dilution units is the most complex part of a dilution refrigerator, however it is the last of several stages of cooling of the cryostat. At this regards different solutions can be used.

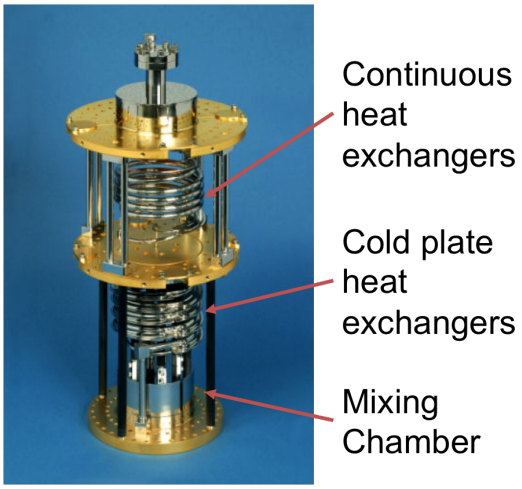

Figure 37: Picture of dilution unit. The heat exchangers and the mixing chambers are pointed out.

Wet and Dry Fridges

Most of dilution refrigerators uses a ^{4}He bath and a 1 K pot to reach the temperatures required to condense the mixture. The 1 K pot is also used to pre-cool the mixture in the circulation procedure. In this case the system is similar to an evaporation refrigerators described is Sec. 3.2.2. More recently the use of cryogen-free refrigerators is becoming more and more widespread.

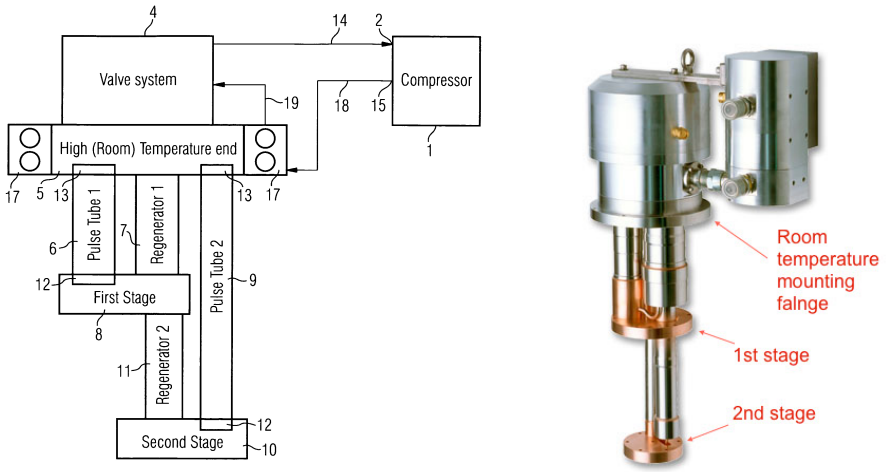

Figure 38: (a) Scheme of a pulse tube and (b) picture of the system.

A cryogen-free cryostat is based on a pulse tube to pre-cool the system allowing to cool down to 20 mK without the use of cryogenics. The pulse-

tube is based on a non-equilibrium thermodynamic cycle of ^{3}He. The tube is alternatively connected to a reservoir with high (3 bar) and low (1 bar) pressure, thus creating an enthalpy flux flowing from the middle part of the tube (see Fig. 38) to its extremities. Therefore the middle of the tube cools down. However, a detailed description of the working scheme goes beyond the purposes of this work. With a double stage of pulse tube coolers it is possible to reach temperatures of the order of 5 K.

In order reach the temperatures needed to condense the mixture, a further step is required. This is usually achieved with a Joule Thomson stage. This requires the use of a compressor, adjoint to the condenser line. At this stage the ^{3}He - ^{4}He mixture is compressed up to 2 bar, thermalized at 5 K and finally adiabatically expanded. In this way the mixture cools down and condenses. The following stages of the cryostat follows the classical sequence of the dilution unit.

3.2.4 Low noise measurements: IV characteristics and switching current distributions

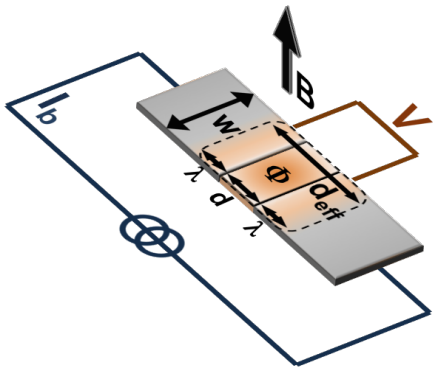

Figure 39: Sketch of a Josephson junction, the shaded area corresponds to the effective area of the junction.

All the measurements presented in this work have been realized in a magnetically shielded environment. The shielding was provided by a system of superconducting and cryoperm screens.

The measurements were performed in a pseudo four point contact configuration. A current bias is applied to the junction, using a waveform generator in series with a high (1 MΩ) resistor. The voltage across the junction is measured with two voltage probe (see Fig. 39) and amplified by a voltage amplifier with a high gain (100 - 10 000). The IV curves are therefore measured. To increase the sensitivity the actual IV curve is mediated on many (500) sweeps.

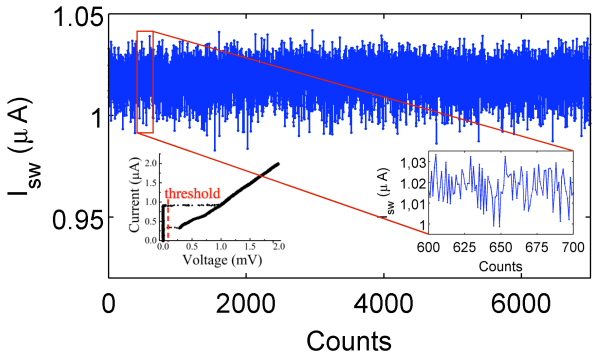

Figure 40: Repeated measurements of the switching current. A zoomed area of the graph is also shown. A threshold detector is used to detect the switching to the resistive state. The threshold is set to be just above the voltage noise in the zero voltage state, and far below the switching voltage, as shown in the inset

To measure switching current distributions (SCD), a current ramp is used to bias the junction. when the bias current approaches I_C, the voltage shows a sudden jump to a finite value. The switching event is detected through a threshold detector, and the value of the switching current is extrapolated. The switching current distribution is therefore achieved by collecting switching currents over many (10^4) repeated ramps (see Fig. 40).

The system is equipped for low noise quasi d.c. measurements, including some stages of cryo-filters. Specifically, the filtering is guaranteed by a room temperature electromagnetic interference filter stage followed by low pass RC filters with a cutoff frequency of $1 - 10$ MHz anchored at 1.5 K, and by a combination of copper powder and twisted pair filters (see Fig. 41) thermally anchored at the cold finger (mixing chamber - ^{3}He pot).

3.3 DEVICES

In this paragraph the devices realized within this work are presented, with a special focus to the fabrication of Al/Bi_2Se_3/Al and AlBi_2Te_3/Al coplanar devices.

3.3.1 S/TI/S coplanar structures

We have fabricated coplanar Josephson junctions on the surface of the Bi_2Se_3 and Bi_2Te_3 flakes. The flakes were exfoliated from Bi_2Se_3 single crystals and from Bi_2Te_3 thin films, epitaxially grown through molecular

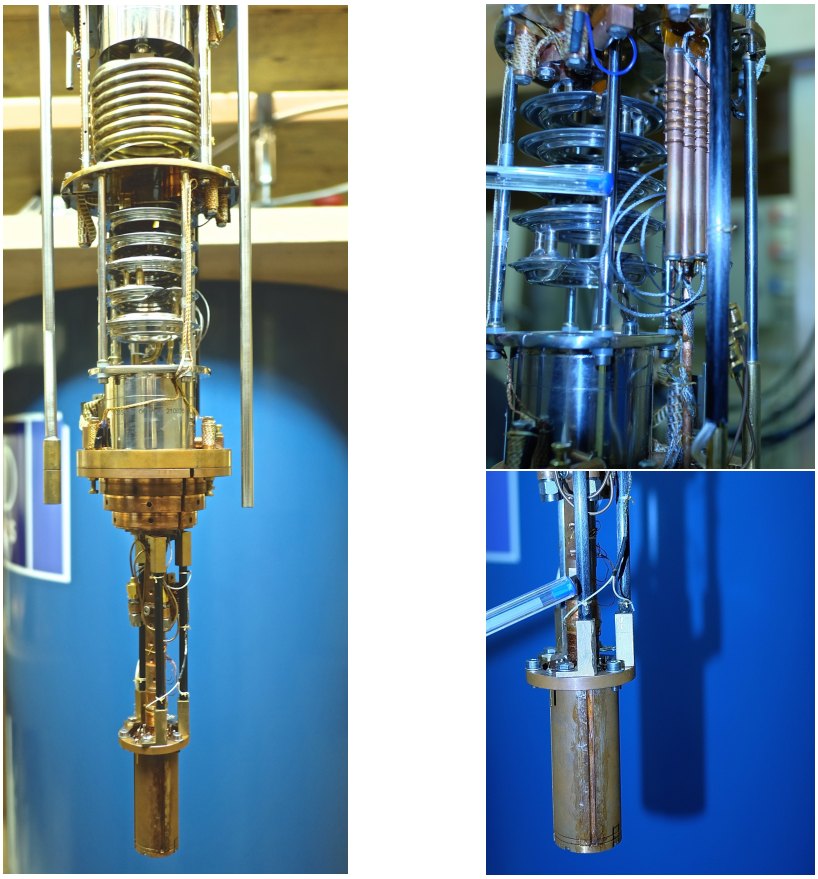

Figure 41: (left) Picture of the Kelvinox MX system used in this work (right) A detail of the two Cu powder filtering stages working at 50 mK (top picture) and at 20 mK (bottom picture). The pen sets the scale of the picture.

beam epitaxy (MBE), and transferred on a Si/SiO_x substrate substrate, to pattern Josephson and Hall devices.

Bi_2Te_3 Thin Film Deposition

Here we will describe the MBE technique, used to grow thin Bi_2Te_3 films. Thin film growth using MBE allows more precise control over the composition and thickness [67, 163]. The thin films are grown epitaxially with their c axis perpendicular to the surface, as verified through XRD analysis. Specifically the (0 0 1) planes were detected using a symmetric $\omega - 2\theta$ X-ray diffraction (XRD) scans.

A phase transition occurs from Bi_2Te_3 to Bi_4Te_3 during the MBE growth of bismuth telluride thin films when low tellurium flux is used [67], and we selected samples with the ideal Bi_2Te_3 stoichiometric composition, which are expected to show the TI features, to perform the transport measurements presented in Sec. **??**. The stoichiometric

composition of the film was confirmed via a combination of XRD analysis and AFM, as shown in Fig. 42

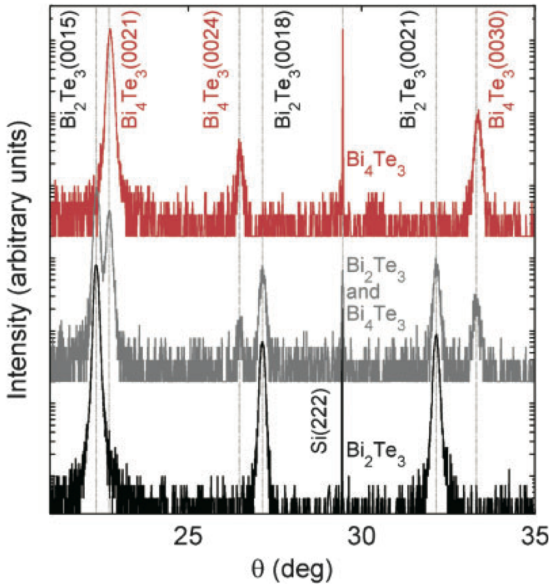

Figure 42: XRD scans showing diffraction peaks for samples various samples containing Bi_4Te_3, both Bi_2Te_3 and Bi_4Te_3, and only Bi_2Te_3, respectively. The values in the parentheses next to each peak indicate the Miller indices of the crystal planes.

The samples were grown on Si (1 1 1) and GaAs (1 1 1) substrates using a Riber Compact 21 MBE system. Before the growth, the Si substrates were etched by a mixed chemical solution of HF and NH_2F to remove the surface oxide, and then quickly transferred to the degas chamber of the MBE and heated to 600 °C until the pressure in the chamber dropped below $1 \cdot 10^{-8}$ Torr. The GaAs substrates were cleaned thermally in the growth chamber at 650 °C. The growth took place under ultra-high vacuum in the range of 10^{-11} Torr. Prior to the epitaxy, a one minute Te soaking on the substrate was implemented to passivate the surface dangling bonds. Then both Bi and Te were simultaneously open to grow the Bi_2Te_3thin films. The growth temperature was varied between 140 °C and 200 °C. A Philips X Pert Materials Research Diffractometer was used to perform the $\omega - 2\theta$ scans to extract the c axis length and a Bruker Dimension 3100 SPM was used for the atomic force microscopy (AFM) scans. The electrical measurements were performed using a Physical Properties Measurement System by Quantum Design at 5 K and up to 14 T.

Bi_2Se_3 Crystal Growth

Single crystals of Bi_2Se_3 are realized through by melt-growth method by reacting pressed pellets of mixed powder of Bi and Se in a evacuated quartz tube. Bi_2Se_3 crystals are characterized by a rhombohedral crystal structure [192] with stacks of weakly linked quintuple layers [204]. Therefore flakes of material can be collected through micro-mechanical exfoliation, and transferred on a Si/SiO_x substrate.

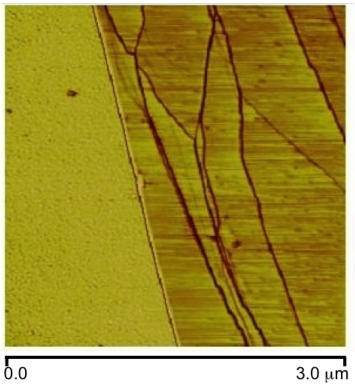

Figure 43: (a) AFM of the surface of a Bi_2Se_3 flake. The presence of the quintuple layers is evidenced by the presence of the steps, signifying an exfoliation along the c axis of the crystal. The steps, with typical separation of $5-10$ nm can be observed.

In Fig. 43 we show a typical Atomic Force Microscopy (AFM) image of an exfoliated Bi_2Se_3 flake. In the picture the surface topography of the sample shows a characteristic stairway like feature. Steps with a typical height of $5-10$ nm are clearly visible from the analysis of a line-scan (Fig. 44a), extracted from the AFM image. The surface is very smooth between the steps, with a roughness below 1 nm (see Fig. 44b), thus we obtain flat surfaces by the exfoliation through the quintuple layer. However steps are created by the mechanical stress accumulated during the wrench required for the exfoliation procedure. In order to increase the smoothness of the surface and to reduce the thickness of the flake, a procedure of multiple exfoliation was performed. The surface shows no steps on a scale of a few microns, which is required to fabricate our devices (see Fig. 34, 39). The final thickness of the flake is typically between 30 and 100 nm.

Nano-fabrication Details

We have fabricated coplanar Josephson junctions on the surface of the Bi_2Se_3 flakes, with a separation of 400 nm between the Al electrodes. The

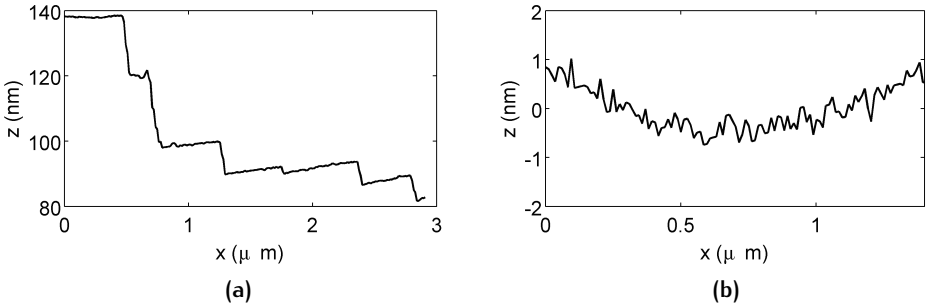

Figure 44: (a) Line-scan extracted from the AFM shown in Fig. 43. The steps, with typical separation of $5 - 10$ nm can be observed. (b). The panel (c) shows the surface of one of the steps. The roughness is below 1 nm, underlining the presence of an atomically flat layer on a scale of at least 1.5 μm. The bending of the line is a spurious effect of the background subtraction.

flakes were randomly deposited on the Si/SiO_x substrate, where a set of Cr/Au markers were previously patterned through a lift-off combined with electron beam lithography. The markers are required to align the electrodes to the position of the flake.

The Al electrodes geometry was then defined through electron beam lithography. The aluminum was deposited by e-beam evaporation in a 10^{-7} mbar environment. The electrodes were then achieved using a lift off procedure.

To increase the adhesion of the aluminum on the Bi_2Se_3 flake, and improve the interface transparency, a short (10 s) Ar^+ ion etching was performed to clean the flake surface. For the same reason a thin buffer layer was deposited in situ before the Al deposition. The buffer layer improves the contact between the Al film and the surface of the Bi_2Se_3 flake and reduces the contact resistance. For instance, a sample (not shown here) was fabricated with no buffer layer and no charge transport through the junction could be detected (its room temperature resistance was too high to be measured).

We have tried 3 different recipes, which differ in the treatment of the interface prior to the electrodes evaporation, and in the material used as a buffer layer. Different treatments lead to different typical characteristics of the devices, and in this manuscript we present three sample junctions with identical distance between the electrodes and comparable cross sections, one representative for each type. The width and the thickness of the junction are defined by the flake geometry and they cannot be fully controlled. However, devices with comparable cross section have been selected. Specifically we present 2 junctions with a Ti interface (junctions 1 and 2). In junction 1 the vacuum was broken between the Ar^+ etching and the Ti/Al deposition, while in junction 2

JJ	size (see Fig. 39) (W (μm) · t (nm) · L (nm))	Buffer layer	Etching
1	2 · 70 · 400	Ti (5 nm)	Ar^+ 10 s
2	2 · 100 · 400	Ti (5 nm)	Ar^+ 30 s (in situ)
3	1.5 · 80 · 400	Pt (3 nm)	Ar^+ 10 s

Table 1: Fabrication parameters of junctions 1,2,3.

the etching was made in situ. We finally present a junction with a Pt buffer layer (junction 3). Further details are listed in Table 1.

Transport Measurements

In figure 45 we report the current voltage characteristics of the three measured devices at the temperature of 280 mK, representative of the different behaviors. The IV curves for junctions 2 and 3 show an ideal over-damped RSJ behavior [14], typical of junctions with a low capacitance barrier. The measured parameters for the three devices are summarized in Table 3. To have a fully comparable dataset, we refer to quantities which are fully independent of the cross section of the junctions (i.e. critical current density J_C, specific resistance $R_N A$ and characteristic voltage $I_C R_N$).

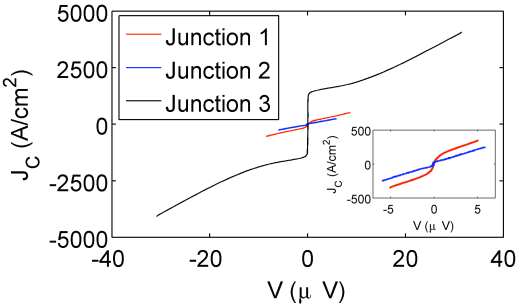

Figure 45: IV measurements of junctions 1, 2 and 3. The inset shows a magnification of the area at low voltages and current, evidencing the difference between junction 1 and 2. In fact while junction 2 shows a clear super-current branch, only a nonlinearity can be observed in junction 1

From Table 2 a clear trend towards better coupling between the electrodes and higher transparency interfaces can be seen from junction 1 to junction 3. This emerges as an increase of the critical current density (Junction 1 did not show a clear dissipation-less current, but only a non-linearity at low voltage), and a consequent increase of the characteristic voltage of the junction (given by the $I_C R_N$ product). The

specific resistance $R_N A$ (where A is the cross section of the junction), correspondingly, shows a slight decrease. The induced superconducting gap and the total effective transparency of the junctions are the most relevant parameters in hybrid superconducting devices [106, 73, 30]. They are strictly connected to the interface quality and to the buffer layer.

Here we have focused on junctions 2 and 3. Both junctions show an $I_C R_N$ product much smaller than the bare Al gap. As a matter of fact, the induced gap in the buffer layer (both Ti and Pt) is rather small and this has consequences also on the critical current of the devices. However, as seen in Table 3, devices with Pt buffer layer have a critical current density and a characteristic voltage which are more than one order of magnitude larger than those with Ti buffer, thus outperforming them.

From the excess current we can also obtain indications on the junction transparency (see Ref. [30]). In junction 2, I_{ex}/I_C is below 4 % (0.03 ± 0.01), thus pointing out to a barrier of $D < 0.3$ (the most likely value being 0.2). This estimate has to be taken with some precaution, due to the poor signal to noise ratio. However, a clear indication of a low transparency interface can be extracted from our data. In junction 3, thanks to a more favorable signal to noise ratio (here I_C is much larger than in junction 2), we can infer a barrier transparency of $D = (0.86 \pm 0.6)$, given by a value of $I_{ex}/I_C = (0.57 \pm 0.03)$.

JJ	I_C (μA)	J_C (A/cm^2)	$R_N A$ (Ω μm^2)	$I_C R_N$ (μeV)	D
1	0	0	8.4	0	not eval.
2	0.070	35	2.4	0.89	< 0.3
3	1.70	$1.4 \cdot 10^3$	1.1	13.9	(0.86 ± 0.6)

Table 2: Physical parameters of junctions 1,2,3.

These outcomes point to a better compatibility of the Pt buffer layer with the TI material, for the creation of a high transparency interface. These devices are therefore good candidates for a complete characterization of the Josephson effect, and for the search of those unconventional features expected in the case of topologically non trivial barriers.

3.3.2 Bi-epitaxial Josephson Junctions

The YBCO devices presented in this work have been realized with the bi-epitaxial fabrication technique [168]. In bi-epitaxial junctions, two

different crystalline orientations of YBCO film are induced using a structured substrate, to obtain a grain boundary. The substrates used in this work are $La_{0.3}Sr_{0.7})(Al_{0.65}Ta_{0.35})O_3$ (LSAT) or $SrTiO_3$ (STO), providing an epitaxial growth of the YBCO film in the (1 0 3) orientation. The template for the growth is defined with a patterned CeO_2 seed layer, which provides a different orientation of the YBCO (0 0 1) film with respect to the one induced by the substrate. The main feature provided is the presence of an off axis electrode obtained thanks to the (1 0 3) orientation of the YBCO film grown on the substrate. This feature most likely determines the lower barrier transitivity that characterizes the transport properties of these devices.

A promising route to further improve the quality of the device is the realization of smaller junctions. Sub-micron HTS junctions have already been used to reduce decoherence [179]. They could prove to be more uniform and of better quality for applications. Measurements on such structures could also provide feedback to improve GB junctions and to clarify the transport mechanisms of GB barriers.

4 A MAGNETIC FIELD CHARACTERIZATION OF THE BISMUTH SELENIDE

This Chapter includes a high magnetic field characterization of the Bi_2Se_3 barrier. Measurements have been performed in Hall bars using the PPMS system described in Sec. 3.2.1. The results of this study are combined with the analysis of scanning tunneling microscopy (STM) performed on the cleaved surface of the sample. STM and SdH oscillations studies are necessary to characterize the typical properties of the Bi_2Se_3 barriers used in our hybrid devices.

4.1 HALL EFFECT IN BISMUTH SELENIDE DEVICES

We describe here the high magnetic field characterization of the Bi_2Se_3 flakes. This study is a fundamental step to gather information on the relevant transport parameters of the barrier, which are used to realize hybrid S-Bi_2Se_3-S devices. We have measured 9 Hall devices (for fabrication detail see Sec. 3.3.1) at low magnetic field ($|B| < 5$ T). Further analysis performed at high field is discussed below.

4.1.1 Low field Hall coefficients

In Fig. 46 we report the typical behavior of the longitudinal (R_{xx}) and transversal (R_{xy}) resistance of Bi_2Se_3 flakes. The longitudinal resistance ($R_{xx} = V_{xx}/I$) has a quasi-parabolic background, which is connected to the band structure of the bulk of the crystal. The transversal resistance

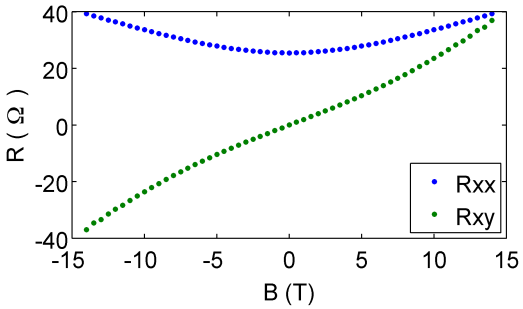

Figure 46: Longitudinal (R_{xx}) and transversal (R_{xy}) resistance of sample Bi_2Se_3X2S19 as a function of the external magnetic field. The longitudinal resistance shows a quasi-parabolic background whereas the transversal resistance have a typical Hall behavior. At high field there are some nonlinear effects, which are discussed below.

is related to the Hall coefficient ($R_{xy} = V_H/I$). For the geometry of the device see Sec. 3.2.4, 3.2.1 and Fig. 47b.

In Fig. 47a we report a typical $R_{xy}(B)$ curve. In the linear regime it gives indications on the sign and the density of the main free carrier of the measured device. The slope of the line is connected to the density of the free carriers ($n_{3D} = 1/etR_H$ - see Sec. 2.1.1 for more details). In 3D systems n_{3D} is expected to be independent of the thickness of the flake, while the most appropriate quantity to be referred in 2D systems is $n_{2D} = 1/eR_H$. This quantity is expected to be independent of the flake thickness, if the transport is purely 2D. In our case the shunting

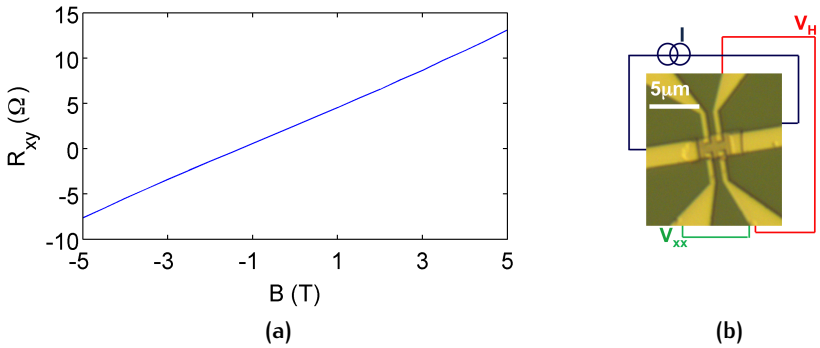

Figure 47: (a) Typical low field Hall effect. The transversal resistance has a linear behavior up to 5 T. (b) Sketch of the measurement setup on an optical image of the device.

effect due to the conduction through impurities in the bulk of the crystal cannot be neglected, therefore both 2D and 3D carrier contribute to the transport. In Fig. 48a we show the behavior of the carrier densities n_{2D}

and n_{3D} as a function of the sample thicknesses t. The thickness of the flake is measured with an AFM tip at one of the edge of the flake, prior to the fabrication.

Following the argument by Jalillo-Herrero [164] clear dependence of both quantities indicates that the transport takes place in a complex structure, created by a parallel of a 2D and a 3D transport channel, namely the bulk and the surface of the crystal. This is confirmed by the behavior of the 2D and 3D Hall coefficients, shown in Fig. 48b. Their behavior can be quantitatively modeled using Eq. 51:

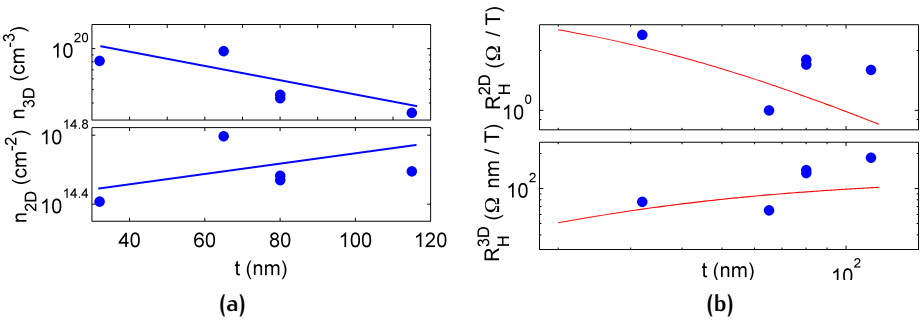

Figure 48: (a) 2D and 3D carrier density as a function of the flake thickness for the 6 Bi_2Se_3 Hall devices realized. Both quantities show a thickness dependence on t, typical of a transport through a parallel of the 2D surface state and the 3D shunting bulk. The behavior of 2D and 3D Hall coefficients as a function of the flake thickness is reported in panel (b). The red line is a model of transport through a parallel of a 2D and a 3D channel, shown in Eq. 51.

This analysis has been performed in a recent paper [164], on Bi_2Se_3 samples. In that case a better control of the thickness and of the level of defects created in the crystal was made possible by the molecular beam epitaxy used for the fabrication. In our case a pronounced data scattering makes the interpretation of the fit less straightforward. This effect can be ascribed to three different reasons:

- uncertainties in the value of the thickness t
- inhomogeneities of the flake thickness
- fluctuations of the defect density from flake to flake, also determined by the different aging of the crystal

However, despite the scattering, our data follows the general trend of the model, plotted as a red line in Fig.48b, yelding the results:

$$\begin{aligned} n_{3D} &= 5 \cdot 10^{19} \mathrm{cm}^{-3} \\ n_{2D} &= 2 \cdot 10^{14} \mathrm{cm}^{-2} \\ \alpha &= 2.5 \end{aligned} \tag{69}$$

A more careful estimation of the carrier density of the 2D channel can be extracted from the analysis of the Shubnikov - de Haas oscillations (see Sec. 4.1.3 below). The estimation of n_{2D}, in this case is in the range between $4.1 - 4.8 \cdot 10^{12}$ cm^{-2}, which is two orders of magnitude below the result of this fit. A discussion about this will be given at the end of the Chapter (Sec. 4.1.3).

4.1.2 Two band analysis

In Fig. 46 it is possible to observe a nonlinear behavior of the R_{xy} at high fields. This effect is typically due to the presence of more than one charge carriers in the device. These effects are traditionally modeled in terms of the conductance tensor, which we achieve using the inversion relation Eq 56.

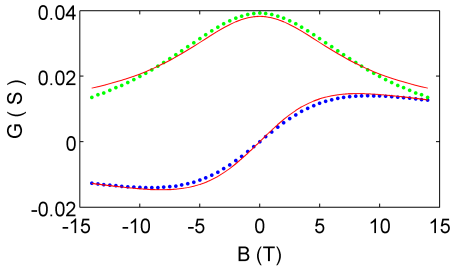

Figure 49: Longitudinal and transversal conductance for sample Bi_2Se_3X2S19. The nonlinearities at high field are typical of a transport through many transport channels (see Figure. 46), and can be fitted with the two carrier model presented in Eq. 58.

In order to drop spurious effects due to the non ideal geometry of the device (Sec. 2.1.1) it is highly desirable to symmetrize the diagonal part of the resistance tensor and an anti-symmetrize the off diagonal elements:

$$\begin{aligned} R_{xx}(B) &= \frac{R_{xx}(B) + R_{xx}(-B)}{2} \\ R_{xy}(B) &= \frac{R_{xy}(B) - R_{xy}(-B)}{2} \end{aligned} \tag{70}$$

In Fig. 49 we show the symmetric (G_{xx}) and anti-symmetric (G_{xy}) elements of conductance tensor, obtained by the inversion of the data in Fig. 46, according to Eq. 56. The data have been fitted using the two band model [94] (see Eq. 58), which confirms our hypothesis about the multiple carriers contributing to the transport.

In order to limit the degrees of freedom of the fit, the model can be re-parametrized:

$$\begin{aligned} G_{xy}(B) &= eB\left(\frac{C_1\mu_1 - C_2}{(\mu_1/\mu_2 - 1)\left(1+\mu_2^2B^2\right)} + \right. \\ &+ \left. \frac{C_1\mu_2 - C_2}{(\mu_1/\mu_2 - 1)\left(1+\mu_2^2B^2\right)}\right) \end{aligned} \tag{71}$$

where C_1 and C_2 can be obtained upon inversion of the system

$$n_1 = \frac{C_1\mu_2 - C_2}{\mu_1\mu_2 - \mu_1^2}; \quad n_2 = \frac{C_1\mu_2 - C_2}{\mu_1\mu_2 - \mu_2^2}$$

The coefficients C_1 and C_2 can be extracted from the low field limit:

$$\frac{G_{xx}(0)}{e} = n_1\mu_1 + n_2\mu_2; \lim_{B\to 0}\frac{G_{xy}(0)}{eB} = n_1\mu_1^2 + n_2\mu_2^2 = C_2$$

which corresponds to the simple case of a Drude model, in the case of a single band.

The result is that data fits quite well the model, giving the results

$$\begin{aligned} n_1 &= 1.5\cdot 10^{14}\ \mathrm{cm}^{-2} \\ \mu_1 &= 1200\ \mathrm{cm}^2/\mathrm{Vs} \\ n_2 &= 6.3\cdot 10^{17}\ \mathrm{cm}^{-2} \\ \mu_2 &= 0.1\ \mathrm{cm}^2/\mathrm{Vs} \end{aligned} \tag{72}$$

Remarkably, the value of n_1 is in a good agreement with the result of n_{2D} in the fit presented in Eq. 69.

This result points to the presence of a low carrier density high mobility band, namely the topologically protected edge state, and a high carrier density band with low mobility.

We have performed a complete characterization of the high mobility band through the study of the Shubnikov - de Haas oscillations. As already pointed out in the discussion of Eq. 69, the carrier density is two order of magnitude higher than the estimation given by the SdH oscillations.

The low mobility band does not match with the estimation given by the Hall effect at low field, and we have two possible explanation for this. On the one hand Eq. 58 holds for a 2D Drude gas with two transport band, therefore the results badly reproduces the contribution of bulk states, which is supposed to be due to impurity states. On the other hand it is possible that a third channel of conductance, coming from the confinement of electrons on the surface of the flake [83], is created in Bi_2Se_3 flakes. It is worth noticing that the second band, in spite of the high carrier density, has an extremely low mobility (2 $\mathrm{cm}^2/\mathrm{Vs}$), therefore negligible contribution is given to the transport.

4.1.3 Shubnikov - de Haas Oscillations

We have studied the high field behavior of our devices. In five of them we observed magnetoresistance oscillations, which we studied through careful characterization at high magnetic field. By slowly sweeping the magnetic field from 0 T to 14 T, we observed small magnetoresistance oscillations on the quite large parabolic background. In Fig. 50 we report the typical behavior of the longitudinal resistance at high field, after the subtraction of the background.

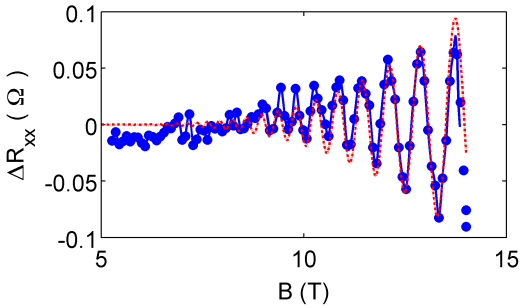

Figure 50: High field oscillations of the longitudinal resistance (sample Bi_2Se_3X2S23) after background removal. The blue line is a spline interpolation and it is a guide for the eyes. The red dashed line in the best fit line according to the model presented in Eq. 73.

The background has been extrapolated with a 4^{th} grade polynomial, to take into account effects related to the geometry of the devices (see Fig. 15 in Sec. 2.1.2). The residual resistance ΔR_{xx} could be studied within the framework of the Shubnikov - de Haas magnetoresistance oscillations (see Sec. 2.3), and it can be fitted with the model [8]

$$R_{xx} \propto \frac{\lambda}{\sinh(\lambda)} \exp\left(-\frac{\pi}{\omega_c \tau_c}\right) \cos\left[2\pi\left(\frac{F}{B} + \frac{1}{2} + \varphi'_B\right)\right] \tag{73}$$

where $\lambda = 2\pi^2 k_B T/\hbar\omega_c$, $\omega_c = eB/cm_c$ is the cyclotron frequency, τ_c is the scattering time and m_c is the cyclotron mass. F is defined by the Onsager's relation (Eq. 64 in Sec. 2.3) and φ'_B is a phase shift related to the presence of a Landau level at zero energy.

Since the theory of the magneto conductance oscillations is formulated in terms of the conductance, it is convenient referring to the conductance tensor. It can be obtained from raw data upon inversion of the resistance matrix, shown in Eq. 56.

In Fig. 51 we report the oscillations of the residual conductance ΔG_{xx} after background removal. The oscillations follow the model presented in Eq. 66

$$\Delta G_{xx} \simeq \cos\left[2\pi\left(\frac{F}{B} - \frac{1}{2} + \beta\right)\right]$$

and they are expected to be equally spaced in the reverse of the magnetic field. The minima of the conductance corresponds to the complete filling of Landau levels, which can be easily identified by simple inspection.

In Fig. 52 we elaborated a fan diagram from our data. As discussed in Sec. 2.3, this is a useful tool for a quantitative analysis of magneto-resistance oscillations. In the figure, the Landau index is plotted as a function of the position in magnetic field of the corresponding minima. To increase the statistics, a semi-integer value was attributed to the position of the maxima. Our data are clearly aligned along a line, as expected in the case of SdH oscillations.

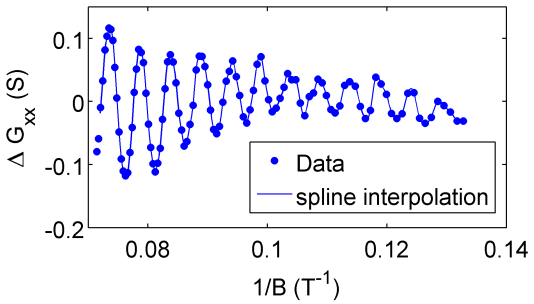

Figure 51: High field conductance oscillations of the flake presented in Figure. 46 vs the reverse of the magnetic field. The longitudinal conductance G_{xx} is obtained upon inversion of the resistance tensor (see Eq. 56) and after background removal. The line is a spline interpolation and guides the eye.

The slope of the line is connected to the frequency F of the oscillations via the Onsager's relation (Eq. 64) [160, 8], and it gives information on the carrier density of the transport channel that generates the oscillations. We have observed a surface carrier density lying in a very narrow range ($4.1 - 4.8 \cdot 10^{12}$ cm^{-2}).

The intercept β, instead, is connected to the Berry phase ϕ_B discussed in Sec. 2.2, 2.3, specifically a semi-integer value of β is compatible with a Berry $\phi_B = \pi + 2n\pi$ and with a hypothesis of Dirac electrons, whereas an integer value of β indicates a $\phi_B = 2n\pi$ and Shrödinger electrons.

The study of the Berry phase, as well as the study of the oscillations as a function of the angle (proposed below), indicates that the oscillations arises from a topologically protected 2D edge state.

Determination of the Berry Phase

To increase the precision of the fit, as shown in Fig. 52, we have extrapolated the frequency of the oscillation through a Fourier transform analysis. In the inset of the figure we report the FFT spectrum of the signal. The signal clearly shows a Lorentz peak, corresponding to the frequency F, and a $1/f$ background, which is related to the noise

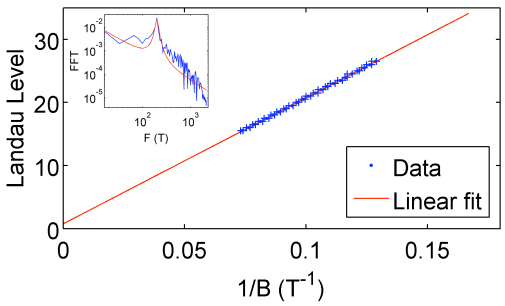

Figure 52: Fan diagram of data presented in 51. The red line is a best fit line. The slope of the line is obtained from the Fourier of SdH oscillations (shown in the inset): $F = (200 \pm 15)$ T. The value of intercept if extracted from the fit. We obtained a value of $\beta = (0.76 \pm 0.16)$, which is an intermediate value between 1 (i.e. Shröedinger electrons) and 0.5 (i.e. Dirac electrons). In the inset: FFT of the signal with a Lorentz peak. The red line is the best fit for the Lorentz curve plus a $1/f^{\eta}$ background.

present in the measurement, which can be discharged. The analysis of the FFT spectrum evidenced a single frequency of oscillations. No hint of beatings was observed on the measured devices.

To achieve a reliable estimation of the Berry phase, we have tried two different strategies, with controversial results. On the one hand we extrapolated both the slope and the intercept from the fan diagram, on the other hand we extrapolated the slope directly from the FFT, as discussed above and in Ref. [8]. In the case of the sample shown in Fig. 52, the two analysis gives a substantially equivalent result, in other cases (not shown here, see [70]) the results of the two analysis might be conflicting. The conclusion is that the results of the fan diagram can be significantly affected from the uncertainties of the measurements and, especially when the Landau levels are populated up to high indexes, the results have to be taken 'cum grano salis'. The value of the Berry phase can be firmly established only populating low order Landau levels (close to $N = 1$). In our case this would require much higher fields certainly higher than 30 T. However, the information given by the fan diagram can be integrated with complementary analysis (like STM), as reported in Sec. 4.2 and in Ref. [70].

Shubnikov - de Haas Oscillations in 2D and 3D

As discussed in Sec. 2.3, SdH are not a unique feature of 2D system, but they can also appear in 3D systems, under suitable conditions. To prove that the oscillations are generated by the 2D edge state of the system, a study of the behavior of the oscillations as a function of the angle is necessary. We swept the field from 0 T to 14 T, with different orientation

of the sample in the magnetic field. In Fig. 53a we present the resistance oscillations as a function of the normal component of the magnetic field. The angle θ represents the angle between the the magnetic field and the direction orthogonal to the transport plane.

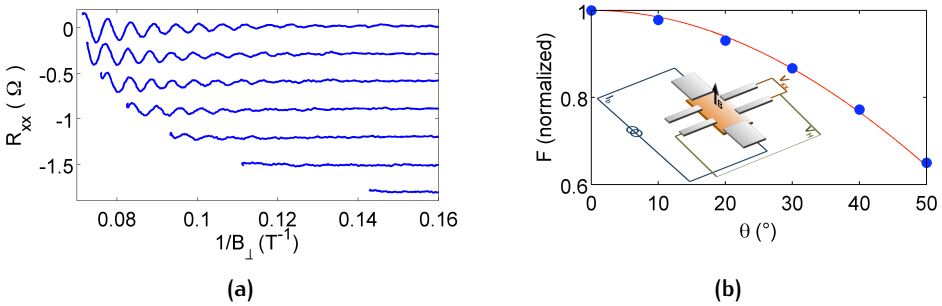

Figure 53: (a) SdH oscillations as a function of the normal component of the magnetic field for sample Bi_2Se_3X2S19. The curves corresponds to different angles θ between the transport plane and the magnetic field, namely 0°, 10°, 20°, 30°, 40°, 50° and 60°. Above 50° no oscillation can be detected. Curves are shifted for clarity. The position of the minima of the different curves are aligned, as expected in the case of a 2D transport. (b) Frequency of the SdH oscillations as a function of the angle θ. The curves follow the ideal cosine behavior, shown in red, valid for a 2D transport up to 50°. The inset shows a sketch of the measurement setup.

In the case of a 2D transport, only the normal component of the field is effective to the oscillations, therefore the position of the minima of the oscillations are fixed with respect to the $B_\perp$ component, and differently from what observed in the case of oscillations arising from a 3D trivial band [70, 58, 152, 6, 166]. As a further check we determined the frequency F of the oscillations for the different angles, and studied this dependence (see Fig.53b). The modulation of F as a function of the angle θ follows a cosine curve up to at least 50°, as expected in the case of a 2D transport [152], and differently from the ellipsoid shaped Fermi surface expected for the bulk band structure of the Bi_2Se_3.

A Comparative Analysis

Shubnikov-de Haas oscillations have been studied on various Bi compounds with different interpretations
[58, 175, 152, 35, 193, 166, 83, 185, 164, 195, 6, 174]).

Specifically, the presence of SdH oscillations in Bi_2Se_3 samples can be connected, in some circumstances, to the spurious effect of the 3D oscillations related to the bulk electrons [26]. In this case, as discussed by Eto et al. [58] in a recent paper, the SdH oscillations can be seen for any direction of the magnetic field (see Fig. 54a). For instance some

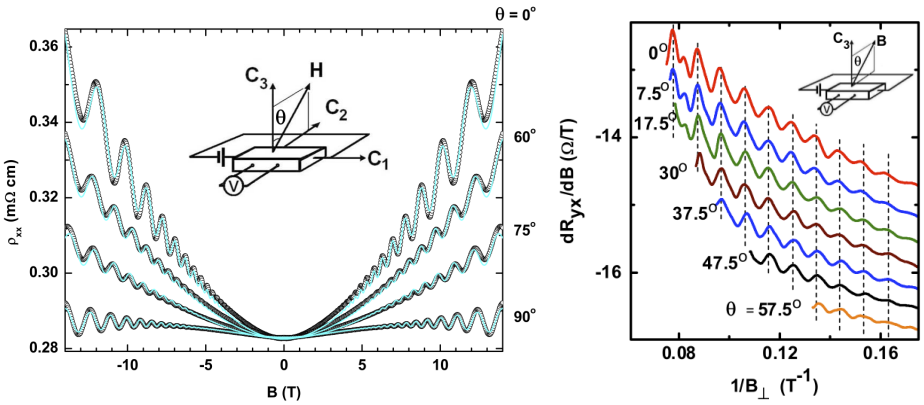

(a) adapted from Ref. [58] **(b)** adapted from Ref. [175]

Figure 54: SdH oscillation in Bi_2Se_3 devices in the case of a prevailing 3D transport channel (a) and in the case of a transport through the topological edge state (shown in panel b).

measurements performed by the same group [175] on a Bi_2Se_3 thin films, obtained from MBE deposition, a completely different angular dependence was observed (see Fig 54b). In this case the peaks are rather well aligned, when plotted as a function of the normal component of the magnetic field $B_\perp$, in complete agreement with our data (see Fig. 53a). This angular dependence was attributed to a transport through the topological edge state of the material.

The reason of the different transport regimes can be attributed to the different contributions given to the transport from the topological surface state and the bulk transport. When the transport is mediated by the bulk, the oscillations have poor angular dependence, and can be found even at $\theta = 90°$. When instead the transport takes place in the topologically protected edge state, the oscillations shows the typical $\cos\theta$ dependance shown in Fig. 54b, 53a.

In the case of Ref. [58, 175], the different contribution was basically tuned with thickness of the material (Bi_2Se_3 flakes in Ref. [58] and MBE thin films in Ref. [175]). However, a similar effect was detected in a work by Qu et al. [152] on Bi_2Te_3 MBE thin films, by tuning the quality of the crystal. In fact the Authors were able to observe a crossover from a condition of oscillations clearly arising from a 3D spurious effect (in low quality films, N1 in Fig. 55) to oscillation showing the typical features of a pure 2D transport (in high quality film, Q1 in Fig. 55). Specifically while in high quality films the behavior of the oscillations as a function of the angle θ follows the expected cosine dependence, in low quality films the frequency still modulates, but without the cosine behavior, especially at higher angles ($\theta > 30°$). In this work, the quality of the film was

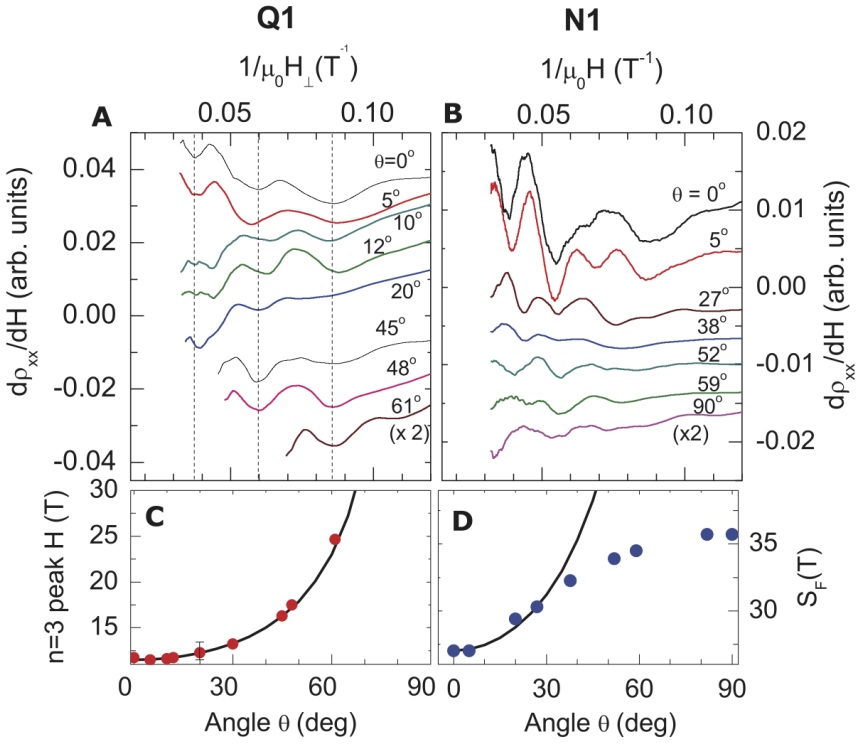

Figure 55: SdH oscillations in the Bi_2Te_3 thin films for various film quality. High quality devices supports a purely 2D transport, as clearly evident from the figure (A), including a cosine dependance of the frequency of the oscillations (C). In the case of low quality films, instead, the oscillations are present at all angles of the magnetic field (B). However the frequency of the oscillations still changes as a function of the angle (D), but the dependence does not follow the cosine dependence behavior (adapted from Ref. [175]).

changed by an intentional deterioration, obtained upon film exposure to the atmosphere for a long time.

The different, and sometimes controversial outcomes found in literature on the nature of SdH oscillations in tetradymite chalcogenides can be therefore accounted on the different quality and thickness of the material, including the different fabrication techniques.

Quite recently [35] SdH detected on Bi_2Se_3 flakes were attributed to an effect of a possible layered bulk material, having therefore a cylindrical Fermi surface (implying a cosine dependence of the frequency of the oscillations as a function of the angle, as shown in Fig. 56). In this work the Authors also extracted a $\varphi_B = 0$ phase, in agreement with the absence of Dirac electrons. However, the conclusion of this paper are not completely convincing under some aspects. In fact in this paper the angular dependence of the frequency of the oscillations is only traced for $\theta < 45°$. Moreover, the Berry phase was extracted from the minima of resistance, and for values of the magnetic field allowing only a depletion of the highest Landau levels ($n > 10$) (see Sec. 2.3.3).

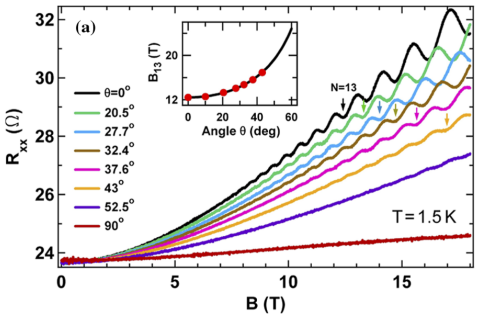

Figure 56: ShD oscillation on Bi_2Se_3 flake, showing a cosine dependence. The Authors extracted a value of the Berry phase $\varphi_B = 0$. The effect was attributed to a 3D Hall effect, related to the presence of a stack of parallel 2D transport planes in the material (adapted from Ref. [35]).

As mentioned in some recent papers [193, 194, 8], in the regime where $R_{xy} \ll R_{xx}$ the inversion of the conductance matrix is non trivial, therefore some cautions must be taken in the analysis of the SdH oscillations (see Sec. 2.3.3), to avoid misleading results. This behavior is rather different from the case of graphene [142, 120, 207], and implies that in the evaluation of the Landau Level index from the R_{xx} might be dangerous. In our case this ambiguity is avoided by directly referring to the minima of the ΔG_{xx} as shown in Fig. 51, 52.

4.2 SCANNING TUNNELING MICROSCOPY ANALYSIS

Transport data obtained from Shubnikov - de Haas oscillations can be efficiently combined with the analysis of the scanning tunneling microscopy (STM). The analysis was performed on the cleaved surfaces of the Bi_2Se_3 crystal at the temperature of 2 K with an ultra high vacuum (UHV) Unisoku USM-1300 STM.

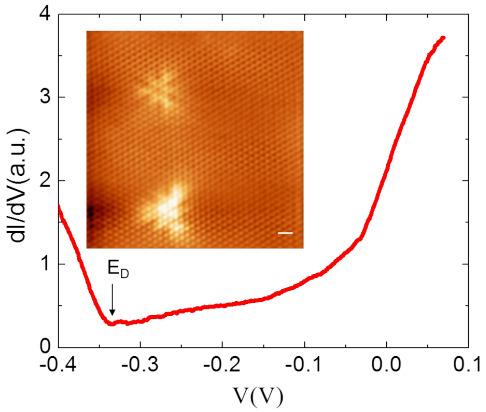

Figure 57: Tunneling conductance spectrum acquired at the surface of a Bi_2Se_3 crystal. The spectrum has been measured with a bias modulation amplitude V_{mod} = 2.5 mV_{rms}. The V-shaped spectrum is consistent with the Dirac dispersion with the Dirac point at $V = -350$ mV (minimum of the spectrum indicated by the arrow and labeled as E_D). The inset is an atomic resolved topographic image showing triangular shaped defects. The imaging conditions are: $V = +0.1$ V, I = 10 pA, scan area is 14.5 nm x 14.5 nm (scale bar is 1 nm).

In Fig. 57 a typical conductance spectrum is reported. The spectrum exhibits a V-shape with a minimum at $V = -350$ mV, representing the Dirac point. The presence of the Dirac point located below the Fermi level has already been reported in literature [79, 38, 81, 86] and it has been attributed to the presence of defects. The inset of Fig. 57 is a topographic image of the (0 0 1) surface of the crystal, and it reveals the presence of triangular shaped defects with a typical spacing of few nanometers. Defects in Bi_2Se_3 crystal are mainly typically due to Se vacancies and defects in the Bi plane [3, 2, 28, 27].

STS spectra have been captured with a magnetic field perpendicular to the sample surface. Peaks are clearly visible above 5 T (Fig. 58a), signaling the presence of not equally spaced Landau levels. Defects are known to suppress the topological edge state in Bi_2Se_3 crystals.

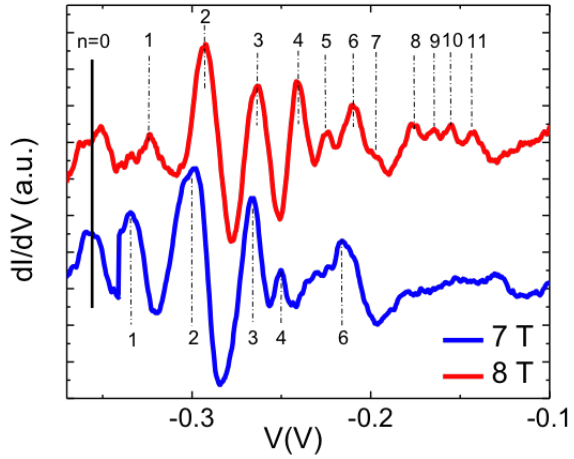

(a)

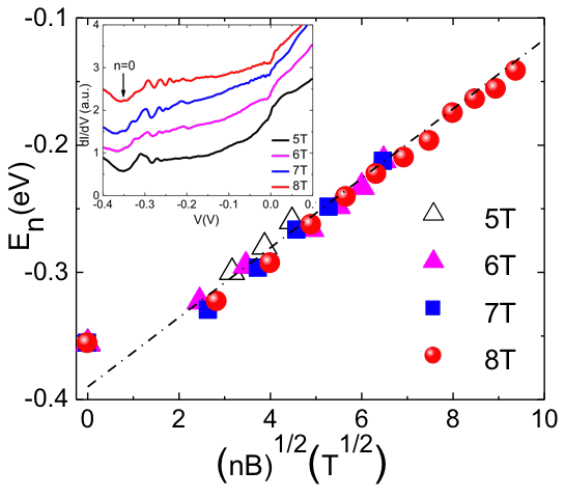

(b)

Figure 58: (a) Tunneling conductance spectra captured in the presence of a magnetic field applied perpendicular to the sample surface. The spectra measured at the value of the magnetic field of at 7 T (in blue) and 8 T (in red) are shown, after a polynomial background subtraction. After the subtraction the Landau levels are clearly visible and they can be labeled. Curves have been shifted for clarity. (b) Landau levels energy E_n follows the aperiodic spacing, proportional to $\sqrt{nB}$. Moreover the presence of a peak at $N = 0$ is evident from magnetic field above 6 T. The position of the $N = 0$ peak does not depend on the field, as expected for Dirac electrons. The inset shows raw data for the tunneling spectra above 5 T, showing a series of peaks associated with the formation of the Landau levels.

However, for the defect density observed in our samples ($\simeq$ 10 nm) is still possible to observe the presence of Landau levels in STM measurements, as pointed out in the work by Chen at al. [38]. Our samples in fact are comparable with the sample (b) of their work (see Fig. 59). For this reason, the oscillations detected at the STM are dominated by a strong background. Only upon an accurate subtraction of the background, in fact, the oscillations clearly appear, and can be labeled (see Fig. 58a the inset of Fig. 58b).

The energy dependence of the Landau levels is given by [36]

$$E_n = E_D + \mathrm{sgn}(n) v_F \sqrt{2e\hbar|n|B} \tag{74}$$

where E_n is the energy of the nth Landau level, $n = (0, \pm1, \pm2 ... \pm n)$ is the Landau level index, E_D is the Dirac point, v_F the Fermi velocity, $\hbar$ is the Plank constant and B the magnetic field [208].

In the inset of Fig. 58b the peaks at magnetic field of 7 T and 8 T are shown, after background subtraction. A plot of E_n versus $\sqrt{nB}$ reveals a reasonable good linear behavior above the Dirac point as expected for the dispersion of a topological insulator (Fig. 58b). Moreover the presence of peak corresponding to $n = 0$, at the Dirac point, that is independent of the applied magnetic field strongly supports the hypothesis of Dirac electrons. Indeed, in the case of a conventional two dimensional electron gas with a parabolic dispersion this level does not exist.

No Landau levels were observed below the Dirac point. This is consistent with previous reports on Bi_2Se_3 crystals [38] and it can be attributed to a coupling to the bulk valence band located just below the Dirac point.

4.3 CONCLUSIONS

Our data supports the hypothesis of a major role played by the topological edge state in magneto-resistance oscillations [70]. This is confirmed by a detailed study of the behavior of the SdH, which followed the ideal cosine behavior up to 50° (see Fig. 53a, 53b). What is instead an issue in our measurements is that we cannot establish, from the SdH oscillations that the 2D gas consists of topologically protected Dirac states. Indeed, depending on the way we extract the frequency of oscillations, we get a Berry phase zero (trivial 2D states) or π (topologically protected states). In our work the final confirmation that we are dealing with topological protected edge states, comes from the STM analysis. STM in magnetic field confirms the Dirac-fermion nature of the surface states, because massless Dirac fermions present peculiar

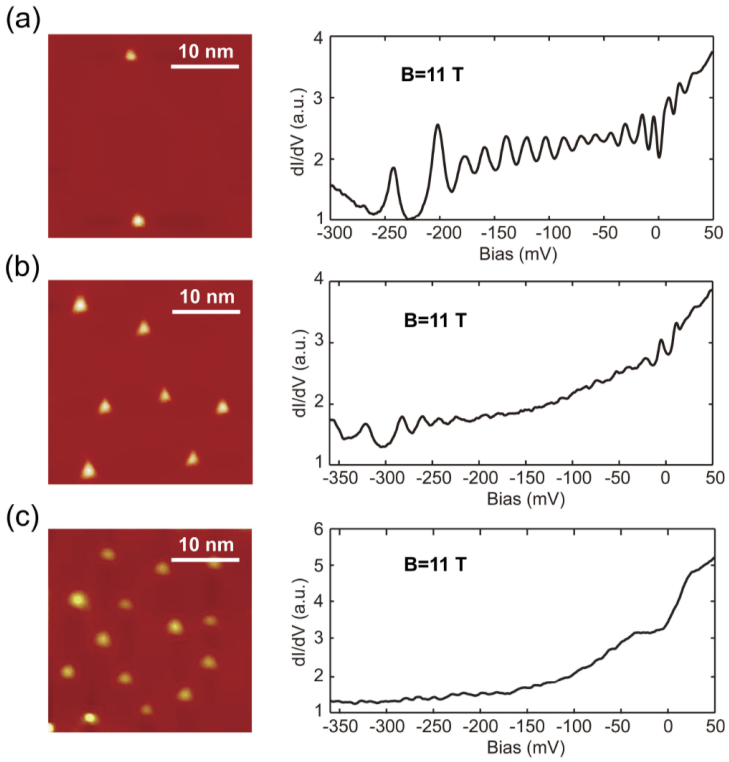

Figure 59: STM of Bi_2Se_3 thin films and the relative spectra, acquired in a static magnetic field of 11 T. The oscillations are suppressed as the density of defects in increased. However in a moderate level of defects, as for instance is the case of our samples (cfr. Fig. 57), the the oscillations are clearly visible in the measurement (adapted from [38]).

Landau quantization with a level spacing changing as $\sqrt{nB}$ and the zero-energy Landau level pinned at the Dirac point.

Measurements performed in high magnetic field measurements are able to reveal the presence of a high mobility 2D channel, while at low field we expect contribution to the transport coming also from the bulk states of the crystal. This result supports the hypothesis that the mobility of the surface states is much larger than those of bulk states, thus a negligible contribution to the conductance oscillations is coming from the bulk states.

5 PROXIMITY EFFECT IN BISMUTH SELENIDE BARRIERS

The new frontiers of material science and nanotechnology offer a variety of different barriers, where proximity effect controls the coherent propagation of Cooper pairs. Innovative devices offer specific functionalities, obviously related to the nature of the barrier (topological insulators, graphene, semiconductors, ferromagnets, nanowires, etc.), and to the possibility of being hybridized with superconductors. Here we focus on those devices which use topological insulators as barriers. This study has great relevance on the propagation of coherence in edge states, where in addition a Dirac cone in the energy dispersion comes from the topological band structure of the material. The follow-up of this study includes the characterization of the superconductivity on topologically non trivial configurations, and in the long run the study of Majorana fermions. These are zero energy states which are expected to be free from decoherence effects thanks to their topological protection.

We refer to junctions employing both Bi_2Se_3 barrier exfoliated from single crystal and Bi_2Te_3 thin films, presented in the next Chapter (Chap. 6). A consistent picture emerges from our measurements, with clear indication of ballistic transport regime in the edge states. Quantitive differences determined by the different fabrication procedure, as discussed in Sec. 3.1, come from the different gaps of the materials and from their morphology, which also implies different thickness of the barrier.

The ballistic nature of transport is proved by the the temperature dependence of the critical current. The analysis of I-V curves in presence of magnetic field and microwaves allows a full characterization of the junctions and of their transport modes.

This Chapter includes most of the experimental results on the characterization of the proximity effect in Al/Bi_2Se_3/Al structures (see also Sec. 3.3.1). We have realized and characterized about 15 coplanar Josephson junctions and SQUIDs. Devices have been realized using flakes of Bi_2Se_3 single crystals and an e-beam lithography, combined with a lift off procedure, to define the geometry of Al electrodes. More details on the fabrication technique are presented in Sec. 3.1, 3.3.1.

5.1 MEASUREMENT SETUP

Measurements are performed in a four probes configuration, using a slow current bias to polarize the junction. Most of data presented in this paragraph have been measured in an Oxford Heliox VS system (base temperature 250 mK). Data relative to device Bi_2Se_3X2S20 have been measured with an Oxford Kelvinox MX cryostat (down to 20 mK) Some stages of cryo-filters and a room temperature stage of lowpass filters are used to reduce the noise of the measurement, and to reduce the heating effect of the lines. Further details on the measurements scheme are discussed in Sec. 3.2.4.

Figure 60 shows a typical resistance vs temperature (R(T)) measurement (Bi_2Se_3X2S20). Measurements are performed in a four probe configuration (see Sec. 3.2.4), with a standard lock in technique. By lowering temperature, the R(T) follows a metallic-like behavior, down to the temperature of 50 K. Below 50 K the resistance is constant and at about 1.1 K (critical temperature of Al) an abrupt drop of R takes place. Below this temperature a quite broadened transition, characteristic of a progressive transition to the superconducting state [71], was observed. Below 600 mK the resistance is zero.

As discussed in Sec. 3.3.1, the devices presented in this work are realized following two main recipes: some samples were fabricated using a Ti thin layer between the Al electrodes and the Bi_2Se_3 flake, in other devices, instead, a Pt buffer layer was used. The role of the buffer layer is to tune the transparency of the interface. Specifically high transparency devices were achieved with Pt buffer layer, whereas a Ti buffer layer determines low transparency barriers.

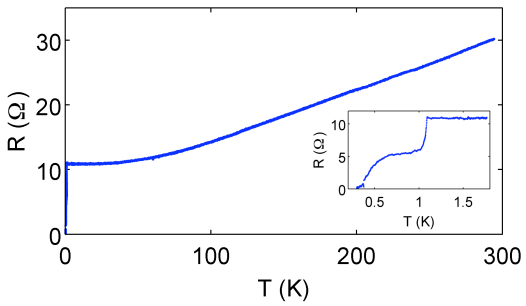

Figure 60: Resistance vs temperature plot for a typical device (sample Bi_2Se_3X2S21). The graph shows a metallic-like behavior down to 50 K, and a flat plateau below this temperature. The inset shows a zoom of the lowest temperatures. The abrupt drop of resistance at 1.1 K has to be attributed to the superconducting transition of the Al electrodes. Below this transition, a progressive transition to the superconducting state was observed.

5.2 IV CURVES AND THEIR TEMPERATURE DEPENDANCE

In Fig. 61 we show the IV curves of two devices, one Al/Pt electrodes (Fig. 61a) and one with Al/Ti electrodes (Fig. 61b). The Pt buffer layer device is characterized by a high critical current density ($1.4 \cdot 10^3$ A/cm^2), and a high transmission coefficient ($D = (0.86 \pm 0.06)$), estimated from the excess current I_{ex} as described in Sec. 1.3. The high critical current density is also reflected into a relatively high characteristic voltage ($I_C R_N/e$), which in this case is about 14 μV, when compared with the $I_C R_N$ product of the Pt buffer layer device. The critical current density of this device, as well as the characteristic voltage and the transmission coefficient are significantly lower ($J_C = 140$ A/cm^2, $D = (0.6 \pm 0.1)$, $I_C R_n/e = 1.6$ μV).

The lower values of the $I_c R_N$ product of the junction, compared to the values expected form the Ambegaokar and Baratoff model [5] (see Sec. 1.3 and Eq. 21) reveals a suppressed effective gap, consistently with all measurements performed up to now [185, 158, 191, 153, 146] (see Tab. 3). The reason of this is mainly connected to the interface between the superconducting electrodes and the TI barrier. Moreover, bulk shunt strongly increases the conductivity of the sample, thus reducing the measured R_N. Despite an almost identical geometry, the samples with a Pt buffer layer show a critical current which is an order of magnitude larger than those with Ti. The actual IV curve is determined by both the effects. It is difficult to disentangle the two components because the ratio between the surface and the bulk resistivity in our samples cannot be easily determined. This is a common problem of coplanar S-TI-S

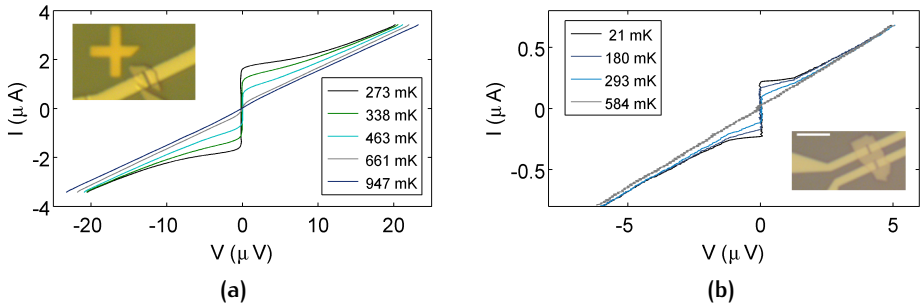

Figure 61: (a) IV curves as a function of temperature for a sample (Bi_2Se_3X2S24) with a Pt buffer layer. Typical critical current densities of 10^3 A/cm^2 can be observed for this type of device. The inset shows an optical image of the device. The cross marker is 5 μm wide. The same plot is presented in (b) for a sample (Bi_2Se_3X2S20) with a Ti buffer layer, in this case the critical current density is more than one order of magnitude lower (35 A/cm^2). The scale bar is 5 μm

junctions, when the bulk conductivity of the barrier is not negligible [185, 158].

Information on the proximity effect can be also tracked through the features of the IV curves at finite voltage pointing to over-damped behavior (see Sec. 1.5). Specifically all devices showed rounded, non-hysteretic IV curves. The nonlinearity falls on a rather linear sub-gap resistance, at a typical voltage which is much lower than the superconducting gap. The voltage at which the IV curve falls in a linear regimes scales quite well with the $I_C R_N$ product. This framework is consistent with a picture of S-I-N-I-S junction, showing suppressed values of critical current density and $I_C R_N$ with respect to standard S-N-S devices [31, 32, 201].

Figure 62 shows typical IV curves at higher bias. The curves have an almost linear sub gap resistance, with no significant features (such as peaks or kinks in corresponding to the Al gap), as confirmed by the analysis of the conductance spectra, numerically elaborated from raw data (see inset of Fig. 62). Figure 63 shows the IV curves of device Bi_2Se_3X2S20, with the result of the RSJ fit [14] (see Sec. 1.5, Eq. 34).

$$\langle V \rangle = \frac{2}{\gamma} R_N I_C \frac{e^{\pi\gamma i} - 1}{e^{\pi\gamma i}} \mathcal{I}^{-1}$$

5.3 FITTING PROCEDURE OF THE $I_C(T)$

The study of the behavior of the critical current as a function of the temperature is a crucial analysis to gather information on the relevant

Ref.	Dev.	L (nm)	I_c (μA)	$\frac{eI_cR_n}{\Delta}$	D	μ ($\frac{m^2}{Vs}$)	n (cm^{-2})
Bi_2Se_3 X2S20	Al/Pt Bi_2Se_3	400	0.228	0.011	0.6	> 0.15	4.1 - 4.8 10^{12}
Bi_2Se_3 X2S24	Al/Ti Bi_2Se_3	300	1.67	0.086	0.9	> 0.15	4.1 - 4.8 10^{12}
[185]	Nb Bi_2Te_3	50	18	0.02	-	0.8	1.2 10^{12}
[158]	Al Bi_2Se_3	400	0.3	0.073 - 0.093	-	0.5	1 - 5 10^{12}
[191]	Al Bi_2Se_3	45	0.850	0.067 - 0.267	-	-	-
[153]	Nb InSb	30	0.45	0.13	> 0	-	-
[146]	Nb HgTe	200	3.8	0.19	0.5	2.6	0.5

Table 3: Comparison of the parameters of two of the junctions realized in this work with those available in the literature.

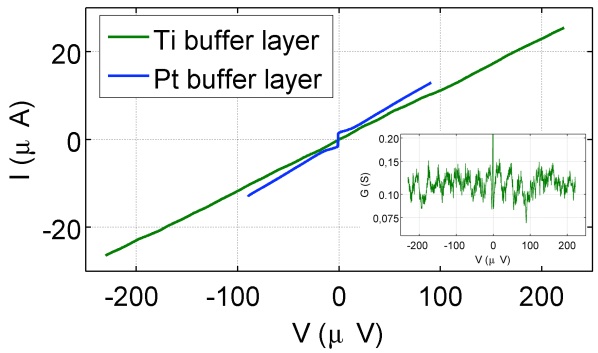

Figure 62: Typical IV curve (sample Bi_2Se_3X2S21 in green and Bi_2Se_3X2S24 in blue) at high bias at the temperature of 20 mK. The sub-gap branch shows no significant structures, up to the value of $\Delta/e = 130$ μV. This is confirmed by the conductance spectra, shown in panel. The inset shows the conductance spectrum of sample Bi_2Se_3X2S21 The spectrum have been numerically elaborated and digitally filtered, after data smoothing. The narrow zero bias peak is determined by the dissipation-less current of the IV curve.

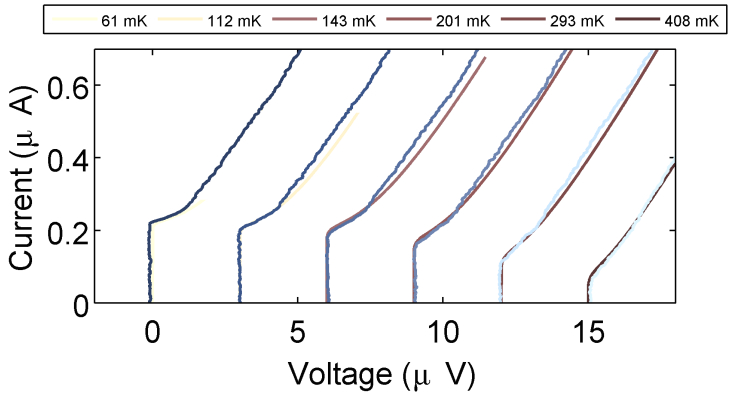

Figure 63: RSJ fit for the IV curves of sample Bi_2Se_3X2S20 (in red scale). In the legend we report the temperature used to fit our data, which are the same of the measured temperature of the corresponding IV curve (in blue scale). Curves are shifted for clarity.

parameters of the proximity devices [19, 4, 180]. Specifically the $I_C(T)$ gives information of the transport regime of the junction, and also on the coherence length of the normal barrier (see Sec. 1.4). Our junctions gave evidence of a ballistic transport regime. Moreover the junction is believed to be in a regime which lies in between the long and short junction approximation. This means that the length of the junction L is comparable with the coherence length ξ_n. Therefore, by increasing the temperature it is possible, to go from a regime where the transport is strongly influenced by the superconducting gap, to a more conventional regime, fully supported by the Andreev bound state, as discussed in Sec. 1.4.

In Fig. 64 we report the critical current as a function of the temperature ($I_C(T)$) for the two devices presented in Fig. 61, in normalized units. The two datasets show a remarkable agreement, falling on the same curve. Sample Bi_2Se_3X2S20 has been measured down to 20 mK, in the Oxford Kelvinox MX dilution refrigerator [70] (see Sec. 3.2.3). A wide temperature range allows a more accurate fitting procedure.

In the high temperature range data can be simulated using an analytical model [105, 111]

$$I_c(T) \propto \sqrt{T} e^{-\frac{2\pi k_B T}{E_{th}}} \tag{75}$$

where E_{th} is the Thouless energy. A value of the Thouless energy of about $E_{th} = 100\ \mu eV$ gives a fairly good fit of experimental data above 150 mK. Below this temperature, the validity of Eq. 75 breaks down as $k_B T < E_{th}/2\pi$. The estimate of the Thouless energy is comparable with

the gap of aluminum ($e\Delta = 130\ \mu eV$). Therefore the junction lies in an intermediate regime between the long and short junction limit [19], as discussed before. From the value of the Thouless energy it is possible to extract an estimation of the coherence length ξ_n of the device at 150 mK. For both junctions considered here we achieved a value of ξ_n of about 3 μm. Since $\xi_n \gg L$, the junction is in a fully ballistic regime.

A simulation of the experimental data in the whole temperature range requires a numerical ballistic model [69] (see Eq. 28 in Sec. 1.4), first proposed in Ref. [185]

$$I = a\frac{2}{\pi}ek_F^2\frac{k_B T}{h}\sin(\chi)\sum_{\omega_n}\int_0^1 \zeta\, d\zeta \frac{t^2}{Q^{1/2}(t,\chi,\zeta)}$$

The pre-factor of Equation 28 is connected with the normal resistance of the sample R_N which is unknown, due to the shunt of the surface state with the bulk states. R_N is therefore a fitting parameter, as done in Ref. [185].

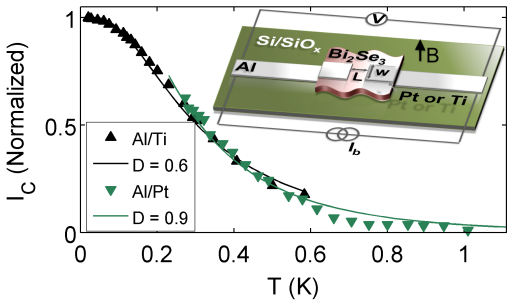

Figure 64: Critical current vs temperature for the two presented devices (Bi_2Se_3X2S20, Bi_2Se_3X2S24) in normalized units. A remarkable agreement between the two datasets can be observed. The continuous lines are the results of numerical simulation of the Eilemberger model presented in Eq. 28, performed using a value of the transparency extracted for the excess current of the IV curve. The inset shows a sketch of the measurement setup.

The ballistic transport supports the hypothesis of a transport through the topologically protected surface states of the TI. An inconsistent scenario would arise in the hypothesis that the transport is carried by the bulk of the crystal, as in this case the presence of defects would determine a diffusive regime of transport. As a further check we made an attempt to fit experimental data in the diffusive regime through Usadel equations Sec. 1.4, providing a not self consistent scenario and yielding unphysical values of the fitting parameters.

Specifically we discuss below in more details the various scenarios, which could nominally reproduce the behavior of experimental data in different the frameworks presented in Sec. 1.4, for the junction with the Ti interface (Bi_2Se_3X2S20).

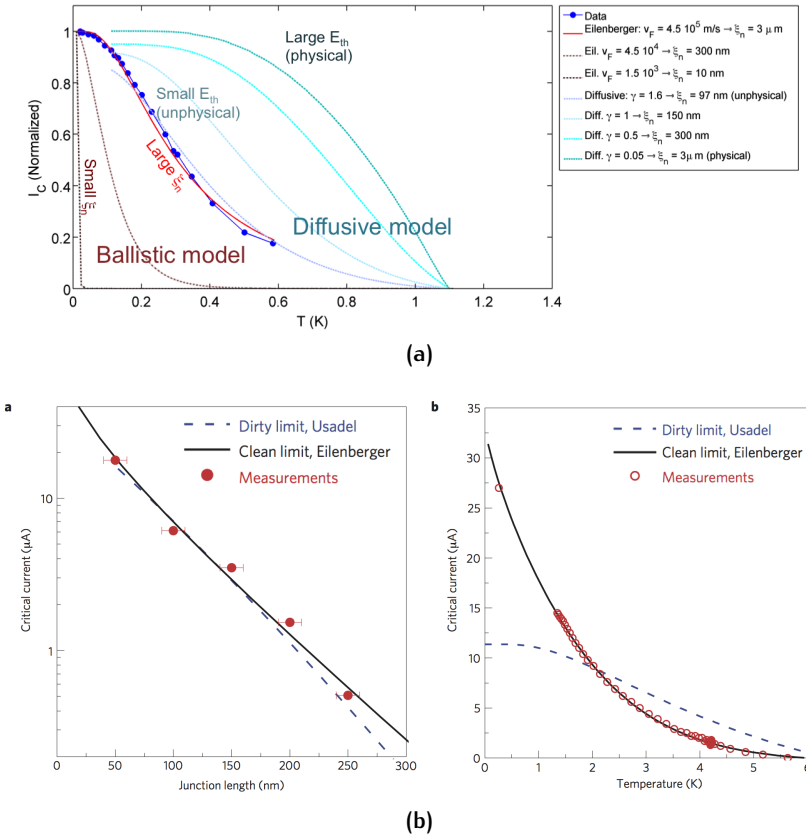

Figure 65: (a) Experimental data of the $I_C(T)$of junction (Bi_2Se_3X2S20), also shown if Fig. 64, where we have added a few additional curves to clarify how a diffusive approach leads to an unphysical scenario. A ballistic approach with a coherence length below 300 nm gives a temperature dependence of the critical current very different form the experimental results. (b) $I_C(T)$ and $I_C(L)$ curves of $Nb/Bi_2Te_3/Nb$ junctions (adapted from Ref. [185]) are in complete agreement with the outcomes of our fit. This outcome was interpreted as a superconducting transport along the topologically protected edge state of the material.

A simulation based on the Usadel model was obtained by Cuevas et al [Priv. Comm.]. The model does reproduce experimental data, but it yields unphysical values of the fitting parameters (see Fig. 65a). Specifically the Thouless energy obtained is 0.2Δ in contrast with our estimation of 0.8Δ (obtained from Eq. 75). Moreover a resistivity of the barrier lower than the resistivity of the Al electrodes was extracted, which is clearly unphysical. This corresponds to a value of $\gamma = \rho_S\xi_S/\rho_N\xi_N > 1$, according to the parametrization of the model [185, 180, 107] discussed in Sec. 1.4. For the validity of the model [185] this parameter should be $\gamma \ll 1$. A Usadel simulation performed with physically reliable parameters, instead, is clearly different with what observed in the experiment. This result is in complete agreement with the outcomes published in Ref. [185] (see Fig. 65b).

The hypothesis of ballistic transport is confirmed by the successful simulation of our data with the Eilenberger clean model. A satisfactory agreement with experimental data is in fact possible using a Fermi velocity of $4.5 \cdot 10^5$ m/s and a transparency coefficient of $D = 0.6$.

A short (i.e. $\xi_n < L = 300$ nm) coherence length corresponds to lower values of the Fermi velocity, one order of magnitude below what found in literature. However, the result of the Eilenberger simulation performed with different values of v_F ($4.5 \cdot 10^4$ m/s and $1.5 \cdot 10^3$ m/s) gives a temperature dependence of the critical current very different form the experimental results, as shown in shown in Fig. 65a.

5.4 EFFECTS OF MICROWAVES AND MAGNETIC FIELD

To study the nature of dissipation-less transport in our junctions, we have performed measurements of IV curves in presence of microwave irradiation and magnetic field. The presence of Majorana bound states in the mid-gap energy spectrum of the junction is expected to modify the current phase relation (CPR) to a 4π periodic function [18, 161, 150, 64, 65], as discussed in Sec. 2.4. Therefore phase sensitive measurements are good candidates to study the topological nature of Josephson junctions with a TI barrier. Nevertheless if the junctions supports a multimodal transport regime [161, 186, 183] there is a combined effect of a 2π periodicity, coming from the trivial transport modes, and a 4π periodicity, due to the topological states. In these conditions the Majorana phenomenology is expected to be masked. Our

junctions support a multichannel transport regime ($N \simeq 500$), as extracted from the value of the normal resistance

$$G_N = \frac{1}{R_N} = N G_0 \tag{76}$$

with $G_0 \simeq 3.874 \cdot 10^{-5}$ S. With a prevailing 2π periodic CPR.

The modulations of I_C in an external magnetic field, and a study of the Shapiro steps are also important to give a detailed characterization of the Josephson coupling (see Sect. 1.2). Our Junctions showed an ideal Josephson behavior, including the typical modulations of the critical current in magnetic field and the modulation of the Shapiro steps (described below), which were in a complete agreement with the expected behavior.

5.4.1 Microwaves

We have detected Shapiro steps in the interval of $15 - 4$ GHz, confirming the presence of the a.c. Josephson effect. In Fig. 66a typical IV curves with an increasing microwave radiation power are displayed.

The position of the steps is connected to the frequency of the microwaves by the relation

$$\nu = \frac{2e}{h} V \tag{77}$$

where $2e/h \simeq 483.6$ MHz/μV. This is a fundamental relation, which is determined by the periodicity of the current phase relation (see Sec. 1.2.3).

Figure 66b shows conductance curve, numerically elaborated from IV the curves, as a function of the temperature. The position of the peaks indicates the position of the Shapiro steps, clearly temperature independent. The position of the Shapiro steps has been verified in various junctions and SQUIDs at different frequencies, giving a strong evidence of a standard current phase relation. A four periodic CPR would generate Shapiro steps at a voltage position $V = h/e\mu$, which is doubled with respect to the conventional relation [18, 153] (Eq. 77). The amplitude of the steps, instead, is modulated by the power of the applied microwave field.

In the case of multimodal modes, a possible scenario is that the $h/2e$ periodic (i.e. topologically trivial) steps have a suppressed amplitude modulation, especially at low RF power, in presence of a strong ($B > 2$ T) magnetic field. In Ref. [153] the IV curve of a Nb/InSb/Nb nanowire junction was measured in a 3 GHz microwave radiation, for different values of the magnetic field up to 2.2 T. The use of Nb

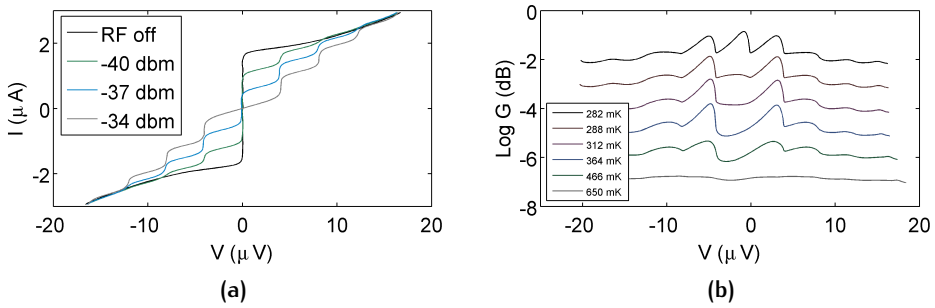

Figure 66: (a) IV curves as a function of the applied microwave field at the frequency of 2 GHz for the sample Bi_2Se_3X2S24 at the temperature of 280 mK. The appearance of Shapiro step at integer multiples of $\nu/\Phi_0 = 4.1\ \mu V$ can be observed. (b) Conductance curves as a function of the voltage for different temperatures. The position of the peaks correspond to the Shapiro step and it shows no dependence on the temperature, as expected in the case of the universal voltage-frequency relation (Eq. 77). Curves are shifted for clarity.

electrodes, characterized by a high critical field, was required to support a superconducting transport at high magnetic field.

When the junction is irradiated with the microwaves, in the absence of an external magnetic field, Shapiro steps at $V_n = \mu h/2e$ are observed, suggesting that the transport is mediated by Cooper pairs, with charge 2e. At high magnetic fields the height of the first Shapiro step is doubled to $\mu h/e$, compatibly with a super-current is carried by charge-e quasiparticles. This is a unique signature of the Majorana fermions, implying a 4π periodic CPR. The measured effect was the progressive suppression of $h/2e$ periodic Shapiro step for increasing values of the magnetic field.

In our case the use of Al electrodes only supported proximity effect in a weak magnetic field ($T < 100$ mT), we therefore could only verify the dominant 2π component of the current phase relation in a zero magnetic field.

Figure 67a shows the amplitude modulations of the two lowest Shapiro steps and of the critical current (i.e. 0^{th} Shapiro step), for the junction presented in Fig. 66a. Since our junctions are current biased, and their characteristic voltage $I_C R_N$ is much larger than the microwave frequency $\hbar\omega_{RF}/2e$ (nominally the dimention-less parameter $\eta = \hbar\omega_{RF}/2eI_C R_N$ is 0.22), we are in a regime where the modulation of the Shapiro steps does not follow the Bessel-like dependance on microwave amplitude. This is indeed valid for voltage biased JJs [157] (see Sec. 1.2.3).

The modulation of the lowest order steps was then numerically simulated using Eq. 17 [157]

$$\alpha_0 + \alpha_1 \sin(\eta\tau) = \frac{d\varphi}{d\tau} + \sin\varphi$$

The result of the simulation of our data is presented in the inset of Fig.67a. Data have been efficiently reproduced using a $\sin\varphi$ current phase relation, thus confirming the expected behavior in case of multimodal transport.

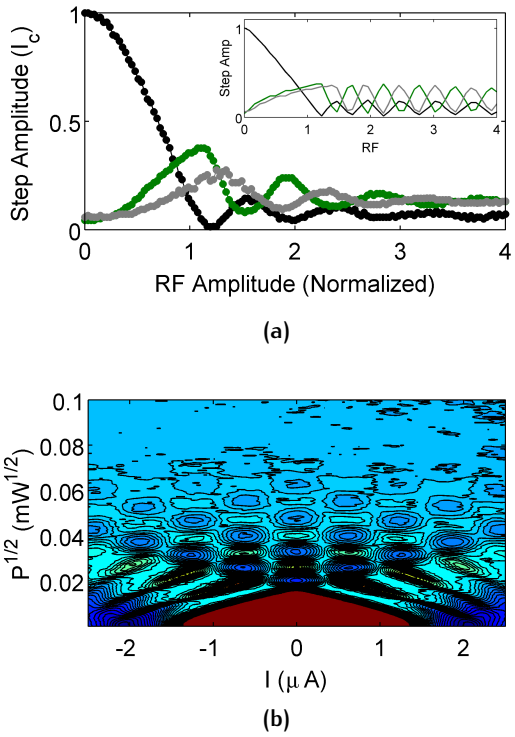

Figure 67: (a) Modulation of the critical current and of the first two Shapiro steps as a function of the applied microwave power (sample Bi_2Se_3X2S24). The curves shows typical modulations of Shapiro steps. (b) Conductance map of the same devices presented above as a function of the current and applied microwave power. The cyan spots correspond to the position of Shapiro steps. The characteristic pattern of the peaks in current and power is typical of Shapiro modulations.

The pattern of the Shapiro steps in current and microwave power can be summarized in a logarithmic conductance map (shown in Fig. 67b). The map presents a regular pattern of peaks and dips (corresponding to light and dark spots in the map). The distribution of these peaks reflects the 3D Bessel-like pattern of the Shapiro steps. The red part has an infinite conductance, and it represents the dissipation-less current

current flowing in the junction. Its edge corresponds to the critical current modulation shown in Fig. 67a.

5.4.2 Magnetic Field

We have measured the modulation of the critical current as a function of the external magnetic field in our $Al/Bi_2Se_3/Al$ devices. We have obtained conventional Fraunhofer patterns, as shown in Fig. 68a. As discussed in Sec. 1.2, a regular magnetic pattern imply a spatially uniform distribution of the current along the junction width, thus supporting the picture of a uniform barrier. Specifically we have verified the consistency of the geometrical area of the junction ($w \cdot (\lambda_L + d)$) with the value extracted from the fit of the period of the I_C modulations.

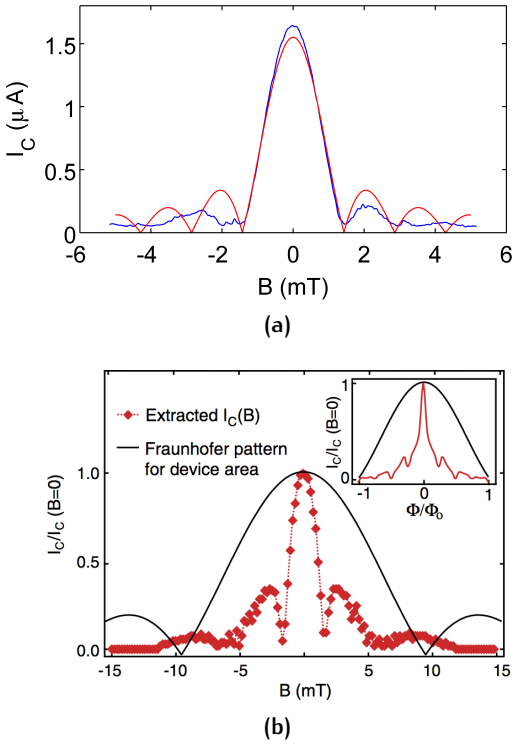

Figure 68: (a) Critical current as a function of an external magnetic field for the sample Bi_2Se_3X2S24. The red line is the expected Fraunhofer behavior, valid for a short junction. (b) Modulation of the critical current in an external magnetic field, for a $Al/Bi_2Se_3/Al$ coplanar junction. A reduction of the scale of the pattern and the nonuniform spacing are evident. (adapted from [191]).

This is important if one wants to evaluate the periodicity of the CPR [186]. As pointed out in a recent paper by Williams et al. [191], the presence of anomalies in the magnetic pattern could, in principle,

denounce the presence of Majorana fermions (see Fig. 68b). However, as the same Authors pointed out [162], similar effects could be due to the presence of Pearl vortices, typical of long Josephson junctions, making the interpretation of experimental data more difficult. Moreover, in coplanar junctions, the magnetic are of the junction could be larger than expected, as the London penetration length in the thin aluminum electrodes could be higher than their bulk value [44, 20]. A more efficient estimation of the periodicity of the current phase relation can be achieved using SQUID devices [183, 184].

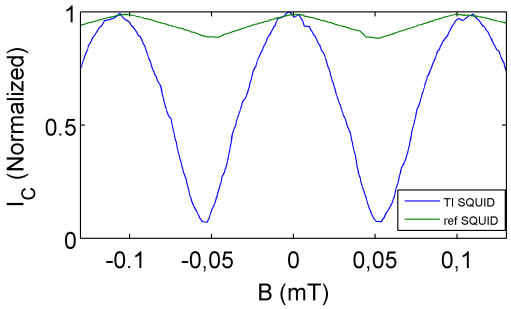

Figure 69: Critical current as a function of the magnetic field, in normalized units, for a S/Bi_2Se_3/S SQUID (sampleBi_2Se_3X3S1-1 - in blue). The modulation are compared with a reference device, having an identical loop, but the junctions replaced by Al nano-bridges (in green). The two modulations present identical period. The difference of the amplitude of the modulation is a well know effect related to the different self inductance of the SQUIDs [141].

Figure 69 shows the modulation of dc SQUIDs with different geometry (sample Bi_2Se_3X3S24-1-3). The period of the oscillations corresponds to a loop area of 19 μm², whereas the designed area was 9.6 μm². This discrepancy is coming from a flux focussing effect [155] due to the geometry of the SQUID and of the electrodes, as confirmed by a comparison of the period of the SQUID oscillations with that of Al reference SQUID, realized on the same chip (also shown in Fig. 69). The optical images of the devices are shown in Fig. 70. The two Al/Bi_2Se_3 SQUIDs and the reference devices show the same modulation period, which supports the existence of a conventional CPR, independently from the geometry of the device.

5.5 CONCLUSIONS

The body of our results confirms, for the first time also for Al/Bi_2Se_3/Al junctions, the dominant role of two dimensional surface states to carry

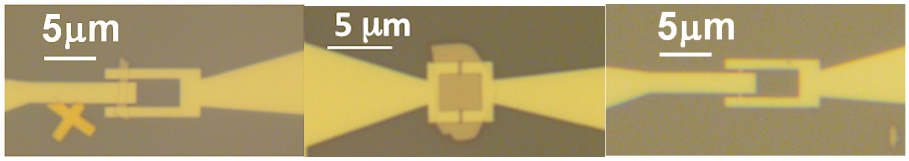

(a) SQUD with S-TI-S junctions **(b)** On-flake SQUD with S-TI-S junctions **(c)** reference SQUID with Al nanobridges

Figure 70: The three devices have an identical loop of 9.6 μm^2. Device in (a) and (b) have coplanar $Al/Bi_2Se_3/Al$ junction, while device in (c) the $Al/Bi_2Se_3/Al$ junctions are replaced by Al nano bridges, which are topologically trivial. (a) and (b) have different geometry of the loops. The three devices have identical magnetic period of the I_C modulations (see Fig.69).

super-current, which can be considered to some extent universal. Bi_2Se_3 crystals, which are produced in quite different conditions and whose surfaces are treated in quite different manners [71], behave as ballistic barriers independently of the exact interface with the superconducting electrodes, as confirmed by the temperature dependence of the critical current. The ballistic transport supports the scenario of a super-current carried by the topologically protected surface states of the TI.

A comparative study of the behavior of the IV curves with the effect of an external magnetic field, and of a microwave field confirmed the presence of a conventional Josephson coupling, with a topologically trivial current phase relation, as expected in the case of multichannel transport.

6 ESCAPE DYNAMICS IN HYBRID JOSEPHSON DEVICES

In this Chapter I will present a comparative study of switching current distributions (SCD) in superconducting hybrid junctions. This is a standard tools to investigate phase dynamics [54, 123, 43, 68, 59, 122]. From the analysis of SCD histograms, indications on the transition to macroscopic quantum tunneling from thermal activation can be inferred.

The interest of this study lies in the recent introduction of Josephson devices with semiconducting barrier, or in combination with nanowires, or flakes of topological insulators in coplanar geometries. These devices show lower values of critical current and capacitance, when compared to the standard tunnel devices, which typically falls in the moderate damping regime.

Therefore this work was motivated by the need of a better understanding of coherence and dissipation in moderate damping, to which we tried to contribute unifying the various results achieved on NbN junctions (Sec. 6.5) and on YBCO bi-epitaxial junctions (see Sec. 6.4) with the results of numerical simulations (see Sec. 6.3). The outcomes of this work were also compared with data available in literature, in the attempt to condensate the various regimes in a (Q - E_J/k_BT) phase diagram. This was an unavoidable step for a complete comprehension of the dynamics of hybrid Al/Bi_2Se_3/Al coplanar devices presented below.

6.1 SWITCHING CURRENT DISTRIBUTIONS

We have performed a study of the SCDs in superconducting hybrid junctions. In devices with underdamped dynamics the IV characteristics typically shows an hysteresis. These devices are characterized by stochastic switchings from the superconducting to the resistive state. This switching corresponds to a bi-stability of the phase particle in the tilted washboard potential (Eq. 32) [165, 131, 93], describing the dynamics of the system (as described in Sec. 1.5.2). An estimation of the relevant physical quantities can be also achieved, including the dissipation level of the device, well described by the damping parameter Q and by the shunting impedance of the circuit [14, 113].

The moderate damping regime is typical of nano-structured and hybrid devices. Indeed the typical low critical current density nano-channels barrier, together with values of capacitance significantly lower than the more standard tunneling junctions, imply lower values of the damping parameter

$$Q(I) = \omega_p(I)RC \tag{78}$$

Moderate damping typically falls in the regime $1 < Q < 5$, which can be controllably induced in larger junctions in case of low critical current densities in junctions with larger intrinsic dissipation levels, as occurring in HTS systems [104, 117].

This regime is rather unexplored, and the determination of the switching dynamics requires an accurate determination of the junction parameter, through the use of numerical Monte Carlo simulations.

The measurements discussed here have been obtained using a dilution cryostat. Measurements were performed in a four probe configuration. A current ramp was used to bias the junction. when the bias current approaches I_C, the voltage shows a sudden jump to a finite value see Fig. 71a. More details on the measurement setup are given in Sec. 3.2.4.

6.2 ESCAPE DYNAMICS IN NIOBIUM NITRIDE JOSEPHSON JUNCTIONS

In this introductory paragraph we want to describe the standard phenomenology of the escape dynamics. We will show results from NbN tunnel junction with MgO barriers [115, 116]. These junctions fall in the moderately damped regime which is very interesting as comparative study for hybrid devices. A complete description of these features goes beyond the purposes of this work [125].

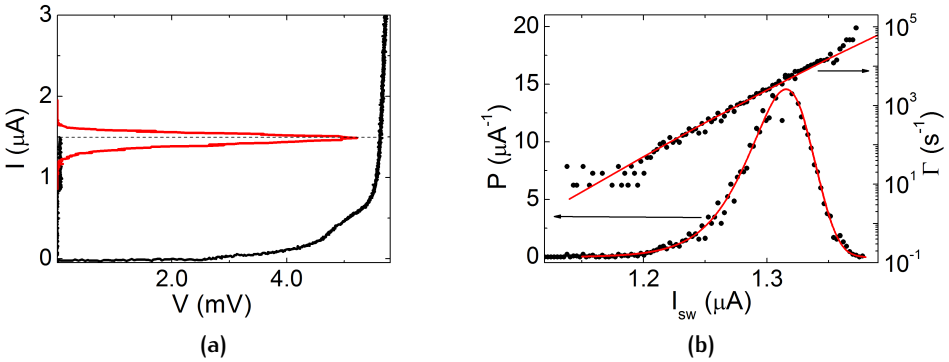

Figure 71: (a) IV curve of a NbN Josephson junction at the temperature of 90 mK. The IV curves have an under-damped typical feature, with an hysteresis and a stochastic switch from the superconducting to the resistive state. The curve in red shows the corresponding SCD. (b) SCD of the same NbN Josephson junction with a best fit line. The corresponding experimental switching rate was achieved using Eq. 40. The Rate was fitted using Eq. 39.

We report measurements of SCDs, performed at the current rate of 122 μA/s in the temperature range of 20 mK - 2.4 K. The main experimental signature is the switching current distribution, extracted from the threshold, through a direct or indirect measurement of the switching current.

Raw data have been analyzed, and an estimation of the escape rates was extracted [68] using Eq. 40

$$\Gamma(I) = \frac{\gamma P(I)}{1 - \int_0^I P(i)di}$$

where $P(I)$ is the probability of the switching, experimentally extracted from the SCD and γ is the ramp rate. Figure 71b shows the SCD and the corresponding escape rate.

The behavior of the SCD as a function of the temperature, shown in Fig. 72, is the real fingerprint of the phase dynamics. As discussed in Sec. 1.5.2, when the junction is the quantum regime, the histograms overlap [172, 123, 54], therefore the mean value (I_{sw}) and the width (σ, or w) of the distribution do not depend on the temperature (see Fig. 73). In this regime the escape dynamics is completely temperature independent, since the escape rates are dominated by the quantum contribution Γ_q determined by the plasma frequency (see Eq. 38). Negligible contribution, indeed, are given by the thermal escapes rates Γ_T (Eq. 36), which is in fact suppressed at low temperatures. Moreover, the mean switching current at the lowest temperatures is usually

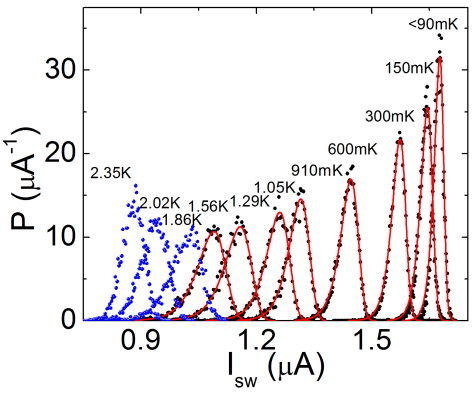

Figure 72: Switching current as a function of the temperature for the NbN junction. The black curves are the experimental data corresponding to the MQT - TA regime, with the best fit line shown in red. The blue curves corresponds to the PD regime, which cannot be fitted with an analytical model.

constant, due to a saturation of the $I_C(T)$, observed for most junctions (see. Eq. 20).

In TA regime the histograms progressively broadens when increasing the temperature. This corresponds to an increase of the width, following the scaling behavior $\sigma \propto T^{2/3}$. The mean switching current, instead, progressively decreases. This behavior is the result of two different mechanisms: on the one hand the switching is more likely to happen at lower currents when the temperature is increased, as the thermal activation energy enhances the escape rate (Eq. 36). On the other hand the absolute value of the critical current progressively decreases, following the behavior determined by the $I_C(T)$ curve (see Sec. 1.3).

The crossover temperature T_{cr} between the quantum and thermal regime is experimentally detected by a crossover from a constant σ to a $\sigma(T)$ with a positive slope ($d\sigma/dT > 0$), as shown Fig 73a.

In MQT and TA regime the escape rate and the SCD can be fitted using the model (Eq.39)

$$\Gamma(I) = \frac{\omega_p}{2\pi} e^{-\frac{\Delta U}{k_B T_{esc}}} \left(\Gamma_{0q} + \Gamma_{0T}\right)$$

The results of the fit have been shown in Fig. 72, for data below 1.6 K. Above this temperature, the behavior of the SCD cannot be described in terms of this model, and the effects of multiple escape and re-trapping processes have to be quantitatively considered, as described in Sec. 1.5.3.

In moderately damped junctions (with $1 < Q < 5$), a transition from TA to PD regime occurs [93, 124, 59] at a crossover temperature T^*, which marks a distinctive change in the sign of the temperature derivative of σ, with $d\sigma/dT > 0$ for $T < T^*$ and $d\sigma/dT < 0$ for $T > T^*$.

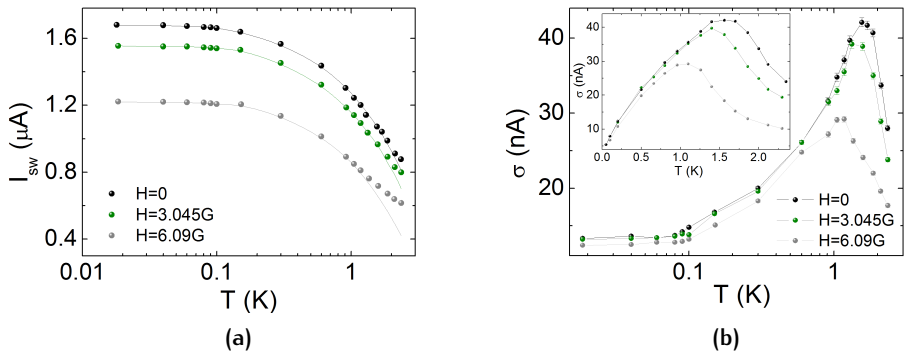

Figure 73: (a) Mean switching current extracted from the SCDs as a function of the temperature for different values of the magnetic field. (b) Width of the SCDs as a function of the temperature (in a log scale). The three different regimes (MQT, TA, PD can be clearly identified). The inset shows a magnification of the TA - PD crossover in a linear scale.

The reduction of the σ above T^* can be qualitatively related to the interplay between escape and re-trapping events, which also determines a progressive symmetrization of the SCD for an increasing temperature [115, 122].

The transition is also visible in the shape of the switching histogram, which becomes more and more symmetric as approaching towards the PD regime. The skewness γ (defined as the third momentum of the distribution, divided by σ^3) is a measurement of the level of asymmetry of the SCD. At low temperatures a value of $\gamma = -1$ corresponds to a SCD lying in the quantum or thermal regime. As the temperature increases the distributions become more and more symmetric as approaching towards the PD regime. Correspondingly γ goes to zero.

The effect of the symmetrization of the SCD can be also traced in the shape of the escape rates, which deviates from the exponential behavior. The experimental escape rates is suppressed at the lower values of the bias current, at which the effect of the re-trapping is more pronounced. Figure 74b shows the experimental escape rates as a function of the height of the potential energy (see Eq. 37)

$$\Delta U = E_J \left(\sqrt{1 - \frac{I}{I_C}} - \cos^{-1}\left(\frac{I}{I_C}\right) \right)$$

As the temperature is increased above T^*, the rates appear more and more rounded, on a logarithmic scale. The rounded shape is signaling a deviation from the exponential behavior, more pronounced at the highest value of $\Delta U/k_B T$, corresponding to the lower currents.

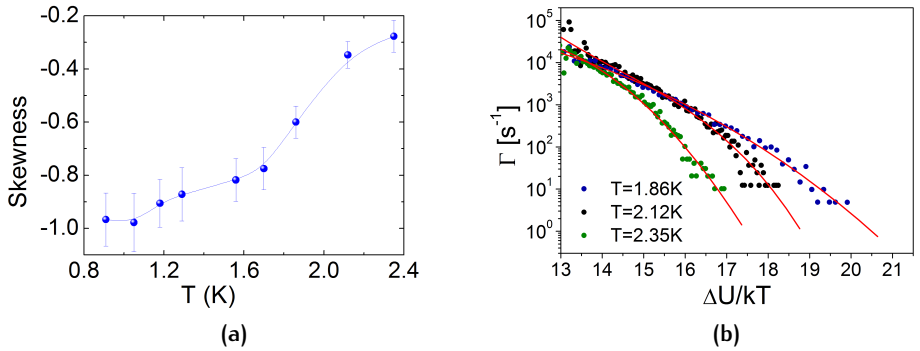

Figure 74: (a) Skewness of the SCDs as a function of the temperature. The plot shows a progressive symmetrization of the SCDs in the PD regime. The progressive symmetrization of the SCDs is also signaled in the Escape rates, shown in panel (b) as a function of the potential energy $\Delta U/k_B T$. The curves shows a bending, more pronounced at higher values of $\Delta U/k_B T$, corresponding to the lower values of the bias current.

6.3 MODERATELY DAMPED REGIME AND MONTE CARLO SIMULATIONS

Monte Carlo simulations are a very useful tool to achieve a quantitative description of SCD in the moderate damping regime [59]. In fact, while the behavior of the width (w) of the switching histograms in the thermal activation regime follows the universal scaling behavior $w \propto T^{2/3}$, the scaling behavior of the w in phase diffusion (PD) regime is not analytically reproducible, since it is determined by two combined stochastic events. On the one hand the event of the escape from the local minimum of the washboard potential (see Sec. 1.5.3 for details), on the other hand the probability (once escaped) to be re-trapped in one of the following minima.

We have used a noise-affected Runge-Kutta algorithm to recreate the dynamics of the RCSJ model. The noise was generated by the RANLUX random numbers generator of the FORTRUN Cern library. The algorithm was run on a grid of parallel batch of processors (available at CINECA). Each batch simulates the switching distribution at a given temperature. Simulated data have then been analyzed with the same routine in use for real data, and the $w(T)$ curve has been extrapolated.

Figure 75 shows some $w(T)$ curves, simulated with different values of the Q. A fundamental information is given by the simulated value of the crossover temperature T^* as a function of damping factor (shown in the inset of Fig.75). The simulations presented here are referred to a

junction with a critical current of 1.2 μA, typical of the moderate damping regime. Nevertheless these data are of general validity since, the behavior for different values of the I_C can be obtained by simply rescaling the temperatures.

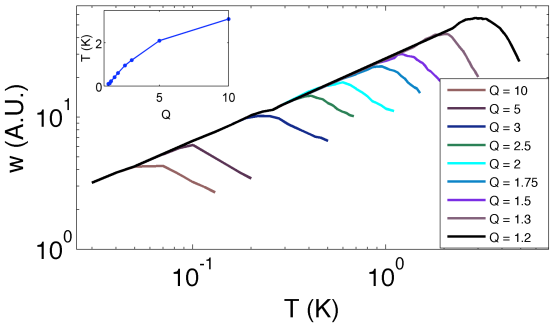

Figure 75: Monte Carlo simulations of the width of a switching current distribution as a function of the temperature, for different values of the damping factor. The critical current used in this case is 1.2 μA. The inset shows the modulation of the crossover temperature as a function of Q.

An additional feature is given by the behavior of the curve in the PD regime. In fact the collapse of the $w(T)$ curve in phase diffusion is not universal, but it is determined by the damping. Particularly, the critical exponent γ can be inferred from a log log plot

6.3.1 Q - $k_B T/E_J$ Phase Diagram

The results achieved through MC simulations are of general validity. In fact the dynamics is determined by the damping factor Q, which is a universal dimensionless parameter. The other element that determines the dynamics is the thermal activation energy ($k_B T$). This have been is normalized to the height of the potential barrier (E_J) (see Eq. 36, 41 and Ref. [74, 68, 59, 122]), to obtain a second universal and dimensionless parameter. This can be condensed in a (Q, $k_B T/E_J$) phase diagram [117, 127, 172], which summarizes the various activation regimes. This has been already expressed in the form of a phase diagram by Kivioja et al. [97] (see Fig.76b) who have shown that by spanning the (E_J, $k_B T$) parameter space it is possible to engineer all different regimes ranging from phase diffusion and thermal activation to macroscopic quantum tunneling.

The good agreement between experimental data, which refer to various works reported in the literature, and the simulations is highlighted by Fig. 76a, where the experimental crossover temperatures are put on top of the numerically estimated transition curve. This makes

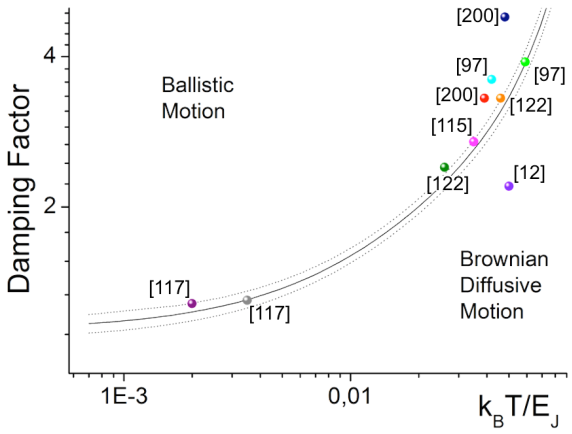

(a)

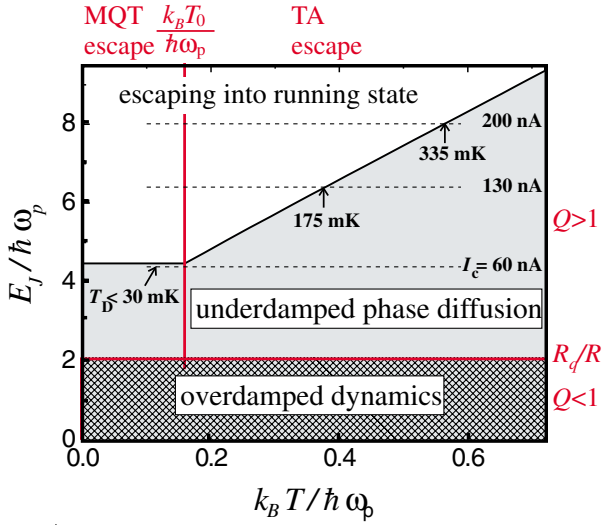

(b)

Figure 76: (a) Phase diagram of TA vs PD dynamics, the figure shows the Q vs $k_B T/E_J$ transition curve between TA and PD regime, determined by the MC simulations. The dashed sidebands are the error bars, determined by the finite temperature step used in the simulation. The various points are referred to experimental phase transition points available for various junctions in literature ([117, 122, 115, 97, 200, 12]) (with the exemption of the work by Bae et al. [12], where a PD behavior in the whole temperature range was found, as confirmed by the phase diagram). Junctions of Ref. [117] is the YBCO bi-epitaxial junctions presented in Sec. 6.4, Junctions of Ref. [115] is the NbN junction presented in Sec. 6.2. (b) (E_J, $k_B T$) phase diagram proposed by Kivioja et al. [97].

this phase diagram a valid guideline in order to define the relation between E_J, the turnover temperature T^* and the junction quality factor Q. In addition it indicates how the transition from TA to PD regime can be tuned by the critical current and the shunting capacitance of the junction.

The pioneering studies of Kautz and Martinis [93, 124] and Iansiti [87, 88] on small junctions can be now supported and developed by different types of junction of quite different sizes. These devices are characterized by intermediate levels of dissipation and by low critical current density J_C limit, characteristic also of nano-hybrids devices [172, 129].

In this general scenario, YBCO grain boundary junctions, presented in the next paragraph (Sec. 6.4), are a an ideal play ground to engineer devices with different parameters, thanks to the flexibility of the bi-epitaxial fabrication technique. It facts it is relatively easy, for HTS junctions, to meet the requirements to contribute to new regimes of the (Q, $k_B T/E_J$) phase diagram [117, 128, 126]. This is the case, for instance, of junctions fabricated on substrates that reduces the values of the stray capacitance.

These device combines a moderately-high damping $Q \gtrsim 1$ with a relatively high Josephson energy, thus meeting the requirement $T^* < T_{cr}$ to detect a direct transition from MQT to phase diffusion [117]. This regime can be achieved by engineering junctions with lower critical current and junction capacitance [104, 200, 199, 117, 125]. An example is given by a experiment presented in a paper by Yu et al. [200] on sub-micron $Nb/AlO_x/Nb$ junctions. Data show an anomalous $w(T)$ dependence with a negative dw/dT over the entire temperature range. Another example is given by the paper by Krasnov et al. [104], in this paper the Authors use shunt capacitance to tune the crossover temperature.

6.3.2 Frequency Dependent Damping

As discussed above there are two main features that are tuned by the damping factor: the turnover temperature T^* and the critical exponent γ. Apparently the two effects can be disentangled in the framework of a more complex model, which takes into account the effects of the frequency on the effective damping (see Sec. 1.5.3). The main effect of a frequency dependent damping (presented in Sec. 1.5.2) can be properly described by using a simplified scheme with two characteristic damping parameters [93]. One which is the effective damping at the plasma frequency ω_p of the junction, which is called high frequency damping factor (Q_H), and one which is the effective damping at the quasi d.c. bias frequency of the bias ramp ($1 - 100$ Hz). While Q_L is substantially

determined by the sub-gap resistance of the junction, Q_H which is mainly determined by the circuit.

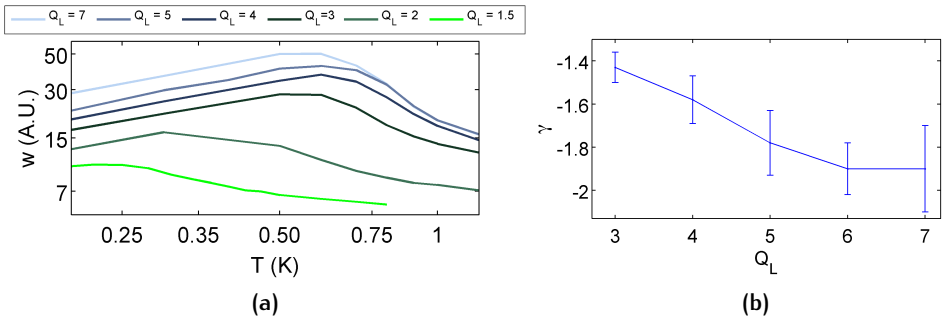

Figure 77: (a) Monte Carlo simulations of the width of the SCD vs temperature in a frequency dependent damping model. In this plot the high frequency damping has been kept constant at $Q_H = 1.5$, while Q_L is varied. The curve in the descendent part (corresponding to PD) shows a clear trend towards lower slopes at low values of Q_L. The crossover temperature shows a weak dependence on Q_L. (b) Critical exponent γ as a function of the low frequency damping Q_L.

The body of the result presented below is that while T^* is mainly determined by the high frequency damping Q_H, the critical exponent is significantly affected by the intrinsic shunting of the junction (determined by the low frequency damping Q_L) in some circumstances.

With the same algorithm used for the simulations presented above we have produced two more datasets. One was performed by keeping the Q_H at the value of 1.5, while Q_L was changed, in the other one Q_H was varied and Q_L was fixed at the value of 5. The frequency independent damping, presented above, in fact, have been achieved in the approximation $Q_H = Q_L = Q$.

Figure 77a shows the $w(T)$ curves in the case of a constant Q_H. The critical exponent shows a significant dependence on Q_L (as shown in Fig. 77b) when Q_L is reduced, and saturates when Q_L is high ($Q_L > 5$). The indication of the MC simulation is that in the regime $Q_H \lesssim Q_L$, when both high and low frequency damping falls in the moderately damped regime, some unconventional features can be observed, namely the critical exponent γ of the $w(T)$ curve. When instead Q_L is high, the curve is determined only by the circuit, as in the well established framework of Fenton and Warburton [59].

However, the crossover temperature is in no case significantly affected by Q_L. This can be observed in Fig. 78, where a comparable modulation of T^* can be observed in curves with the same value of Q_H (the figure shows the curve for $Q_H = Q_L$ and for $Q_L = 5$), independently on the

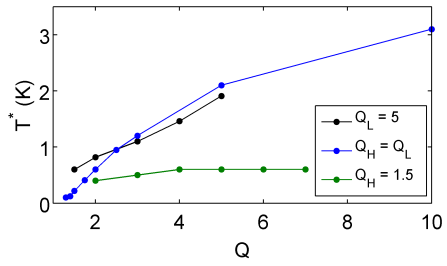

Figure 78: Crossover temperature vs damping factor for three set of simulations with different values of Q_H and Q_L. Specifically data plotted in black was simulated using a constant $Q_L = 5$, and Q_H is changed. Its behavior is quite close to data plotted in blue (see Fig.75), where a frequency independent damping was used (i.e. $Q_L = Q_H$). Data plotted in green shows a significantly different behavior. They corresponds to a $Q_H = 1.5$ and Q_L is varied (see Fig. 77a). In this case the crossover temperature is almost independent of Q.

value of Q_L. Only negligible variations of T^*, instead, are determined by a the variation of Q_L (green curve in Fig. 78, also shown in Fig. 77).

6.4 MODERATE DAMPING IN YBCO BI-EPITAXIAL JUNCTIONS

Looking at recent literature, HTS systems have represented the start for SCD measurements on systems different from LTS junctions [17, 16, 104]. Some of the more recent advances in the field of HTS Josephson devices have been pushed by advances in nanotechnology. Moreover off axis grain boundary (GB) junctions, fabricated on substrate with low capacitance [169] fall in the typical moderately damped regime that can be encountered in nano-scale junctions [173, 129]. Therefore YBCO bi-epitaxial grain boundary junctions are a fantastic test branch for the study of switching dynamics, thanks to their design scalability and flexibility in controlling the level of damping [117, 126, 127].

We demontrate a direct transition from macroscopic quantum tunneling to phase diffusion, thus exploring a new region of the phase diagram presented in Sec. 6.3.1 (see Fig. 76a).

We have used YBaCuO off-axis grain boundary bi-epitaxial JJs [114, 171, 17, 16, 169], whose scheme is shown in Fig. 79. The GB is determined at the boundary between the (1 0 3) oriented grains growing on the bare substrate and the (0 0 1) grains growing on the CeO_2 seed layer. Figure 79b shows a SEM image of an extended grain boundary.

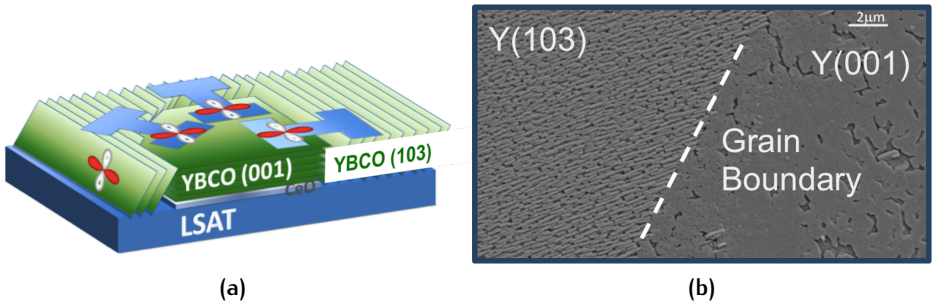

Figure 79: (a) Sketch of a bi-epitaxial grain boundary Josephson junction. Junctions was fabricated using a LSAT substrate (in blue) and a CeO_2 seed layer (in grey). The green plane represents the CuO_2 transport plane on the YBCO, presenting the characteristic off axis orientation on the LSAT substrate. The orientation of the d-wave order parameter in the two configuration is also shown. The blue structures presents the geometry of the junctions in different angles of the grain boundary (30°, 90°, 0° respectively, from left to right). (b) Scanning electron microscopy of a grain boundary, corresponding to the meeting of the (1 0 3) with the (0 0 1) grains. The image was performed on a LSAT/CeO_2 structure, prior to the lithography of the YBCO structures.

We have engineered junctions on $(La_{0.3}Sr_{0.7})(Al_{0.65}Ta_{0.35})O_3$ (LSAT) rather than on $SrTiO_3$ (STO) substrates, where MQT in a high temperature superconductor JJ was first demonstrated [17, 16]. The new design fully responds to the need of reducing stray capacitances. Specific capacitances are one order of magnitude lower than those measured on STO-based devices. Dynamical junction parameters can be tuned by choosing the interface orientation indicated by the angle (see Fig. 79a), which also sets d-wave induced effects.

The IV curves of these devices, shown in Fig. 80, gave evidence of a pronounced hysteresis (50%) and a critical current of 1.2 μA.

On these junctions we have studied the switching dynamics in a temperature range between 20 mK and 2.2 K. We have substantially engineered a device with $T^* \lesssim T_{cr}$ [117].

We report measurements of SCD in a temperature range from 20 mK to 2.2 K, performed with a sweep rate of $dI/dt = 17.5\ \mu A/s$. These measurements, collected over a wide range of temperatures, are reported in Fig. 81. Our data are characterized by two distinct regimes. A progressive broadening of the histograms occurs when lowering the temperature, which is a distinctive feature of the PD regime [122, 115, 104, 12]. For temperatures below about 135 mK the histograms overlap, following the typical MQT behavior [54, 123, 43]. This is a typical signature of a quantum activation regime.

Figure 81b shows the width of the SCDs as a function of the temperature, with a direct transition from a constant regime, to a

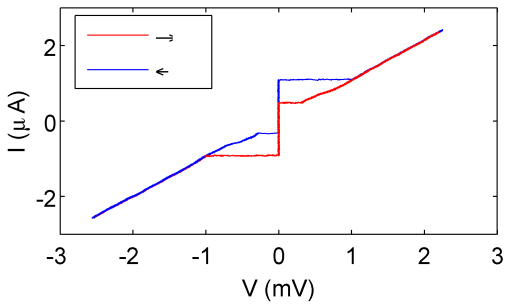

Figure 80: IV curve of junction YBCO16a. The red and blue part corresponds to the different direction of the current bias. The IV shows an hysteresis, typical of under-damped junctions. Around I_C the voltage shows a sudden jump to a voltage of 1 mV.

decreasing regime. This corresponds to a direct transition from a regime where the escape is dominated by macroscopic quantum tunneling, to the phase diffusion regime. The inset shows the corresponding mean switching current I_{sw} and the I_C, extracted form the model (see Sec. 6.5). For temperatures T well below T_{cr}, MQT contributions to escape rates are larger than those coming from both thermal escape and multiple re-trapping processes. MQT processes are substantially followed and assisted by thermally ruled re-trapping processes. However, a fully quantum account of phase fluctuations passes through the empirical condition of a Josephson energy much larger than Coulomb energy, $E_J \ll E_C$ with $E_C = e^2/2C$, given by Iansiti et al. [87].

Above 135 mK the negative temperature derivative of w is consistent with the phase diffusion regime, due to the multiple escapes and re-trapping in the potential wells. This regime has been fitted using MC simulations (shown in Sec. 6.3) with a damping factor $Q = 1.3$ (see Fig. 81b).

HTS junctions lead to new insights on intermediate regimes of dissipation, which are of relevance also for hybrid devices. Junctions, fabricated on low loss LSAT substrate, were characterized by a combination of a low Q factor to a relatively high critical current (1.1 μA), thanks to the reduced stray capacitance of the substrate. These junctions are engineered to explore a new region of the phase diagram, made available by the different ranges of Q and I_C.

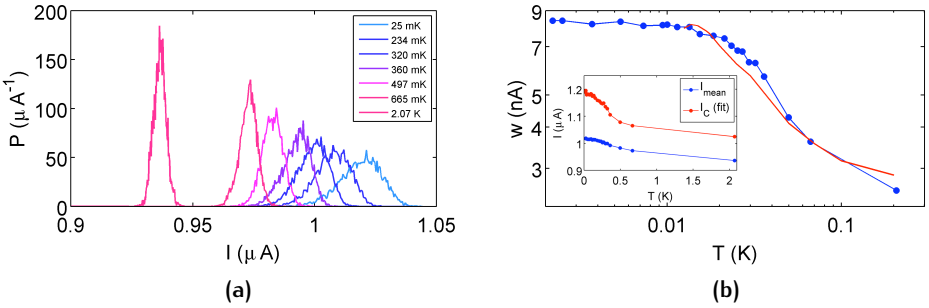

Figure 81: (a) Switching current distributions shown for various temperatures for junctions YBCO16a. Below 135 mK the SCDs overlap. Above this temperature measurements shows progressive broadening of the histograms, giving evidence of a direct transition towards a phase diffusion regime. (b) The width of the SCDs shown in Fig. 81a is reported as a function of the temperature, giving evidence of the direct MQT-PD transition. This corresponds to the crossover from a constant w to a negative dw/dT slope. The red solid line is the result of simulations in the diffusive regime with a damping parameter of $Q = 1.3$. The inset shows the mean switching current of the histogram and I_C, extracted form a fitting procedure of the SCDs.

6.5 PHASE DYNAMICS IN BISMUTH TELLURIDE BARRIERS

The results presented here are referred to $Al/Bi_2Te_3/Al$ junctions. Coplanar hybrid devices have been produced through a procedure similar to the $Al/Bi_2Se_3/Al$ fabrication presented in Sec. 3.3.1. The main difference is the technique used for the fabrication of the TI. In the case Bi_2Te_3 thin films have been produced by molecular beam epitaxy (MBE) deposition [67, 163]. The junctions showed an over-damped I-V curves, with hysteresis clearly visible up to 300 mK.

The body of our results is based on the study of the switching current distributions, and contains a careful characterization of coherence and dissipation in this kind of devices performed, for the first time to our knowledge, on coplanar hybrid devices with TI barriers. The estimation of all the junctions parameters includes an estimation of the Q factors and of plasma frequency ω_p, based on the results of the simulations presented in Sec. 6.3. A careful characterization of the proximity effect has been also performed, including a study of the critical current as a function of the temperature.

As shown for the over-damped $Al/Bi_2Se_3/Al$ junctions presented in Sec. 5.2, 5.3, also in these moderately damped junctions, we have measured IV as a function of the temperature, with the same indication of a predominant ballistic transport regime. We also measured the IV

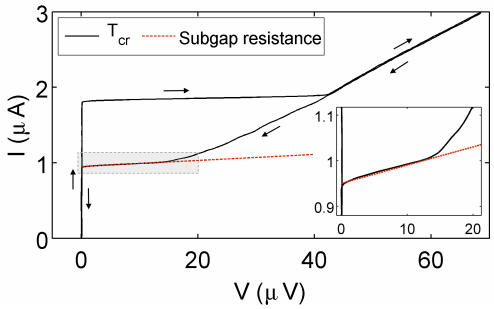

Figure 82: IV curve of the junction at the temperature of 75 mK of a $Al/Bi_2Te_3/Al$ device. The curve shows a sub-gap resistance of 250 Ω, as depticed by the red dashed line. The black arrows underlines the direction of the bias ramp. The shaded part is shown in inset with a higher magnification.

curves in magnetic field and in a microwaves field, to fully characterize the features of the conventional Josephson coupling, following a similar framework to the characterization presented in Sec. 5.4

6.5.1 Proximity Effect in Al-Bi_2Te_3-Al junctions

Figure 82 shows a typical current - voltage curve with a hysteresis of 50% of the I_C value. The value of the I_C for this device is 1.94 μV at 20 mK and the normal resistance is 24 Ω. The switching voltage of the junction is 40 μV. In the sub-gap branch, the IV follows a rather linear behavior until 18 μV. Below this value the resistance goes up to values of roughly 250 Ω. This value, called sub-gap resistance, is of fundamental importance for the switching dynamics [93].

A careful characterization of the junction properties has been performed, including the measurement of the modulation of the critical current as a function of an external magnetic field (presented in Fig. 83a), that follows the expected Fraunhofer patterns. The magnetic area, estimated from the period the modulations is 1.15 μm^2, in a reasonable agreement with the geometric area of the device, taking into consideration the flux focussing effects [155] already discussed in Sec. 5.4.

Figure 83b shows the Shapiro steps, measured at 20 mK with a frequency of 5 GHz. The position of the steps, and their modulation is in agreement with a conventional Josephson relation. Anomalies in the Shapiro steps have been detected above 10 GHz, and their study is still a work in progress. Some preliminary results are presented below (see Fig. 85, 86).

Figure 84 shows the IV curves as a function of the temperature. Devices showed a much lower transparency than the $Al/Bi_2Se_3/Al$

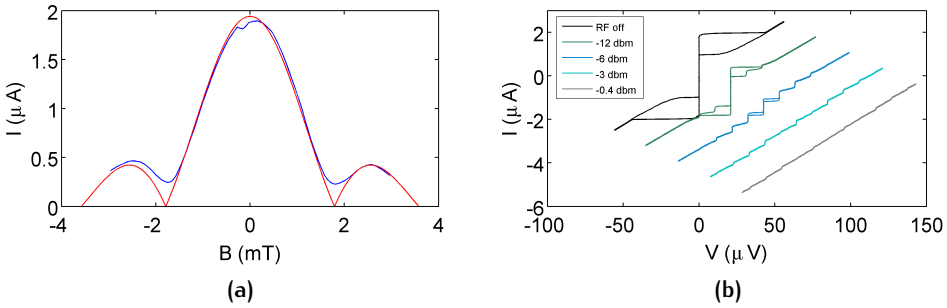

Figure 83: (a) Critical current as a function of an external magnetic field (sample Bi_2Te_3R708B). The red line is the best fit curve for the expected Fraunhofer behavior. (b) IV curves for various applied power of the microwave field at the frequency of 5 GHz, and at the temperature of 18 mK. The curves shows the appearance of Shapiro steps at multiple integers of 10.5 μV. Curves are shifted for clarity.

junctions described in Sec. 5.1 (D = (0.41 ± 0.05)), with pronounced hysteresis up to 300 mK.

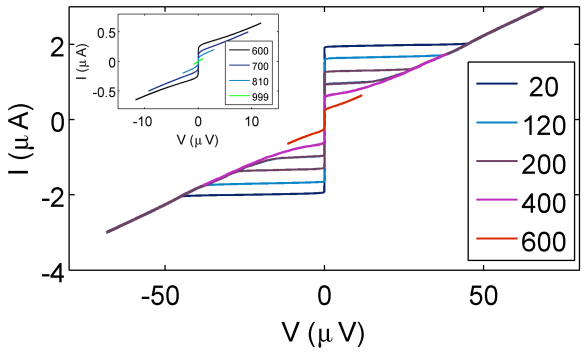

Figure 84: IV curves as a function of the temperature. Curves show a pronounced hysteresis up to 300 mK, due to to the high capacitance of the devices. The inset shows curves at higher temperatures, in higher magnification scale

Half Integer Shapiro Steps

We detected Shapiro steps at semi-integer position of the conventional voltage - frequency relation (Eq. 77), for frequencies of 10 GHz and 20 GHz. Our results are shown in Fig. 85, where Shapiro steps are visible at multiple integers of $V = \nu h/4e$ of the current - voltage characteristic. These results were confirmed on two different devices, and the appearance of half integer steps was confirmed at the same frequencies of the microwave field. A non-equilibrium dynamical model, based on time-dependent Andreev bound states, is traditionally

reported in literature [111, 56] to accounts for the appearance of half integer Shapiro step and for an enhancement in the conductance near zero bias. By irradiating the junction with microwaves at a frequency ν, the n^{th} harmonic of the CPR (Eq. 1) can create phase-locking resonance at voltages $2ne V/h$, generally called fractional Shapiro steps.

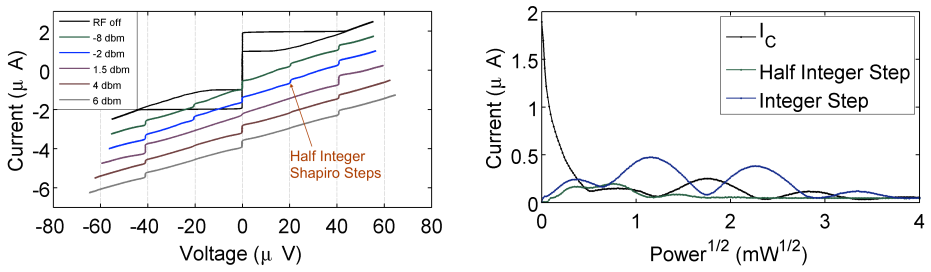

Figure 85: (a) IV curves of junction Bi_2Te_3R708B at the temperature of 20 mK for an increasing microwave field at the frequency of 20 GHz. The curves shows the appearance of Shapiro steps at voltages of $\nu h/4e$, corresponding to a value of 20.5 μV. The half integer steps disappear at lower powers of the microwave field, compared to the regular Shapiro steps. (b) The modulation of the critical current, and of the first integer and half integer Shapiro steps. The modulation of the half integer step are more irregular, and disappear at lower values of the RF power.

6.5.2 Ballistic transport in Bi_2Te_3 barriers

A fitting procedure of the $I_C(T)$ curve has been performed, in analogy of what described in Sec. 5.3. We have a clear evidence of a ballistic transport regime (see Fig. 87). The fit of the analytical model was performed above the temperature of 160 mK. We obtain a comparable value of the Thouless energy (97 μeV) to the value obtained for Bi_2Se_3 samples. In Bi_2Te_3 the Fermi velocity is known to be smaller than in Bi_2Se_3 ($v_F \simeq 1 \cdot 10^5$ m/s). Therefore a significantly shorter coherence length was extracted ($\xi_n^{Bi_2Te_3} = 700$ nm, $\xi_n^{Bi_2Se_3} = 3$ μm). In devices fabricated on Bi_2Te_3 thin films devices with a separation between the electrodes of $L = 200$ nm were produced.

A numerical simulation of our data has been performed using Eq. 28, using a value of transparency of $D = 4$, in agreement with the experimental value extracted from the IV curve. The value of Fermi velocity extracted from the simulation is $(1.8 \cdot 10^5$ m/s). This value is in fair agreement with data available in literature [185]. The result of the numerical simulation is shown in Fig. 87, confirming the hypothesis of ballistic superconducting transport.

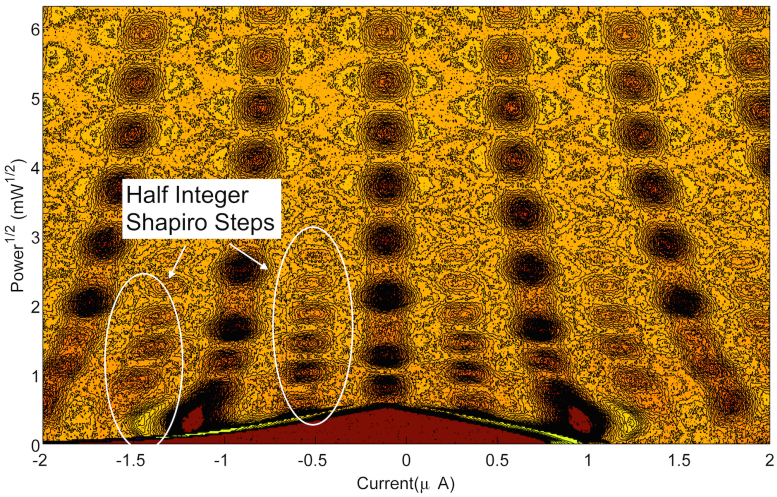

Figure 86: Conductance map of the junction Bi_2Te_3R708B, at the frequency of 10 GHz and the temperature of 20 mK. The map is analog to the one presented in Fig. 67b, for Bi_2Se_3 junctions. In this case additional peaks can be seen, corresponding to the position of half integer Shapiro steps, as signaled by the white spots.

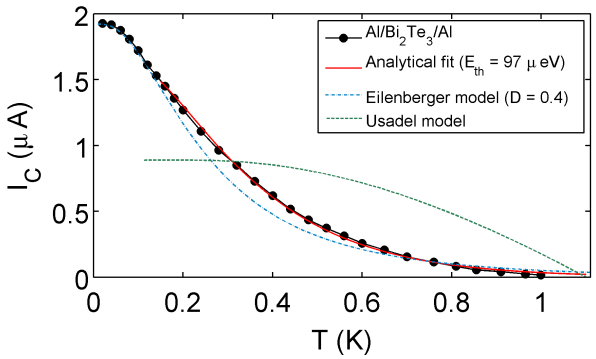

Figure 87: I_C vs T curve extracted from Fig. 84. The red line is the best fit line from the analytical model (Eq. 75), while the green curve is the result of a numerical simulation of the Eilenberger model (Eq. 28)

6.5.3 Switching Current Distributions in $S/Bi_2Te_3/S$ junctions

We have measured the switching current distributions (SCD) as a function of the temperature. We measured two different devices (sample Bi_2Te_3R708B), basically confirming the same results. The junctions were biased with a fast current ramp ($\gamma = 2.3$ mA/s). A clock is used to measure the time taken from the start of the current ramp to the switching event. This is called the time of flight (TOF). This technique to evaluate the switching current is basically equivalent to the one described in Sec. 6.2, 6.4, with the main difference that in this case the current is not directly measured, but indirectly obtained from the measurement of the TOF. Therefore one must take special care to the calibration of the electronic equipment. In the measurements presented here an additional feature is given by the feature of the current ramp used to bias the junction. The ramp, indeed is extremely fast ($\gamma = 2.3$ mA/s) and, soon ($\simeq 1$ µs) after the detection of the switching the current, it is set to zero for a time of about 4 ms before the next ramp. This feature allows to prevent any heating effect of the current bias ("self heating"). The dwell time is set to be far above the relaxation time of the device.

Figure 88a shows the SCDs for temperatures going from 20 mK to 300 mK. From the figure three different regimes can be observed: macroscopic quantum tunneling (MQT), thermal activation regime (TA) and phase diffusion (PD). The crossover temperature T_{cr} between MQT and TA is 75 mK, while the turnover temperature T^* to the phase diffusion is 135 mK.

Figure 88b shows the experimental escape rates, extracted from SCDs at the temperature of 20 mK and 300 mK, and the best fit line for the escape rate at 20 mK. Above T^*, the escape rates are no longer reproducible with the model, and a Monte Carlo approach is required (see Sec. 6.3). The experimental signature is a bending of the $\log\Gamma(\Delta U)$ curve, clearly visible in the cyan curve of Fig. 88b. This effect is well known [115, 122], and it is a consequence of the symmetrization of the SCD in phase diffusion regime, as discussed in Sec. 6.2.

From the fit we have extracted the value of the critical current I_C and of the escape rate T_{esc} as a function of the temperature, shown in Fig. 89. From Fig. 89a it is possible to see that the junction switches at values of roughly 94% of I_C at 20 mK, that is fundamental for the correct evaluation of the junction parameters present below. Figure 89b clearly shows the three regimes (MQT, TA, PD) mentioned above.

Below T_{cr} the escape temperature is basically constant. This is a clear evidence that the junction is in a quantum regime as clearly confirmed when applying the magnetic field (see below). Indeed the escape

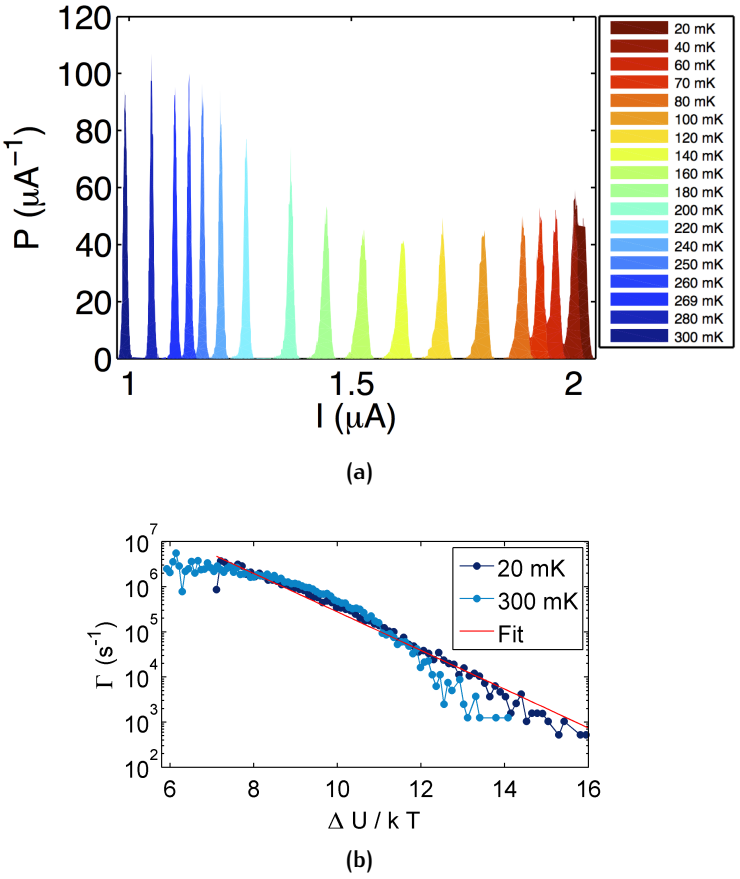

Figure 88: (a) Switching current distributions as a function of the temperature. The MQT regime can be seen below 75 mK (in red), the thermal activations follows at temperature between 75 and 135 mK (in orange - yellow). Above 135 mK a phase diffusion regime have been detected (in green - blue). (b) Escape rates as a function of the height of the potential barrier, normalized to $k_B T$. The curves at lower temperature ($T < 135$ mK) follows the ideal exponential behavior (linear in logarithmic scale). The red line is the fit of the model Eq. 39 to our data. Above T^* the curves show a pronounced bending, typical of the phase diffusion regime.

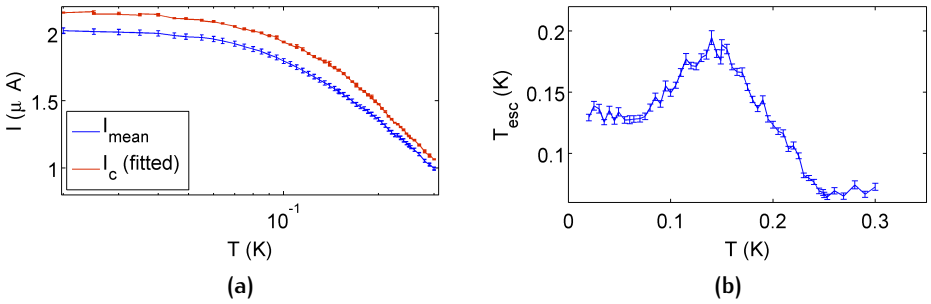

Figure 89: (a) Mean swithing current as a function of the temperature, extracted from the SCD shown in Fig. 88a (in blue). Data have been fitted with the model shown in Eq. 39. The values of the critical current I_C and of the escape temperature T_{esc} have been extracted from the fit of the SCD. The value of I_C vs the temperature is shown in red, the value of T_{esc} vs the temperature is shown in (b).

temperature is settled by the quantum noise of the device, determined by the plasma frequency ($k_B T_{esc} = \hbar\omega_p$). In TA regime, instead, the escape temperature is determined by the thermal noise, and it is proportional to the temperature of the bath. This determines the positive slope of the T_{esc} vs T curve at temperature between 75 mK and 135 mK. Finally above T^* the analytical model in no longer reliable, as the processes of multiple escapes and re-trappings becomes dominant. This is the characteristic feature of the phase diffusion regime, also described for NbN junctions (Sec. 6.2) and for YBCO bi-epitaxial junctions (6.4). In PD regime, the escape temperature decreases when T is increased. This qualitatively follows the behavior of the width of the distribution.

In Fig. 90 we show the mean switching current I_{sw} and the width of the histogram as a function of the temperature, for various values of the external magnetic field. This is a fundamental test to verify that the width of the distribution follows the modulation of the plasma frequency, which in fact is reduced by an external magnetic field. Increasing the field, the absolute value of w is reduced, ruling out the eventuality that the saturation of w at low temperatures is determined by a saturation of the sensitivity of the electronics. In addition, it is possible to verify that the two quantities T^* and T_{cr} modulates with the field. These quantities, in fact are connected to the Josephson energy $E_J = I_C\phi_0/2\pi$ and the plasma frequency $\omega_{p0} = \sqrt{2eI_C/\hbar C}$, respectively by the relations

$$\begin{aligned} T^* &\propto E_J/k_B \\ T_{cr} &= \frac{\hbar\omega_{p0}}{2\pi K_B} \end{aligned} \tag{79}$$

Therefore it is possible to verify the consistency of the model by tuning E_J and ω_p with the magnetic field. We verified that T^* and T_{cr} follows the expected modulations. This practically means that T^* scales with I_C, while T_{cr} scales with $\sqrt{I_C}$.

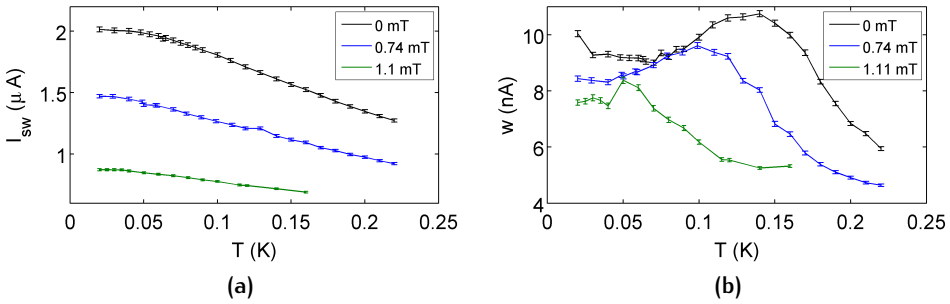

Figure 90: (a) Mean switching current as a function of the temperature for three different values of the external magnetic field. The value of I_{sw} was reduced by 27% with a magnetic field of 0.74 mT and by 57% with a field of 1.11 mT. (b) Width of the SCD as a function of the temperature. The width is reduced by applying an external magnetic field, as expected from the switching dynamics. Moreover the values of T_{cr} and T^* showed a modulation in agreement with the theoretical prediction (see text for details, Eq. 79).

Figure 91a shows the $w(T)$ curve at zero field, in a bi-logarithmic scale. The critical exponents of the curve in TA and PD regimes are extracted, as shown by the dashed lines. As shown in Fig. 91a, the $w(T)$ curve in MQT regime is not completely constant, but a small trend can be observed. This effect has to be attributed to the presence of a temperature dependence of the critical current I_C down to 20 mK. Junctions in a Ballistic regime, as discussed in Sec. 1.4, typically do not present any saturation of the $I_C(T)$ at low temperatures, which instead is the case observed in most of devices. The anomalous behavior of $w(T)$, which has been never observed so far to our knowledge, probably requires a redefinition of some standard notions of the escape dynamics.

A theoretical description of the phenomenology of the MQT in a ballistic regime has never been completely developed up to now, and its study obviously goes beyond the purposed of this work. However a tentative phenomenological description, inspired by the generalized Kurkjävi theory [108] is attempted below. We noticed that the width of the distribution scales with height of the barrier ΔU, which is in fact proportional to the critical current I_C, therefore a possible approach is to normalize at each temperature the width of the distribution to the of the height of the barrier ΔU. In Fig. 91b, the width have been normalized to the values of the I_{sw}, which has been used to extract an estimate of the barrier at the temperature T. The $w/I_{sw}(T)$ curve shows

a flat MQT regime, as expected in the standards of the conventional macroscopic quantum tunneling.

The critical exponent of the $w(T)$ curve, shown in Fig. 91a, in thermal activation regime does not follow the universal regime $T^{2/3}$. In our case an exponent of (0.279 ± 0.001) was exacted from the curve. This is close to an exponent 1/3. A scaling law of the $w(T)$ of 1/3 in TA regime was observed in graphene samples [45] and interpreted as a distinctive feature of a phase slip dynamics, in terms of a generalized Kurkjävi theory [108], mentioned above. However, the thermal excitation regime have been observed in our sample for a very narrow temperature range (since the crossover temperature is quite close to the PD transition) making a faithful estimation of the critical exponent rather difficult.

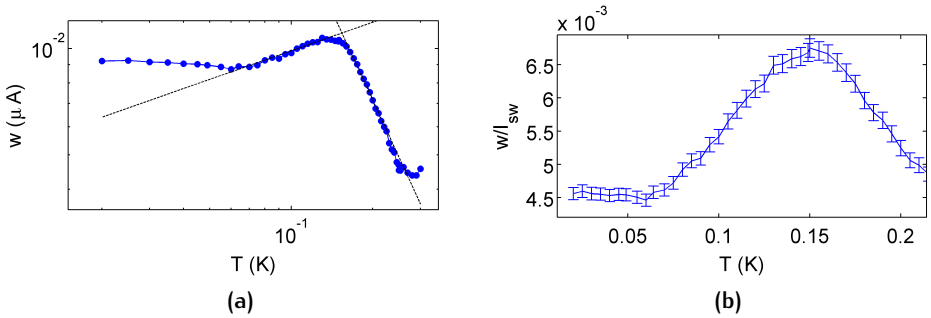

Figure 91: (a) Width of the zero field SCD in log log scale. The critical exponent of the TA and PD regime can be extrapolated with a linear fit (black dashed lines). The best fit gave the result of (0.269 ± 0.002) for the TA, and of (-1.668 ± 0.002) for the PD regime. (b) Width of the distribution normalized to I_C. The small trend visible in Fig. 91a in the MQT regime is not visible any more.

We have used $w(T)$ curve (see Fig. 91a) to make a careful estimation of the damping factors of the junction the zero field, taking advantage of the Monte Carlo simulations presented in [117], and Sec. 6.3.

Particularly we used the phase diagram shown in Fig. 76a to estimate the high frequency damping factor. A value of $Q_H \simeq 1.2$ is in a fair agreement with our data. The critical exponent of the $w(T)$ curves, instead gives information on the low frequency damping factor, as discussed, and in this case we extracted a value of $Q_L = 4.2$.

An independent estimation of the damping can also been extracted directly from the IV curve, taking into account the amount of hysteresis. From the Eq.35

$$Q^2 = \frac{2 - (\pi - 2) I_r/I_C}{(I_r/I_C)^2}$$

In this case we estimated $Q = 2.4$. This value is in reasonable agreement with data extracted from MC simulations

We have observed a crossover from MQT to TA at $T_{cr} = 75$ mK. This value, taking into account the value of the high frequency damping $Q_H = 1.2$ obtained from the simulations, implies a plasma frequency $\omega_{p0} = 314$ GHz and a junction capacitance of $C = 62$ fF. We used the well-known formula [172]

$$T_{cr} = \frac{\hbar\omega_p}{2\pi k_B}\left(\sqrt{1+\frac{1}{4Q_H(I_{sw})^2}}-\frac{1}{2Q_H(I_{sw})}\right) \tag{80}$$

which includes the effects of dissipations in the quantum regime [126, 75].

The estimation of the plasma frequency and capacitance of the junction is important to verify the self consistency of our model. In fact we can extract a value of the shunting resistance of the junction at high and low frequency and verify the congruence of these estimations with experimental data. This is an important fidelity test to support our approach and the main conclusions.

The low ($\simeq$ 50 fF) capacitance extracted is consistent with the coplanar geometries of devices with metallic barriers. The high frequency shunt value has been evaluated to be 61 Ω, in a reasonable agreement with data available in literature [117, 122, 115, 97, 200, 12]. Considering the effect of the low frequency damping factor, instead, one can obtain the shunt resistance at low frequency. In this case a value of 215 Ω can be extracted form the model, which is in agreement with the sub gap resistance of the junction.

6.6 CONCLUSIONS

We have presented a comparative study of escape dynamics in superconducting hybrid devices. This is a sector of interest for the integration of hybrid or unconventional barriers, which usually falls in the moderate damping regime. The analysis of this regime was performed through a confrontation of the Monte Carlo results, to data available in literature (including the ones on NbN junctions presented in this work). This effort was condensed in a Q - E_J/k_BT phase diagram. YBCO bi-epitaxial junctions are ideal candidates to explore new regimes of the phase diagram, engineering devices where direct MQT - PD transitions were observed.

We have measured IV curves of $Al/Bi_2Te_3/Al$ Josephson junctions as a function of the temperature, with a strong indication of a predominant ballistic transport regime, already observed for $Al/Bi_2Se_3/Al$ junctions (Chap. 5). On these devices the study of SCD gave evidence of a

moderately damped regime, which we have studied through a comparative analysis performed also on other junctions, specifically bi-epitaxial YBCO and NbN junctions, and further supported by a comparison with numerical codes based on Montecarlo simulations.

The merits of these measurements are to be the very first ones on junctions with topological barriers. This study is in progress and opens to the possibility of a better understanding of how the escape dynamics can be modified in the case of ballistic coherent transport regimes.

SUMMARY AND CONCLUSIONS

In this work we have studied proximity effect in hybrid devices. The main efforts are directed towards the study of $Al/Bi_2Se_3/Al$ and $Al/Bi_2Te_3/Al$ junctions, where the barrier is a topological insulator. In these devices evidence of Josephson effect have been obtained by a careful characterization of the superconducting transport in an external magnetic field, and in presence of a microwave field. A ballistic coherent transport in such a structures has been confirmed by the study of the $I_C(T)$ curve, that we have compared with numerical simulation of the temperature dependences for the diffusive and ballistic regimes. The importance of this finding lies in the fact we have been able to isolate the contribution of the surface edge states in the superconducting transport. This is one of the very first examples of Josephson super-current through a topologically protected surface state.

The evidence of a Josephson super-current through a topologically protected surface state is supported by a combined analysis of the superconducting transport and scanning tunneling microscopy. The presence of triangular defects, with a typical spacing of 10 nm was in fact confirmed by the morphological analysis of the STM. The notion of ballistic transport is clearly incompatible with the hypothesis that the transport is carried by the bulk of the crystal. In fact in this case the presence of defects would determine a diffusive regime of transport.

The presence of a two dimensional electron transport channel with a Dirac dispersion relation has been also confirmed through a high magnetic field characterization, obtained from a combination of transport measurements in Hall bars and a STM analysis performed on the cleaved surface of the crystal. Shubnikov - de Haas oscillations have been detected in Hall bars above 5 T, and the study of the oscillations as a function of the angle confirmed the 2D nature of the transport channel. The presence of aperiodic peaks, including an $N = 0$ Landau level, observed in STM, together with the direct detection of the Dirac

cone, confirmed the non-trivial topology of the channel, which was in fact identified as the topological surface state of the material. The normal transport at low field, instead, is dominated by the conductivity of the impurity states of the bulk of the crystal.

The superconducting hybrid devices studied in this work belongs to the family of moderately damped devices, which seems to be characteristic of the emergent nano/hybrid superconducting devices. The recent implementation of devices with unconventional barrier, as semiconducting nanowires, or bi-dimensional systems, promoted the occurrence of devices in the moderate damping regime. This is determined by the characteristic level of dissipation, and by the low critical current, observed in hybrids and nano-structures, and gives a strong motivation to a deeper understanding of dissipation at intermediate damping regimes.

The dynamics of the escape processes from the metastable zero bias state to the resistive state was studied in $Al/Bi_2Te_3/Al$ coplanar hybrid junctions. These devices showed a ballistic transport regime, also found in the $Al/Bi_2Se_3/Al$ junctions. The measurements of the escape dynamics gave evidence of a moderate damping regime, which we comparatively studied.

Proximity effect has been studied on various devices, with special focus to the escape dynamics. NbN junctions and YBCO bi-epitaxial junction were compared with those with a topological insulator barrier. All these devices have in common the same moderately high levels of damping ($Q \gtrsim 1$), and low critical current regime (1 μA). Though, the mechanisms underlying coherence and dissipation in these devices are significantly different. An attempt of a jointed description of all these phenomenology is condensed in a Q - E_J/k_BT phase diagram, obtained from the Monte Carlo simulation. Data of various devices, available in literature, showed a remarkable agreement with our numerical simulation. YBCO bi-epitaxial junctions turned out to be a fantastic tool to explore new regions of this phase diagram, including the possible direct transitions from macroscopic quantum tunneling to phase diffusion regimes.

We compared data of switching current distributions in $Al/Bi_2Te_3/Al$ with both the result obtained in S-I-S devices with LTS electrodes (NbN junctions) and with HTS devices (YBCO grain boundary junctions). These systems have been used as a reference to classify peculiar features in unconventional devices, as for instance those observed both in thermal activation and macroscopic quantum tunneling on $Al/Bi_2Te_3/Al$ junctions. These characteristics are probably related to the particular nature of the junctions, and to their ballistic transport regime.

ACKNOWLEDGMENTS

At the end of a long experience there are many people to thank.

First of all I would like to express my gratitude to prof. Antonio Barone, with whom I had the honor to move my first steps in the research. Antonio have been a fantastic guide, and his premature departure has left a great emptiness in our community.

I would like to thank my supervisor, prof. Francesco Tafuri, who has affectionately followed me along this PhD project, and prof. Floriana Lombardi, who shared with Francesco the responsibility of following me for most of my PhD work. I would also like to thank dott. Procolo Lucignano, prof. Thilo Bauch and dott. Sophie Charpentier for their remarkable contribution to this work, and prof. Anthony Leggett for the very useful and inspiring discussions.

A special thank goes to the whole staff of the Chalmers University of Technology, who housed me in a very friendly environment during my staying in Göteborg.

During this years, I always had the opportunity to work in a friendly and stimulating atmosphere. For this I would like to specially thank Daniela Stornaiuolo, Maria Ekström, Davide Massarotti, Riccardo Arpaia, Marco Arzeo, Reza Bagdadi, Domenico Montemurro, Luigi Longobardi, and all the people I had the pleasure to work with.

Last but not least I would like to thank my family, my friends, and all the people that supported me during these years.

This project was granted by:
MIUR-Italy through Prin project 2009 "Nanowire high critical temperature superconductor field-effect devices",
Progetto FIRB HybridNanoDev RBFR1236VV
COST Action - [MP1201] Nanoscale Superconductivity: "Novel Functionalities Through Optimized Confinement of Condensate and Fields" [NanoSC - COST]
and by the Swedish Research Council (VR) and SSF.

BIBLIOGRAPHY

[1] J. Alicea. New directions in the pursuit of majorana fermions in solid state systems. *Reports on Progress in Physics*, 75(7):076501, 2012.

[2] Z. Alpichshev, J. G. Analytis, J.-H. Chu, I. R. Fisher, Y. L. Chen, Z. X. Shen, A. Fang, and A. Kapitulnik. STM imaging of electronic waves on the surface of bi_2te_3: Topologically protected surface states and hexagonal warping effects. *Phys. Rev. Lett.*, 104:016401, 2010.

[3] Z. Alpichshev, R. R. Biswas, A. V. Balatsky, J. G. Analytis, J.-H. Chu, I. R. Fisher, and A. Kapitulnik. Stm imaging of impurity resonances on b2se3. *Phys. Rev. Lett.*, 108:206402, May 2012.

[4] B. L. Al'tschuler and B. Z. Spivak. Mesoscopic fluctuations in a superconductor-normal metal-superconductor junction. *Zh. Eksp. Theor. Fiz..*, 92(2):609, 1987.

[5] V. Ambegaokar, U. Eckern, and G. Schon. Quantum dynamics of tunneling between superconductors. *Phys. Rev. Lett.*, 48:1745–1748, Jun 1982.

[6] J. G. Analytis, R. D. McDonald, S. C. Riggs, J.-H. Chu, G. S. Boebinger, and I. R. Fisher. Two-dimensional surface state in the quantum limit of a topological insulator. *Nature Phys.*, 6:960, 2010.

[7] T. Ando. Theory of quantum transport in a two-dimensional electron system under magnetic fields. iii. many-site approximation. *J. Phys. Soc. Jpn.*, 37(3):662, 1974.

[8] Y. Ando. Topological insulator materials. *J. Phys. Soc. Jpn.*, 82:102001, 2013.

[9] A. Andreev. Zh. e ksp. teor. fiz. 46, 1823 1964 sov. phys. *JETP*, 19:1228, 1964.

[10] T. Aref, A. Levchenko, V. Vakaryuk, and A. Bezryadin. Quantitative analysis of quantum phase slips in superconducting mo76ge24 nanowires revealed by switching-current statistics. *Phys. Rev. B*, 86:024507, Jul 2012.

[11] J. E. Avron, D. Osadchy, and R. Seiler. A topological look at the quantum hall effect. *Physics Today*, 56(8):38, 2003.

[12] M.-H. Bae, M. Sahu, H.-J. Lee, and A. Bezryadin. Multiple-retrapping processes in the phase-diffusion regime of high t intrinsic josephson junctions. *Phys. Rev. B*, 79:104509, Mar 2009.

[13] A. Barone, F. Esposito, C. Magee, and A. Scott. Theory and applications of the sine-gordon equation. *La Rivista del Nuovo Cimento*, 1(2):227–267, 1971.

[14] A. Barone and G. Paterno. *Physics and Applications of the Josephson Effect*. John Wiley, New York, 1982.

[15] I. E. Batov, X. Jin, S. Shitov, Y. Koval, P. Muller, and A. Ustinov. Detection of 0.5 nbsp;thz radiation from intrinsic bi2sr2cacu208 josephson junctions. *Applied Physics Letters*, 88(26):262504–262504–3, Jun 2006.

[16] T. Bauch, T. Lindstrom, F. Tafuri, G. Rotoli, P. Delsing, T. Claeson, and F. Lombardi. Quantum dynamics of a d-wave josephson junction. *Science*, 311(5757):57–60, 2006.

[17] T. Bauch, F. Lombardi, F. Tafuri, A. Barone, G. Rotoli, P. Delsing, and T. Claeson. Macroscopic quantum tunneling in d-wave yba2cu307 josephson junctions. *Phys. Rev. Lett.*, 94:087003, Mar 2005.

[18] C. Beenakker. Search for majorana fermions in superconductors. *Ann. Rev. Cond. Mat. Phys.*, 4:113, 2013.

[19] C. W. J. Beenakker. *Three Universal Mesoscopic Josephson Effects*, chapter Transport Phenomena in Mesoscopic Systems, pages 235–253. Springer Verlag, New York, 1992.

[20] F. Behroozi, M. P. Garfunkel, F. H. Rogan, and G. A. Wilkinson. Temperature and magnetic field dependence of the superconducting penetration depth in pure and impure aluminum single crystals. *Phys. Rev. B*, 10:2756, 1974.

[21] E. Ben-Jacob, D. J. Bergman, B. J. Matkowsky, and Z. Schuss. Lifetime of oscillatory steady states. *Phys. Rev. A*, 26:2805–2816, Nov 1982.

[22] F. S. Bergeret, P. Virtanen, T. T. Heikkila, and J. C. Cuevas. Theory of microwave-assisted supercurrent in quantum point contacts. *Phys. Rev. Lett.*, 105:117001, Sep 2010.

[23] F. S. Bergeret, P. Virtanen, A. Ozaeta, T. T. Heikkila, and J. C. Cuevas. Supercurrent and andreev bound state dynamics

in superconducting quantum point contacts under microwave irradiation. *Phys. Rev. B*, 84:054504, Aug 2011.

[24] B. A. Bernevig, T. L. Hughes, and S.-C. Zhang. Quantum spin hall effect and topological phase transition in hgte quantum wells. *Science*, 314(5806):1757–1761, 2006.

[25] M. V. Berry. Quantal phase factor accompanying adiabatic changes. *Proc. R. Soc. Lond. A*, 392(1802):45, 1984.

[26] M. Bianchi, D. Guan, S. Bao, J. Mi, B. B. Iversen, P. D. King, and P. Hofmann. Coexistence of the topological state and a two-dimensional electron gas on the surface of bi2se3. *Nature communications*, 1:128, 2010.

[27] R. R. Biswas and A. V. Balatsky. Impurity-induced states on the surface of three-dimensional topological insulators. *Phys. Rev. B*, 81:233405, Jun 2010.

[28] A. M. Black-Schaffer and A. V. Balatsky. Strong potential impurities on the surface of a topological insulator. *Phys. Rev. B*, 85:121103, Mar 2012.

[29] G. Blatter. Schrodinger's cat is now fat. *Nature*, 406(6791):25, 07 2000.

[30] G. E. Blonder, M. Tinkham, and T. M. Klapwijk. Transition from metallic to tunneling regimes in superconducting microconstrictions: Excess current, charge imbalance, and supercurrent conversion. *Phys. Rev. B*, 25:4515, 1982.

[31] F. Born, D. Cassel, K. Ilin, A. Klushin, M. Siegel, A. Brinkman, A. Golubov, M. Y. Kupriyanov, and H. Rogalla. Transport properties of sinis junctions with high-current density. *Applied Superconductivity, IEEE Transactions on*, 13(2):1079–1084, June 2003.

[32] A. Brinkman and A. A. Golubov. Coherence effects in double-barrier josephson junctions. *Phys. Rev. B*, 61:11297–11300, May 2000.

[33] M. Buttiker, Y. Imry, R. Landauer, and S. Pinhas. Generalized many-channel conductance formula with application to small rings. *Phys. Rev. B*, 31:6207–6215, May 1985.

[34] A. O. Caldeira and A. J. Leggett. Influence of dissipation on quantum tunneling in macroscopic systems. *Phys. Rev. Lett.*, 46:211–214, Jan 1981.

[35] H. Cao, J. Tian, I. Miotkowski, T. Shen, J. Hu, S. Qiao, and Y. P. Chen. Quantized hall effect and shubnikov–de haas oscillations in highly doped bi_2se_3: Evidence for layered transport of bulk carriers. *Phys. Rev. Lett.*, 108:216803, 2012.

[36] A. H. Castro Neto, F. Guinea, N. M. R. Peres, K. S. Novoselov, and A. K. Geim. The electronic properties of graphene. *Rev. Mod. Phys.*, 81:109–162, Jan 2009.

[37] Y. L. Chen, J. G. Analytis, J.-H. Chu, Z. K. Liu, S.-K. Mo, X. L. Qi, H. J. Zhang, D. H. Lu, X. Dai, Z. Fang, S. C. Zhang, I. R. Fisher, Z. Hussain, and Z.-X. Shen. Experimental realization of a three-dimensional topological insulator, Bi_2Te_3. *Science*, 325:178, 2009.

[38] P. Cheng, C. Song, T. Zhang, Y. Zhang, Y. Wang, J.-F. Jia, J. Wang, Y. Wang, B.-F. Zhu, X. Chen, X. Ma, K. He, L. Wang, X. Dai, Z. Fang, X. Xie, X.-L. Qi, C.-X. Liu, S.-C. Zhang, and Q.-K. Xue. Landau quantization of topological surface states in bi_2se_3. *Phys. Rev. Lett.*, 105:076801, 2010.

[39] I. Chiorescu, P. Bertet, K. Semba, Y. Nakamura, C. J. P. M. Harmans, and J. E. Mooij. Coherent dynamics of a flux qubit coupled to a harmonic oscillator. *Nature*, 431(7005):7005, 2004.

[40] I. Chiorescu, Y. Nakamura, C. J. P. M. Harmans, and J. E. Mooij. Coherent quantum dynamics of a superconducting flux qubit. *Science*, 299(5614):1869–1871, 2003.

[41] H. O. H. Churchill, V. Fatemi, K. Grove-Rasmussen, M. T. Deng, P. Caroff, H. Q. Xu, and C. M. Marcus. Superconductor-nanowire devices from tunneling to the multichannel regime: Zero-bias oscillations and magnetoconductance crossover. *Phys. Rev. B*, 87:241401, 2013.

[42] J. Clarke. Squid fundamentals. In H. Weinstock, editor, *SQUID Sensors: Fundamentals, Fabrication and Applications*, volume 329 of *NATO ASI Series*, pages 1–62. Springer Netherlands, 1996.

[43] J. Clarke, A. N. Cleland, M. H. Devoret, D. Esteve, and J. M. Martinis. Quantum mechanics of a macroscopic variable: The phase difference of a josephson junction. *Science*, 239(4843):992–997, 1988.

[44] R. W. Cohen and B. Abeles. Superconductivity in granular aluminum films. *Phys. Rev.*, 168:444, 1968.

[45] U. C. Coskun, M. Brenner, T. Hymel, V. Vakaryuk, A. Levchenko, and A. Bezryadin. Distribution of supercurrent switching in graphene under the proximity effect. *Phys. Rev. Lett.*, 108:097003, Feb 2012.

[46] G. Costabile, R. D. Parmentier, B. Savo, D. W. McLaughlin, and A. C. Scott. Exact solutions of the sine gordon equation describing oscillations in a long (but finite) josephson junction. *Applied Physics Letters*, 32(9):587–589, 1978.

[47] M. S. Crosser, J. Huang, F. Pierre, P. Virtanen, T. T. Heikkila, F. K. Wilhelm, and N. O. Birge. Nonequilibrium transport in mesoscopic multi-terminal sns josephson junctions. *Phys. Rev. B*, 77:014528, Jan 2008.

[48] J. C. Cuevas and F. S. Bergeret. Magnetic interference patterns and vortices in diffusive sns junctions. *Phys. Rev. Lett.*, 99:217002, Nov 2007.

[49] A. Das, Y. Ronen, Y. Most, Y. Oreg, M. Heiblum, and H. Shtrikman. Zero-bias peaks and splitting in an al–inas nanowire topological superconductor as a signature of majorana fermions. *Nature Phys.*, 8:887, 2012.

[50] S. Datta. *Quantum Transport: Atom to Transistor*. ISBN-13 978-0-521-63145-7 -10 0-521-63145-9. Cambridge University Press, 2005.

[51] P. De Gennes and E. Guyon. Superconductivity in ?normal? metals. *Physics Letters*, 3(4):168–169, 1963.

[52] K. A. Delin and A. W. Kleinsasser. Stationary properties of high-critical-temperature proximity effect josephson junctions. *Superconductor Science and Technology*, 9(4):227, 1996.

[53] M. T. Deng, C. L. Yu, G. Y. Huang, M. Larsson, P. Caroff, and H. Q. Xu. Anomalous zero-bias conductance peak in a nb–insb nanowire–nb hybrid device. *Nano Lett.*, 12:6414, 2012.

[54] M. H. Devoret, J. M. Martinis, and J. Clarke. Measurements of macroscopic quantum tunneling out of the zero-voltage state of a current-biased josephson junction. *Phys. Rev. Lett.*, 55:1908–1911, Oct 1985.

[55] M. H. Devoret, A. Wallraff, and J. M. Martinis. Superconducting qubits: A short review. *arXiv*, cond-mat/0411174v1, 2004.

[56] P. Dubos, H. Courtois, O. Buisson, and B. Pannetier. Coherent low-energy charge transport in a diffusive s-n-s junction. *Phys. Rev. Lett.*, 87:206801, Oct 2001.

[57] R. C. Dynes and T. A. Fulton. Supercurrent density distribution in josephson junctions. *Phys. Rev. B*, 3:3015–3023, May 1971.

[58] K. Eto, Z. Ren, A. A. Taskin, K. Segawa, and Y. Ando. Angular-dependent oscillations of the magnetoresistance in bi2se3 due to the three-dimensional bulk fermi surface. *Phys. Rev. B*, 81:195309, May 2010.

[59] J. C. Fenton and P. A. Warburton. Monte carlo simulations of thermal fluctuations in moderately damped josephson junctions: Multiple escape and retrapping, switching- and return-current distributions, and hysteresis. *Phys. Rev. B*, 78:054526, Aug 2008.

[60] L. Fidkowski, H.-C. Jiang, R. M. Lutchyn, and C. Nayak. Magnetic and superconducting ordering in one-dimensional nanostructures at the laalo3srtio3 interface. *Phys. Rev. B*, 87:014436, Jan 2013.

[61] L. Fidkowski, R. M. Lutchyn, C. Nayak, and M. P. A. Fisher. Majorana zero modes in one-dimensional quantum wires without long-ranged superconducting order. *Phys. Rev. B*, 84:195436, Nov 2011.

[62] A. D. K. Finck, D. J. Van Harlingen, P. K. Mohseni, K. Jung, and X. Li. Anomalous modulation of a zero-bias peak in a hybrid nanowire-superconductor device. *Phys. Rev. Lett.*, 110:126406, 2013.

[63] L. Fu and C. L. Kane. Topological insulators with inversion symmetry. *Phys. Rev. B*, 76:045302, Jul 2007.

[64] L. Fu and C. L. Kane. Superconducting proximity effect and majorana fermions at the surface of a topological insulator. *Phys. Rev. Lett.*, 100:096407, 2008.

[65] L. Fu and C. L. Kane. Josephson current and noise at a superconductor/quantum-spin-hall-insulator/superconductor junction. *Phys. Rev. B*, 79:161408, Apr 2009.

[66] L. Fu, C. L. Kane, and E. J. Mele. Topological insulators in three dimensions. *Phys. Rev. Lett.*, 98:106803, 2007.

[67] A. Fulop, Y. Song, S. Charpentier, P. Shi, M. Ekstrom, L. Galletti, R. Arpaia, T. Bauch, F. Lombardi, and S. Wang. Phase transition of bismuth telluride thin films grown by mbe. *Applied Physics Express*, 7(4):045503, 2014.

[68] T. A. Fulton and L. N. Dunkleberger. Lifetime of the zero-voltage state in josephson tunnel junctions. *Phys. Rev. B*, 9:4760–4768, Jun 1974.

[69] A. V. Galaktionov and A. D. Zaikin. Quantum interference and supercurrent in multiple-barrier proximity structures. *Phys. Rev. B*, 65:184507, Apr 2002.

[70] L. Galletti, S. Charpentier, M. Iavarone, P. Lucignano, D. Massarotti, R. Arpaia, K. Kadowaki, T. Bauch, A. Tagliacozzo, F. Tafuri, and F. Lombardi. Influence of topological edge states on the properties of al/ bi_2se_3 /al hybrid josephson devices. *Phys. Rev. B*, (Accepted), 2014.

[71] L. Galletti, S. Charpentier, F. Tafuri, D. Massarotti, R. Arpaia, P. Lucignano, A. Tagliacozzo, T. Bauch, Y. Suzuki, K. Kadowaki, and F. Lombardi. Josephson effect in al/bi_2se_3/al coplanar hybrid devices. *Physica C*, (Submitted), 2014.

[72] F. Giazotto, T. T. Heikkila, G. P. Pepe, P. Helisto, A. Luukanen, and J. P. Pekola. Ultrasensitive proximity josephson sensor with kinetic inductance readout. *Applied Physics Letters*, 92(16):162507–162507–3, Apr 2008.

[73] A. A. Golubov, M. Y. Kupriyanov, and E. Il'ichev. The current-phase relation in josephson junctions. *Rev. Mod. Phys.*, 76:411–469, Apr 2004.

[74] H. Grabert. Escape from a metastable well: The kramers turnover problem. *Phys. Rev. Lett.*, 61:1683–1686, Oct 1988.

[75] H. Grabert, U. Weiss, and P. Hanggi. Quantum tunneling in dissipative systems at finite temperatures. *Phys. Rev. Lett.*, 52:2193–2196, Jun 1984.

[76] S. Groot. Termodinamica dei processi irreversibili e generalizzazioni delle relazioni di onsager. *Il Nuovo Cimento*, 12(1):5–16, 1954.

[77] G. Grosso and G. Pastori Parravicini. *Solid State Physics*, volume 1 of *ISBN 0-12-304460-X*. Academic Press - Elsvier Science, 2nd edition, 2000.

[78] E. H. Hall. On a new action of the magnet on electric currents. *American Journal of Mathematics*, 2(3):pp. 287–292, 1879.

[79] T. Hanaguri, K. Igarashi, M. Kawamura, H. Takagi, and T. Sasagawa. Momentum-resolved landau-level spectroscopy of dirac surface state in b_2se_3. *Phys. Rev. B*, 82:081305, 2010.

[80] S. T. Hannahs, J. S. Brooks, W. Kang, L. Y. Chiang, and P. M. Chaikin. Quantum hall effect in a bulk crystal. *Phys. Rev. Lett.*, 63:1988–1991, Oct 1989.

[81] M. Z. Hasan and C. L. Kane. *Colloquium* : Topological insulators. *Rev. Mod. Phys.*, 82:3045, 2010.

[82] K. He, Y. Zhang, C.-Z. Chang, C.-L. Song, L.-L. Wang, X. Chen, J.-F. Jia, Z. Fang, X. Dai, W.-Y. Shan, S.-Q. Shen, Q. Niu, X.-L. Qi, S.-C. Zhang, X.-C. Ma, and Q.-K. Xue. Crossover of the three-dimensional topological insulator Bi_2Se_3 to the two-dimensional limit. *Nature Phys.*, 6:584, 2010.

[83] L. He, F. Xiu, X. Yu, M. Teague, W. Jiang, Y. Fan, X. Kou, M. Lang, Y. Wang, G. Huang, N.-C. Yeh, and K. L. Wang. Surface-dominated conduction in a 6 nm thick bi2se3 thin film. *Nano Lett.*, 12(3):1486–1490, 2012.

[84] S. Hill, S. Uji, M. Takashita, C. Terakura, T. Terashima, H. Aoki, J. S. Brooks, Z. Fisk, and J. Sarrao. Bulk quantum hall effect in ? - moo11. *Phys. Rev. B*, 58:10778–10783, Oct 1998.

[85] D. R. Hofstadter. Energy levels and wave functions of bloch electrons in rational and irrational magnetic fields. *Phys. Rev. B*, 14:2239–2249, Sep 1976.

[86] D. Hsieh, Y. Xia, D. Qian, L. Wray, J. H. Dil, F. Meier, J. Osterwalder, L. Patthey, J. G. Checkelsky, N. P. Ong, A. V. Fedorov, H. Lin, A. Bansil, D. Grauer, Y. S. Hor, R. J. Cava, and M. Z. Hasan. A tunable topological insulator in the spin helical Dirac transport regime. *Nature*, 460:1101, 2009.

[87] M. Iansiti, A. T. Johnson, W. F. Smith, H. Rogalla, C. J. Lobb, and M. Tinkham. Charging energy and phase delocalization in single very small josephson tunnel junctions. *Phys. Rev. Lett.*, 59:489–492, Jul 1987.

[88] M. Iansiti, M. Tinkham, A. T. Johnson, W. F. Smith, and C. J. Lobb. Charging effects and quantum properties of small superconducting tunnel junctions. *Phys. Rev. B*, 39:6465–6484, Apr 1989.

[89] E. Il'ichev, V. Zakosarenko, R. P. J. IJsselsteijn, H. E. Hoenig, V. Schultze, H.-G. Meyer, M. Grajcar, and R. Hlubina. Anomalous

periodicity of the current-phase relationship of grain-boundary josephson junctions in high-tc superconductors. *Phys. Rev. B*, 60:3096–3099, Aug 1999.

[90] L. Jiang, D. Pekker, J. Alicea, G. Refael, Y. Oreg, and F. von Oppen. Unconventional josephson signatures of majorana bound states. *Phys. Rev. Lett.*, 107:236401, 2011.

[91] B. D. JOSEPHSON. Coupled superconductors. *Rev. Mod. Phys.*, 36:216–220, Jan 1964.

[92] S. Kashiwaya and Y. Tanaka. Tunnelling effects on surface bound states in unconventional superconductors. *Reports on Progress in Physics*, 63(10):1641, 2000.

[93] R. L. Kautz and J. M. Martinis. Noise-affected i-v curves in small hysteretic josephson junctions. *Phys. Rev. B*, 42:9903–9937, Dec 1990.

[94] Y. S. Kim, M. Brahlek, N. Bansal, E. Edrey, G. A. Kapilevich, K. Iida, M. Tanimura, Y. Horibe, S.-w. Cheong, and S. Oh. Thickness-dependent bulk properties and weak antilocalization effect in topological insulator bi2se3. *Phys. Rev. B*, 84:073109, 2011.

[95] A. Kitaev. Fault-tolerant quantum computation by anyons. *Annals of Physics*, 303(1):2 – 30, 2003.

[96] A. Y. Kitaev. Unpaired majorana fermions in quantum wires. *Phys.-Usp.*, 44:131, 2001.

[97] J. M. Kivioja, T. E. Nieminen, J. Claudon, O. Buisson, F. W. J. Hekking, and J. P. Pekola. Observation of transition from escape dynamics to underdamped phase diffusion in a josephson junction. *Phys. Rev. Lett.*, 94:247002, Jun 2005.

[98] K. v. Klitzing, G. Dorda, and M. Pepper. New method for high-accuracy determination of the fine-structure constant based on quantized hall resistance. *Phys. Rev. Lett.*, 45:494–497, Aug 1980.

[99] J. Kohlmann and R. Behr. *book - Superconductivity - Theory and Applications*. Number ISBN 978-953-307-151-0. Adir Moyses Luiz, 2011-07-18.

[100] M. Kohmoto, B. I. Halperin, and Y.-S. Wu. Diophantine equation for the three-dimensional quantum hall effect. *Phys. Rev. B*, 45:13488–13493, Jun 1992.

[101] M. Konig, S. Wiedmann, C. Brune, A. Roth, H. Buhmann, L. W. Molenkamp, X.-L. Qi, and S.-C. Zhang. Quantum spin hall insulator state in hgte quantum wells. *Science*, 318(5851):766–770, 2007.

[102] G. Koren and T. Kirzhner. Zero-energy bound states in tunneling conductance spectra at the interface of an s-wave superconductor and a topological insulator in nbn/bi_2se_3/au thin-film junctions. *Phys. Rev. B*, 86:144508, 2012.

[103] G. Koren, T. Kirzhner, E. Lahoud, K. B. Chashka, and A. Kanigel. Proximity-induced superconductivity in topological bi2se and bi2se3 films: Robust zero-energy bound state possibly due to majorana fermions. *Phys. Rev. B*, 84:224521, Dec 2011.

[104] V. M. Krasnov, T. Bauch, S. Intiso, E. Hurfeld, T. Akazaki, H. Takayanagi, and P. Delsing. Collapse of thermal activation in moderately damped josephson junctions. *Phys. Rev. Lett.*, 95:157002, Oct 2005.

[105] V. Z. Kresin. Josephson current in low-dimensional proximity systems and the field effect. *Phys. Rev. B*, 34:7587, 1986.

[106] M. Kupriyanov, A. Brinkman, A. Golubov, M. Siegel, and H. Rogalla. Double-barrier josephson structures as the novel elements for superconducting large-scale integrated circuits. *Physica C: Superconductivity*, 326–327(0):16 – 45, 1999.

[107] M. Y. Kupriyanov and L. V. F. Influence of boundary transparency on the critical current of dirty ss's structures. *Zh. Eksp. Theor. Fiz.*, 94(6):139, 1988.

[108] J. Kurkijarvi. Intrinsic fluctuations in a superconducting ring closed with a josephson junction. *Phys. Rev. B*, 6:832–835, Aug 1972.

[109] C. N. Lau, N. Markovic, M. Bockrath, A. Bezryadin, and M. Tinkham. Quantum phase slips in superconducting nanowires. *Phys. Rev. Lett.*, 87:217003, Nov 2001.

[110] R. B. Laughlin. Quantized hall conductivity in two dimensions. *Phys. Rev. B*, 23:5632–5633, May 1981.

[111] K. W. Lehnert, N. Argaman, H.-R. Blank, K. C. Wong, S. J. Allen, E. L. Hu, and H. Kroemer. Nonequilibrium ac josephson effect in mesoscopic nb-inas-nb junctions. *Phys. Rev. Lett.*, 82:1265, 1999.

[112] R. Leoni, G. Arena, M. G. Castellano, and G. Torrioli. Electron cooling by arrays of submicron tunnel junctions. *Journal of Applied Physics*, 85(7):3877–3881, 1999.

[113] K. K. Likharev. Superconducting weak links. *Rev. Mod. Phys.*, 51:101–159, Jan 1979.

[114] F. Lombardi, F. Tafuri, F. Ricci, F. M. Granozio, A. Barone, G. Testa, E. . Sarnelli, J. R. Kirtley, and C. C. Tsuei. Intrinsic d-wave effects in yba2cu3o7 grain boundary josephson junctions. *Phys. Rev. Lett.*, 89:207001, Oct 2002.

[115] L. Longobardi, D. Massarotti, G. Rotoli, D. Stornaiuolo, G. Papari, A. Kawakami, G. P. Pepe, A. Barone, and F. Tafuri. Thermal hopping and retrapping of a brownian particle in the tilted periodic potential of a nbn/mgo/nbn josephson junction. *Phys. Rev. B*, 84:184504, Nov 2011.

[116] L. Longobardi, D. Massarotti, G. Rotoli, D. Stornaiuolo, G. Papari, A. Kawakami, G. Piero Pepe, A. Barone, and F. Tafuri. Quantum crossover in moderately damped epitaxial nbn/mgo/nbn junctions with low critical current density. *Applied Physics Letters*, 99(6), 2011.

[117] L. Longobardi, D. Massarotti, D. Stornaiuolo, L. Galletti, G. Rotoli, F. Lombardi, and F. Tafuri. Direct transition from quantum escape to a phase diffusion regime in ybacuo biepitaxial josephson junctions. *Phys. Rev. Lett.*, 109:050601, Aug 2012.

[118] P. Lucignano, A. Mezzacapo, F. Tafuri, and A. Tagliacozzo. Advantages of using high-temperature cuprate superconductor heterostructures in the search for majorana fermions. *Phys. Rev. B*, 86:144513, Oct 2012.

[119] I. A. Luk'yanchuk and Y. Kopelevich. Dirac and normal fermions in graphite and graphene: Implications of the quantum hall effect. *Phys. Rev. Lett.*, 97:256801, Dec 2006.

[120] I. A. Luk'yanchuk and Y. Kopelevich. Dirac and normal fermions in graphite and graphene: Implications of the quantum hall effect. *Phys. Rev. Lett.*, 97:256801, Dec 2006.

[121] E. Majorana. Teoria simmetrica dell'elettrone e del positrone. *Il Nuovo Cimento*, 14(4):171–184, 1937.

[122] J. Mannik, S. Li, W. Qiu, W. Chen, V. Patel, S. Han, and J. E. Lukens. Crossover from kramers to phase-diffusion switching in moderately damped josephson junctions. *Phys. Rev. B*, 71:220509, Jun 2005.

[123] J. M. Martinis, M. H. Devoret, and J. Clarke. Experimental tests for the quantum behavior of a macroscopic degree of freedom: The phase difference across a josephson junction. *Phys. Rev. B*, 35:4682–4698, Apr 1987.

[124] J. M. Martinis and R. L. Kautz. Classical phase diffusion in small hysteretic josephson junctions. *Phys. Rev. Lett.*, 63:1507–1510, Oct 1989.

[125] D. Massarotti. *Macroscopic Quantum Phenomena in Superconductors: Study of the Phase Dynamics and Dissipation in Moderately Damped Junctions*. PhD thesis, Fundamental and Applied Physics, 2013.

[126] D. Massarotti, F. Lombardi, L. Galletti, D. Stornaiuolo, D. Montemurro, G. P. Pepe, G. Rotoli, A. Barone, and F. Tafuri. Escape dynamics in moderately damped josephson junctions. *Low Temperature Physics/Fizika Nizkikh Temperatur*, 38(263), 2012.

[127] D. Massarotti, L. Longobardi, L. Galletti, D. Stornaiuolo, G. Rotoli, and F. Tafuri. Macroscopic quantum tunneling and retrapping processes in moderately damped ybacuo josephson junctions. *Low Temperature Physics/Fizika Nizkikh Temperatur*, 39(294):378–383, 2013.

[128] D. Massarotti, L. Longobardi, D. Stornaiuolo, L. Galletti, G. Rotoli, A. Kawakami, G. Pepe, and F. Tafuri. Study of phase dynamics in moderately damped josephson junctions. *Journal of Superconductivity and Novel Magnetism*, 26(4):835–838, 2013.

[129] D. Massarotti, D. Stornaiuolo, G. Rotoli, F. Carillo, L. Galletti, L. Longobardi, F. Beltram, and F. Tafuri. Phase dynamics of low critical current density ybco josephson junctions. *Physica C: Superconductivity*, Proceedings of VORTEX VII Conference((submitted)), 2014.

[130] J. Matisoo. Critical currents and current distributions in josephson junctions. *Journal of Applied Physics*, 40(4):1813–1820, 1969.

[131] D. E. McCumber. Effect of ac impedance on dc voltagecurrent characteristics of superconductor weaklink junctions. *Journal of Applied Physics*, 39(7):3113–3118, 1968.

[132] D. E. McCumber. Tunneling and weak äêlink superconductor phenomena having potential device applications. *Journal of Applied Physics*, 39(6):2503–2508, 1968.

[133] R. McDermott, A. H. Trabesinger, M. Muck, E. L. Hahn, A. Pines, and J. Clarke. Liquid-state nmr and scalar couplings in microtesla magnetic fields. *Science*, 295(5563):2247–2249, 2002.

[134] W. L. McMillan. Theory of superconductor?normal-metal interfaces. *Phys. Rev.*, 175:559–568, Nov 1968.

[135] J. E. Mooij, T. P. Orlando, L. Levitov, L. Tian, C. H. van der Wal, and S. Lloyd. Josephson persistent-current qubit. *Science*, 285(5430):1036–1039, 1999.

[136] J. E. Moore. The birth of topological insulators. *Nature*, 464:194, 2010.

[137] J. E. Moore and L. Balents. Topological invariants of time-reversal-invariant band structures. *Phys. Rev. B*, 75:121306, Mar 2007.

[138] A. F. Morpurgo, T. M. Klapwijk, and B. J. van Wees. Hot electron tunable supercurrent. *Applied Physics Letters*, 72(8):966–968, 1998.

[139] V. Mourik, K. Zuo, S. M. Frolov, S. R. Plissard, E. P. A. M. Bakkers, and L. P. Kouwenhoven. Signatures of majorana fermions in hybrid superconductor-semiconductor nanowire devices. *Science*, 336:1003, 2012.

[140] S. Nakosai, Y. Tanaka, and N. Nagaosa. Topological superconductivity in bilayer rashba system. *Phys. Rev. Lett.*, 108:147003, Apr 2012.

[141] S. Nawaz, R. Arpaia, F. Lombardi, and T. Bauch. Microwave response of superconducting yba2cu307-x nanowire bridges sustaining the critical depairing current: Evidence of josephson-like behavior. *Phys. Rev. Lett.*, 110:167004, Apr 2013.

[142] K. Novoselov, A. K. Geim, S. Morozov, D. Jiang, M. Katsnelson, I. Grigorieva, S. Dubonos, and A. Firsov. Two-dimensional gas of massless dirac fermions in graphene. *nature*, 438(7065):197–200, 2005.

[143] K. Novoselov, E. McCann, S. Morozov, V. I. Fal?ko, M. Katsnelson, U. Zeitler, D. Jiang, F. Schedin, and A. Geim. Unconventional quantum hall effect and berry?s phase of 2π in bilayer graphene. *Nature Physics*, 2(3):177–180, 2006.

[144] K. S. Novoselov, A. K. Geim, S. V. Morozov, D. Jiang, M. I. Katsnelson, I. V. Grigorieva, S. V. Dubonos, and A. A. Firsov. Two-dimensional gas of massless dirac fermions in graphene. *Nature*, 438(7065):197–200, November 2005.

[145] K. S. Novoselov, Z. Jiang, Y. Zhang, S. V. Morozov, H. L. Stormer, U. Zeitler, J. C. Maan, G. S. Boebinger, P. Kim, and A. K. Geim.

Room-temperature quantum hall effect in graphene. *Science*, 315(5817):1379, 2007.

[146] J. B. Oostinga, L. Maier, P. Schuffelgen, D. Knott, C. Ames, C. Brune, G. Tkachov, H. Buhmann, and L. W. Molenkamp. Josephson supercurrent through the topological surface states of strained bulk hgte. *Phys. Rev. X*, 3:021007, 2013.

[147] C. S. Owen and D. J. Scalapino. Vortex structure and critical currents in josephson junctions. *Phys. Rev.*, 164:538–544, Dec 1967.

[148] Y. A. Pashkin, T. Yamamoto, O. Astafiev, Y. Nakamura, D. V. Averin, and J. S. Tsai. Quantum oscillations in two coupled charge qubits. *Nature*, 421(6925):823, 02 2003.

[149] D. I. Pikulin and Y. V. Nazarov. Phenomenology and dynamics of a majorana josephson junction. *Phys. Rev. B*, 86:140504, Oct 2012.

[150] A. C. Potter and L. Fu. Anomalous supercurrent from majorana states in topological insulator Josephson junctions. *Phys. Rev. B*, 88:121109, 2013.

[151] X.-L. Qi and S.-C. Zhang. The quantum spin hall effect and topological insulators. *Physics Today*, 63(1):33, 2010.

[152] D.-X. Qu, Y. S. Hor, J. Xiong, R. J. Cava, and N. P. Ong. Quantum oscillations and hall anomaly of surface states in the topological insulator Bi_2Te_3. *Science*, 329:821, 2010.

[153] L. P. Rokhinson, X. Liu, and J. K. Furdyna. The fractional a.c. josephson effect in a semiconductor–superconductor nanowire as a signature of majorana particles. *Nature Phys.*, 8:795, 2012.

[154] R. Romestain, B. Delaet, P. Renaud-Goud, I. Wang, C. Jorel, J.-C. Villegier, and J.-P. Poizat. Fabrication of a superconducting niobium nitride hot electron bolometer for single-photon counting. *New Journal of Physics*, 6(1):129, 2004.

[155] P. A. Rosenthal, M. R. Beasley, K. Char, M. S. Colclough, and G. Zaharchuk. Flux focusing effects in planar thinfilm grainboundary josephson junctions. *Appl. Phys. Lett.*, 59:3482, 1991.

[156] R. Roy. Topological phases and the quantum spin hall effect in three dimensions. *Phys. Rev. B*, 79:195322, May 2009.

[157] P. Russer. Influence of microwave radiation on current-voltage characteristic of superconducting weak links. *J. Appl. Phys.*, 43:2008, 1972.

[158] B. Sacepe, J. B. Oostinga, J. Li, A. Ubaldini, N. J. G. Couto, E. Giannini, and A. F. Morpurgo. Gate-tuned normal and superconducting transport at the surface of a topological insulator. *Nat. Commun.*, 2:575, 2011.

[159] M. Sahu, M.-H. Bae, A. Rogachev, D. Pekker, T.-C. Wei, N. Shah, P. M. Goldbart, and A. Bezryadin. Individual topological tunnelling events of a quantum field probed through their macroscopic consequences. *Nat Phys*, 5(7):503, 07 2009/07.

[160] D. Shoenberg. *Magnetic oscillations in metals*. Cambridge University Press, 1984.

[161] M. Snelder, M. Veldhorst, A. A. Golubov, and A. Brinkman. Andreev bound states and current-phase relations in three-dimensional topological insulators. *Phys. Rev. B*, 87:104507, 2013.

[162] I. Sochnikov, A. J. Bestwick, J. R. Williams, T. M. Lippman, I. R. Fisher, D. Goldhaber-Gordon, J. R. Kirtley, and K. A. Moler. Direct measurement of current-phase relations in superconductor/topological insulator/superconductor junctions. *Nano Lett.*, 13:3086, 2013.

[163] Y. Song, S. Charpentier, I. S. Roy, M. Ekstrom, L. Galletti, F. Lombardi, and S. Wang. Mbe growth of bi2te3 for thermoelectric and topological insulators. *MBE 2012*, Special Issue, 2012.

[164] H. Steinberg, D. R. Gardner, Y. S. Lee, and P. Jarillo-Herrero. Surface state transport and ambipolar electric field effect in Bi_2Se_3 nanodevices. *Nano Lett.*, 10:5032, 2010.

[165] W. C. Stewart. Current-voltage characteristics of josephson junctions. *Applied Physics Letters*, 12(8):277–280, 1968.

[166] H. L. Stormer, J. P. Eisenstein, A. C. Gossard, W. Wiegmann, and K. Baldwin. Quantization of the hall effect in an anisotropic three-dimensional electronic system. *Phys. Rev. Lett.*, 56:85, 1986.

[167] H. L. Stormer, J. P. Eisenstein, A. C. Gossard, W. Wiegmann, and K. Baldwin. Quantization of the hall effect in an anisotropic three-dimensional electronic system. *Phys. Rev. Lett.*, 56:85–88, Jan 1986.

[168] D. Stornaiuolo. *Advances in HTS mesoscopic junctions Advances in HTS mesoscopic junctions Advances in HTS mesoscopic junctions*. PhD thesis, Technologie Innovative per i Material, i Sensori e l'Imaging, 2007.

[169] D. Stornaiuolo, G. Papari, N. Cennamo, F. Carillo, L. Longobardi, D. Massarotti, A. Barone, and F. Tafuri. High quality factor hts josephson junctions on low loss substrates. *Superconductor Science and Technology*, 24(4):045008, 2011.

[170] K. Suzuki, S. Miki, S. Shiki, Z. Wang, and M. Ohkubo. Time resolution improvement of superconducting nbn stripline detectors for time-of-flight mass spectrometry. *Applied Physics Express*, 1(3):031702, 2008.

[171] F. Tafuri and J. R. Kirtley. Weak links in high critical temperature superconductors. *Reports on Progress in Physics*, 68(11):2573, 2005.

[172] F. Tafuri, D. Massarotti, L. Galletti, D. Stornaiuolo, D. Montemurro, L. Longobardi, P. Lucignano, G. Rotoli, G. Pepe, A. Tagliacozzo, and F. Lombardi. Recent achievements on the physics of high-tc superconductor josephson junctions: Background, perspectives and inspiration. *Journal of Superconductivity and Novel Magnetism*, 26(1):21–41, 2013.

[173] F. Tafuri, D. Stornaiuolo, P. Lucignano, L. Galletti, L. Longobardi, D. Massarotti, D. Montemurro, G. Papari, A. Barone, and A. Tagliacozzo. Energy scales in ybacuo grain boundary biepitaxial josephson junctions. *Physica C: Superconductivity*, 479(0):74 – 78, 2012. Proceedings of VORTEX VII Conference.

[174] A. A. Taskin, Z. Ren, S. Sasaki, K. Segawa, and Y. Ando. Observation of Dirac holes and electrons in a topological insulator. *Phys. Rev. Lett.*, 107:016801, 2011.

[175] A. A. Taskin, S. Sasaki, K. Segawa, and Y. Ando. Manifestation of topological protection in transport properties of epitaxial bi_2se_3 thin films. *Phys. Rev. Lett.*, 109:066803, 2012.

[176] C. Tesche and J. Clarke. dc squid: Noise and optimization. *Journal of Low Temperature Physics*, 29(3-4):301–331, 1977.

[177] M. Thinkham. *Introduction to Superconductivity*. ISBN 0-07-064878-6. McGraw-Hill, Inc., 2d edition, 1996.

[178] D. J. Thouless, M. Kohmoto, M. P. Nightingale, and M. den Nijs. Quantized hall conductance in a two-dimensional periodic potential. *Phys. Rev. Lett.*, 49:405–408, Aug 1982.

[179] A. Y. Tzalenchuk, T. Lindstrom, S. A. Charlebois, E. A. Stepantsov, Z. Ivanov, and A. M. Zagoskin. Mesoscopic josephson junctions of high-tc superconductors. *Phys. Rev. B*, 68:100501, Sep 2003.

[180] K. D. Usadel. Generalized diffusion equation for superconducting alloys. *Phys. Rev. Lett.*, 25:507–509, Aug 1970.

[181] A. Ustinov and S. Sakai. Submillimeter-band high-power generation using multilayered josephson junctions. *Applied Physics Letters*, 73(5):686–688, Aug 1998.

[182] A. V. Ustinov, H. Kohlstedt, and P. Henne. Giant radiation linewidth of multifluxon states in long josephson junctions. *Phys. Rev. Lett.*, 77:3617–3620, Oct 1996.

[183] M. Veldhorst, C. G. Molenaar, C. J. M. Verwijs, H. Hilgenkamp, and A. Brinkman. Optimizing the majorana character of squids with topologically nontrivial barriers. *Phys. Rev. B*, 86:024509, 2012.

[184] M. Veldhorst, C. G. Molenaar, X. L. Wang, H. Hilgenkamp, and A. Brinkman. Experimental realization of superconducting quantum interference devices with topological insulator junctions. *Appl. Phys. Lett.*, 100:072602, 2012.

[185] M. Veldhorst, M. Snelder, M. Hoek, T. Gang, V. K. Guduru, X. L. Wang, U. Zeitler, W. G. van der Wiel, A. A. Golubov, H. Hilgenkamp, and A. Brinkman. Josephson supercurrent through a topological insulator surface state. *Nature Mater.*, 11:417, 2012.

[186] M. Veldhorst, M. Snelder, M. Hoek, C. G. Molenaar, D. P. Leusink, A. A. Golubov, H. Hilgenkamp, and A. Brinkman. Magnetotransport and induced superconductivity in bi based three-dimensional topological insulators. *physica status solidi (RRL) - Rapid Research Letters*, 7(1-2):26–38, 2013.

[187] D. Vion, A. Aassime, A. Cottet, P. Joyez, H. Pothier, C. Urbina, D. Esteve, and M. H. Devoret. Manipulating the quantum state of an electrical circuit. *Science*, 296(5569):886–889, 2002.

[188] J. Waldram and J. Lumley. Direct measurements of the current-phase relation in superconducting weak links. *Rev. Phys. Appl.*, 10:7–10, 1975.

[189] A. Wallraff, D. I. Schuster, A. Blais, L. Frunzio, R.-S. Huang, J. Majer, S. Kumar, S. M. Girvin, and R. J. Schoelkopf. Strong coupling of a single photon to a superconducting qubit using circuit quantum electrodynamics. *Nature*, 431(7005):162, 09 2004.

[190] D. Waxman and A. J. Leggett. Dissipative quantum tunneling at finite temperatures. *Phys. Rev. B*, 32:4450–4468, Oct 1985.

[191] J. R. Williams, A. J. Bestwick, P. Gallagher, S. S. Hong, Y. Cui, A. S. Bleich, J. G. Analytis, I. R. Fisher, and D. Goldhaber-Gordon. Unconventional josephson effect in hybrid superconductor-topological insulator devices. *Phys. Rev. Lett.*, 109:056803, 2012.

[192] Y. Xia, D. Qian, D. Hsieh, L. Wray, A. Pal, H. Lin, D. Bansil, A.and Grauer, Y. S. Hor, R. J. Cava, and M. Z. Hasan. Observation of a large-gap topological-insulator class with a single Dirac cone on the surface. *Nature Phys.*, 5:398, 2009.

[193] J. Xiong, Y. Luo, Y. Khoo, S. Jia, R. J. Cava, and N. P. Ong. High-field Shubnikov-de Haas oscillations in the topological insulator Bi_2Te_2Se. *Phys. Rev. B*, 86:045314, 2012.

[194] J. Xiong, A. Petersen, D. Qu, Y. Hor, R. Cava, and N. Ong. Quantum oscillations in a topological insulator bi2te2se with large bulk resistivity (). *Physica E: Low-dimensional Systems and Nanostructures*, 44(5):917 – 920, 2012. SI:Topological Insulators.

[195] F. Xiu, L. He, Y. Wang, L. Cheng, L.-T. Chang, M. Lang, G. Huang, X. Kou, Y. Zhou, X. Jiang, Z. Chen, J. Zou, A. Shailos, and K. L. Wang. Manipulating surface states in topological insulator nanoribbons. *Nature Nanotech.*, 6:216, 2011.

[196] T. Yamashita and Y. Onodera. Magnetic field dependence of josephson current influenced by self field. *Journal of Applied Physics*, 38(9):3523–3525, 1967.

[197] I. Yanson. Effect of fluctuation on the dependence of the josephson current on the magnetic field. *Soviet Physics JETP*, 31(5), 1970.

[198] I. Yanson. Influence of barrier inhomogeneities on the josephson critical current. *Tr. Fiz. Teck. Inst. Nizk. Temp.*, 8:19–26, 1970.

[199] Y. Yoon, S. Gasparinetti, M. Mottonen, and J. Pekola. Capacitively enhanced thermal escape in underdamped josephson junctions. *Journal of Low Temperature Physics*, 163(3-4):164–169, 2011.

[200] H. F. Yu, X. B. Zhu, Z. H. Peng, Y. Tian, D. J. Cui, G. H. Chen, D. N. Zheng, X. N. Jing, L. Lu, S. P. Zhao, and S. Han. Quantum phase diffusion in a small underdamped josephson junction. *Phys. Rev. Lett.*, 107:067004, Aug 2011.

[201] A. D. Zaikin and Z. G. F. Contribution to the theory of weak superconductivity in sinis systems. *Zh. Eksp. Theor. Fiz..*, 78:721–732, 1978.

[202] H. H. Zappe. Minimum current and related topics in josephson tunnel junction devices. *Journal of Applied Physics*, 44(3):1371–1377, 1973.

[203] Zhang, T. Yuanbo, S. Yan-Wen, and L. K. P. Horst. Experimental observation of the quantum hall effect and berry's phase in graphene. *Nature*, 438(7065):201–204, 11 2005.

[204] G. Zhang, H. Qin, J. Teng, J. Guo, Q. Guo, X. Dai, Z. Fang, and K. Wu. Quintuple-layer epitaxy of thin films of topological insulator bi[sub 2]se[sub 3]. *Appl. Phys. Lett.*, 95:053114, 2009.

[205] H. Zhang, C.-X. Liu, X.-L. Qi, X. Dai, Z. Fang, and S.-C. Zhang. Topological insulators in Bi_2Se_3, Bi_2Te_3 and Sb_2Te_3 with a single dirac cone on the surface. *Nature Phys.*, 5:438, 2009.

[206] Y. Zhang, Y.-W. Tan, H. L. Stormer, and P. Kim. Experimental observation of the quantum hall effect and berry's phase in graphene. *Nature*, 438(7065):201, 11 2005.

[207] Y. Zhang, Y.-W. Tan, H. L. Stormer, and P. Kim. Experimental observation of the quantum hall effect and berry's phase in graphene. *Nature*, 438(7065):201–204, 2005.

[208] Y. Zheng and T. Ando. Hall conductivity of a two-dimensional graphite system. *Phys. Rev. B*, 65:245420, 2002.